Li, Runzi. (B.S.) Dioxygen Reactivity of Bioinspired Copper(I) and Copper(I)/Manganese(II)-Porphyrin Systems. **2022**.
Directed by Dr. Shabnam Hematian. 88 pp.

ABSTRACT: Transition metal-dioxygen (O_2) interactions are of great importance in biological and chemical transformations involving dioxygen binding, activation, or reduction. In this work, the independent O_2 reactivity of a series of bioinspired copper(I) complexes with varying ligand electronic environments, as well as the cooperative O_2 reactivity of a copper(I)/manganese(II)-porphyrin assembly, were studied via variable temperature absorption (VT UV-vis-NIR), nuclear magnetic resonance (NMR), and infrared (IR) spectroscopies, along with X-ray crystallography, cyclic voltammetry (CV), and electrospray ionization mass spectrometry (ESI-MS). Our spectroscopic studies confirmed that the copper(I) complexes reversibly react with O_2 to form the corresponding 1:1 copper-O_2 (i.e., *end-on* superoxo) intermediates which can further react reversibly with second equivalents of copper(I) complexes to form the related dinuclear 2:1 copper-O_2 (i.e., *trans*-peroxo) adducts. Small but significant variations in the Cu/O_2 adducts' spectroscopic features suggest that electronic variation in the copper chelates directly affects the electronic properties of the copper-O_2 cores. Furthermore, the bioinspired copper(I) complex $[(tmpa)Cu^{I}(MeCN)]^{+}$ (TMPA: *tris*[(2-pyridyl)methyl]amine) was observed to "trigger" the O_2 reactivity of a manganese(II) porphyrin which displays no independent O_2 chemistry at ambient conditions: In the presence of one or two equivalents of the O_2-active copper center, the O_2-inert manganese center was "triggered" to *cooperatively* active O_2 and perform one or two electron transfers, generating the first examples of such Mn(III)/Cu(II)/O_2 or Mn(IV)/Cu(II)/O_2 species, respectively. The observed cooperative O_2 chemistry was not possible for either metal center independently.

Dioxygen Reactivity of Bioinspired Copper(I) and Copper(I)/Manganese(II)-Porphyrin Systems

by

Runzi Li

A Senior Thesis

Submitted to

the Faculty of The Department of Chemistry and Biochemistry at

The University of North Carolina at Greensboro

Bachelor of Science in Chemistry

Graduated May 2022

Greensboro, NC

Directed by

Dr. Shabnam Hematian
Principal Investigator

Contributors:

Runzi Li, Dr. Shabnam Hematian, Dr. Firoz Shah Tuglak Khan, Marcos Tapia

ACKNOWLEDGEMENTS

Thank you to Dr. Shabnam Hematian, my principal investigator, for guidance and training.

Thank you to all my lab mates, past and present: Firoz, for teaching me the ins and outs of air-free synthesis and mentoring me as a senior in lab; Marcos, for changing the N_2 tank together and sharing your dad jokes; and Amy, for showing me how not to be intimidated by the Randles-Ševčik equation.

For this project, Dr. Maxime A. Siegler is acknowledged for valuable discussions related to X-ray crystallography. I also thank professors Dr. Jerry L. Walsh, Dr. Liam M. Duffy, Dr. Dennis A. Burnes, and Dr. R. Bruce Banks for valuable discussions related to chemistry, spectroscopy, and science.

Grateful acknowledgement is given to the following for support which helped to make this project (and its related publications) possible: the University of North Carolina at Greensboro, for funding via the Spartans ADVANCE Research Award and the URSCO Undergraduate Research and Creativity Award (URCA); the UNC Greensboro Libraries, for funding via the Open Access Publishing Support Fund; and the Joint School of Nanoscience and Nanoengineering, for providing access to the X-ray diffraction facility. Dr. Franklin Moy, Dr. Reynaldo Diaz, and Dr. Daniel Todd are gratefully acknowledged for their expertise and technical support.

Finally, I thank the UNC Greensboro Chemistry faculty and staff, my friends, and my family for your unrelenting support. Though this paper only outlines ~8 months of wet lab work, the experience I gained far outweighs what can be quantitatively measured by time, and you were there for me at every step. Thank you.

TABLE OF CONTENTS

CHAPTER I: INTRODUCTION: DIOXYGEN CHEMISTRY

Dioxygen (O_2) activation and reduction are vital for aerobic life as well as industrial energy applications such as sustainable fuel cells [1,2]. Dioxygen is clean, abundantly available in the air, and a powerful four-electron oxidant, but kinetically inert and requires redox "activation" for its oxidizing power to be utilized [3]. A detailed understanding of the oxygen reduction reaction (Scheme 1) is essential not only for investigating biological processes such as cellular respiration and oxidative phosphorylation (ATP synthesis), but also for developing industrial applications such as sustainable fuel cells [2-4].

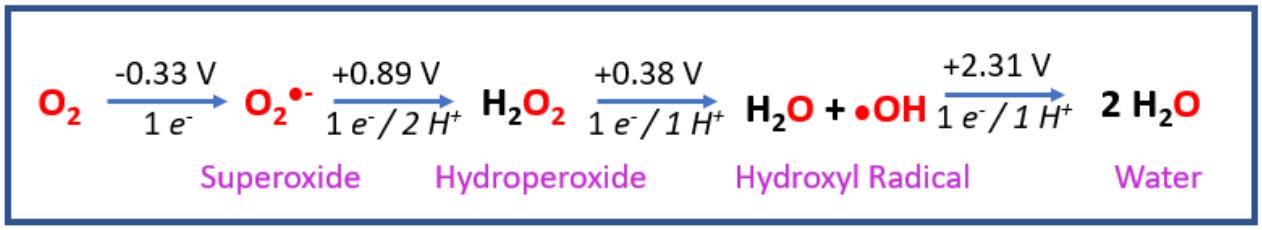

Scheme 1. Stepwise reduction of O_2. $E_{1/2}$ are given vs. NHE at 25 °C, pH 7. Adapted from Ref. [3].

In nature, dioxygen activation and reduction are often facilitated by transition metal centers at metalloenzyme active sites. The O_2 reduction chemistry at Fe/Cu active sites, for example, has been extensively studied for heme-copper oxidases [3]. The independent O_2 reactivities of biomimetic and bioinspired Fe and Cu systems are also well-established and known to vary from the cooperative O_2 chemistry of Fe/Cu, *viz*., the cooperative activation of O_2 by Fe/Cu systems produces new Fe/Cu/O_2 adducts not observed in the independent Fe/O_2 or Cu/O_2 reactions, as seen in enzymes such as cytochrome c oxidase (CcO) [3-5]. Although heme-copper oxidases are ideal target systems for investigating cooperative O_2 reduction and activation in nature, heme-copper oxidases are large, complex integral membrane proteins which are difficult to isolate and directly

study via spectroscopic methods, so synthetic model chemistry is used to study O_2 activation and related O_2 adducts in similar transition metal systems instead.

This work describes investigations of the O_2 reactivities of bioinspired copper(I) and copper(I)/manganese(II)-porphyrin systems which have recently been published by our group [6,7]. The *independent* oxygenation chemistries of a series of bioinspired copper(I) complexes, as well as the *cooperative* oxygenation chemistry of a copper(I)/manganese(II)-porphyrin assembly was studied. Excitingly, our studies revealed that a porphyrin-based manganese site with no independent O_2 chemistry at ambient conditions can, in the presence of a bioinspired copper site, be "triggered" to react toward O_2 and form two new metastable Mn/Cu/O_2 intermediates. Here, an O_2-inert Mn center is "triggered" by the presence of one or two equivalents of an O_2-active Cu center to cooperatively activate O_2 and perform up to two one-electron transfers (i.e., Mn(III) and Mn(IV) intermediate species, respectively). The observed O_2 chemistry was not possible for either metal center independently.

.

CHAPTER II: MATERIALS AND METHODS

We have previously described the following methods in Ref. [6] and [7].

2.1. General Methods

All chemicals were of commercially available grade and used without further purification, unless noted otherwise. Acetonitrile (MeCN), dichloromethane (DCM), tetrahydrofuran (THF), and 2-methyltetrahydrofuran (MeTHF) were purchased from Sigma-Aldrich. Methanol (MeOH) and diethyl ether were purchased from Fisher Chemical. Deuterated solvents (acetone-d_6, $CDCl_3$, CD_2Cl_2, CD_3CN, and THF-d_8) were purchased from Cambridge Isotope Laboratories. Commercial ACS grade solvents were used for chromatography and extractions. All solvents were purified by an Innovative Technologies or Inert PureSolv Micro solvent purification system prior to use for the reactions and characterizations. Solvents were then deoxygenated by bubbling with argon for 1 h followed by storage over 3 or 5 Å molecular sieves for at least 72 h prior to use. Deionized water was purified by a PURELAB flex 1 Analytical Ultrapure Water System (ELGA) to obtain nanopure water with a specific resistance of 18.2 MΩ cm at room temperature.

Air- and moisture-sensitive compounds were prepared and handled under nitrogen atmosphere in a Vacuum Atmospheres OMNI-Lab inert atmosphere (<0.5 ppm of O_2 and H_2O) glovebox, or under a dry, oxygen-free argon atmosphere using standard Schlenk techniques. Ultra-high purity grade oxygen gas was purchased from Airgas and passed through a drying column containing Drierite desiccant and 3 Å activated molecular sieves prior to use. For the Nuclear Magnetic Resonance (NMR) experiments, dry O_2 gas was transferred and stored in a capped 50-mL Schlenk flask, then slowly bubbled into the metal complex solutions via a three-way long syringe needle.

Electrochemical data were collected using a Bio-Logic SP-200 potentiostat. UV-vis absorption spectra were recorded on a Cary-60 spectrophotometer equipped with a Unisoku CoolSpeK USP-203-B cryostat using 4- or 10-mm modified Schlenk quartz cuvettes. Infrared (IR) spectra of neat solid samples were obtained using a Thermo Scientific Nicolet iS5 Fourier Transform IR (FT-IR) spectrometer equipped with an iD7 attenuated total reflection (ATR) accessory. Proton (^{1}H-) and fluorine (^{19}F-) NMR spectra were recorded on either a JEOL 400 or 500 MHz spectrometer. For ^{1}H-NMR spectra, the chemical shifts were referenced against NMR solvent residual shifts (e.g., THF-d_8 at δ = 1.72 ppm) and/or tetramethylsilane (TMS at δ = 0.00 ppm). Electrospray ionization mass spectra (ESI-MS) of the ligands and copper complexes were collected in positive ion mode by a Waters Synapt G2 HDMS q-TOF system; ESI-MS of the copper/manganese samples were collected in positive ion mode on a Thermo Fisher Scientific Plus system.

2.2. Synthesis and Characterization

The compounds TMPA [1], [(tmpa)Cu^{II}Cl][$B(C_6F_5)_4$] [2], [(tmpa)Cu^{I}(MeCN)][$B(C_6F_5)_4$] [3], and [(TPP)Mn^{III}Cl] [4] were prepared and characterized following methods previously described in the literature. Complex [(tmpa)Cu^{I}(MeCN)][$B(C_6F_5)_4$] was further recrystallized from THF/hexanes affording [(tmpa)Cu^{I}][$B(C_6F_5)_4$], and the absence of a bound MeCN ligand was confirmed through ^{1}H-NMR and FT-IR spectroscopies.

2.2.1. Synthesis and characterization of free ligands

F_2TMPA. Under continuous argon flow, a solution of picolylamine (0.96 mL, 9.2 mmol), 3-fluoro-2-formylpyridine (1.27 g, 10.1 mmol), and sodium triacetoxyborohydride (3.12 g, 14.72 mmol) in 1,2-dichloroethane (DCE; 40 mL) was stirred for 2 h. Additional 3-fluoro-2-formylpyridine (1.27 g, 10.1 mmol) and sodium triacetoxyborohydride (3.12 g, 14.72 mmol) were

added, and stirring was continued overnight. The reaction mixture was then mixed with 0.1 M aqueous HCl solution (60 mL; pH = 1), and the DCE layer was discarded. The aqueous layer was washed using DCM (2 × 20 mL), brought to pH = 10 using NaOH pellets, then extracted using DCM (2 × 100 mL). The DCM fractions were evaporated under reduced pressure, redissolved in hot diethyl ether, then cooled at –20 °C overnight to obtain white product crystals, which were washed with cold ether and dried under vacuum. Yield: 1.292 g (43%). ^{1}H-NMR (400 MHz, $CDCl_3$, δ, ppm): 8.46 (d, 1H), 8.35 (d, 2H), 7.57 (m, 2H), 7.31 (td, 2H), 7.19 (m, 2H), 7.09 (td, 1H), 4.03 (d, 2H), 3.99 (s, 1H) (Figure A1). ^{19}F-NMR (376 MHz, $CDCl_3$, δ, ppm): –123.38 (Figure S2). ESI-MS ($[F_2TMPA+H]^+$) calcd./found (*m/z*) : 327.1421/327.1359 (Figure A3). FT-IR (solid): $\nu_{(C\text{-}H,\ Py\ \&\ CH2)}$ = 3056, 3019, 2919, 2889, 2846, and 2819 cm^{-1} (Figure A4).

MeTFE-TMPA. An aqueous solution of 2-(chloromethyl)-3-methyl-4-(2,2,2-trifluoroethoxy)pyridine hydrochloride (6.74 g, 0.024 mol) was prepared, brought to pH = 10 using NaOH pellets, then extracted using DCM (2 x 100 mL). The DCM fractions were evaporated under reduced pressure, then redissolved in THF (80 mL) and transferred to a three-neck round-bottom flask under argon atmosphere. Under continuous argon flow, the THF solution was stirred with di-(2-picolyl)amine (4.9 g, 0.024 mol) and diisopropylamine (25.3 mL, 0.15 mol) for 1 week. After one week, the reaction mixture was evaporated under reduced pressure and purification was performed on an alumina column. The product fraction was eluted with 3-4% MeOH:DCM, evaporated under reduced pressure, redissolved in hot diethyl ether, then cooled at −20 °C overnight to obtain the light-brown solid product, which was washed with cold ether and dried under vacuum. Yield: 5.8081 g, (59%). ^{1}H-NMR (400 MHz, $CDCl_3$, δ, ppm): 8.52 (d, 2H), 8.31 (d, 1H), 7.62 (td, 2H), 7.46 (d, 2H), 7.13 (td, 2H), 6.58 (d, 1H), 4.35 (q, 2H), 3.89 (s, 2H), 3.83 (s, 4H) (Figure A5). ^{19}F-NMR (376 MHz, $CDCl_3$, δ, ppm): –73.79 (Figure A6). ESI-MS ([MeTFE-

TMPA + H]+) calcd./found (m/z) : 403.1746/403.1650 (Figure A7). FT-IR (solid): $\nu_{(C\text{-}H,\ Py\ \&\ CH2)}$ = 3067, 3012, 2949, and 2824 cm^{-1} (Figure A4).

2.2.2. Synthesis and characterization of copper(I) complexes

[(F_2tmpa)Cu^I][$B(C_6F_5)_4$]. The complex was prepared following slight modification of the reported procedure for [(tmpa)Cu^I][$B(C_6F_5)_4$] . In the glovebox, a solution of F_2TMPA (249.8 mg, 0.77 mmol) and [$Cu^I(MeCN)_4$][$B(C_6F_5)_4$] (698.22 mg, 0.77 mmol) in THF (6 mL) was stirred for 30 min at room temperature. Hexanes (40 mL) was added to precipitate the product as a yellow powder, then stirring was continued for 25 min. After allowing the mixture to sit for approximately 30 min to allow the separation of the two layers, the hexanes layer was decanted off as waste, and the hexanes addition/decantation step was repeated twice more. The resulting THF solution was dried under vacuum to obtain the light-yellow solid product. Yield: 703.59 mg (86%). ^{1}H-NMR (500 MHz, CD_3CN, δ, ppm): 8.53 (s, 1H, 6-H), 8.41 (s, 2H, 6'-H), 7.79 (s, 1H, 4-H), 7.57 (s, 2H, 4'-H), 7.38 (m, 4H, 3-H, 5-H, 5'-H), 4.03 (s, 2H, -CH'2-), 3.93 (s, 1H, -CH2-) (Figure A8); (500 MHz, THF-d8, δ, ppm): 8.75 (s, 3H, 6-H, 6'-H), 7.86 (s, 1H, 4-H), 7.72 (s, 2H, 4'-H), 7.57 (m, 4H, 3-H, 5-H, 5'-H), 4.63 (s, 3H, -CH'2-, -CH2-). ^{19}F-NMR (470 MHz, CD_3CN, δ, ppm): −127.8, −134.2, −164.3, and −168.8 (Figure A9); (470 MHz, THF-d8, δ, ppm): −123.9, −132.0, −164.3, and −167.8. ESI-MS ([(F2tmpa)CuI]+) calcd./found (m/z): 389.0639/389.0574 (Figure A10). FT-IR (solid): ν(C-H, Py & CH2) = 3085, 2958, 2925, and 2862 cm^{-1} (Figure A11).

[(MeTFE-tmpa)Cu^I][$B(C_6F_5)_4$]. The synthetic procedure was analogous to that of complex [(F_2tmpa)Cu^I][$B(C_6F_5)_4$], with MeTFE-TMPA (200.2 mg, 0.49 mmol) used in place of F_2TMPA. The product was obtained as a light-yellow solid. Yield: 483.8 mg (85%). 1H-NMR (500 MHz, CD3CN, δ, ppm): 8.52-8.36 (br s, 3H, 6-H, 6'-H), 7.80 (s, 2H, 4-H), 7.34 (br s, 4H, 3-H, 5-H), 6.94 (s, 1H, 5'-H), 4.58 (q, 2H, 8-H), 3.86 (s, 6H, -CH2-), 2.07 (s, 3H, 7-H) (Figure A12); (500

MHz, THF-d8, δ, ppm): 8.96 (br s, 3H, 6-H, 6'-H), 7.83 (s, 2H, 4-H), 7.53 (s, 4H, 3-H, 5-H), 7.20 (s, 1H, 5'-H), 4.73 (br s, 8H, 8-H, -CH2-), 2.17 (s, 3H, 7-H). ^{19}F-NMR (470 MHz, CD_3CN, δ, ppm): −75.3, −134.2, −164.3, and −168.8 (Figure S13); (470 MHz, THF-d8, δ, ppm): −74.5, −132.1, −164.3, and −167.8. ESI-MS ([(MeTFE-tmpa)CuI]+) calcd./found (m/z): 465.0963/465.0890 (Figure A14). FT-IR (solid): ν(C-H, Py & CH2) = 3069, 2961, 2872, and 2854 cm^{-1} (Figure A11).

2.2.3. Synthesis and characterization of copper(II) complexes

[(F_2tmpa)Cu^{II}(Cl)][$B(C_6F_5)_4$]. The complex was prepared following slight modification of the reported procedure for [(tmpa)Cu^{II}(Cl)][$B(C_6F_5)_4$] [2]. A clear green solution of $CuCl_2 \cdot 2H_2O$ (172.2 mg, 1.01 mmol), F_2TMPA (329.6 mg, 1.01 mmol), and 6 drops of water in MeCN (14 mL) was stirred for 10 min at room temperature. While continuing stirring, K[$B(C_6F_5)_4$] (725.3 mg, 1.01 mmol) was added to the reaction mixture, producing a white solid precipitate. The mixture was filtered to remove precipitated KCl, evaporated under reduced pressure, redissolved in diethyl ether (4 mL), and again evaporated under reduced pressure. The resulting solid was recrystallized by slowly cooling a hot MeOH/water solution to produce light blue-green product crystals suitable for X-ray diffraction, which were then dried under vacuum. Yield: 881.2 mg (79%). UV-vis [λ_{max}, nm (ε_{max}, $M^{-1}cm^{-1}$)]: 310 (3,570), 734 (100), and 964 (205) in MeTHF (Figure A15). ^{1}H-NMR (500 MHz, CD_3CN, δ, ppm): 30.31 (br s, 3H, 5,5'-*H*), 10.84-10.04 (s, 3H, 4,4'-*H*) (Figure A16). ^{19}F-NMR (470 MHz, CD_3CN, δ, ppm): −106.19, −134.2, −164.3, and −168.8 (Figure A17). ESI-MS ([(F_2tmpa)Cu^{II}(Cl)]$^+$) calcd./found (*m/z*): 424.0328/424.0192 (Figure A18). FT-IR (solid): $\nu_{(C\text{-}H,\ Py\ \&\ CH2)}$ = 3127, 3101, 3088, and 3082 cm^{-1} (Figure A19).

[(MeTFE-tmpa)Cu^{II}(Cl)][$B(C_6F_5)_4$]. The synthetic procedure was analogous to that of complex [(F_2tmpa)Cu^{II}(Cl)][$B(C_6F_5)_4$], with MeTFE-TMPA used in place of F_2TMPA. The product was obtained as a light-green microcrystalline solid. Yield: 908.7 mg (77%). UV-vis [λ_{max},

nm (ε_{max}, $M^{-1}cm^{-1}$)]: 302 (3750), 734 (98), and 964 (218) in MeTHF (Figure A15). ^{1}H-NMR (500 MHz, CD_3CN, δ, ppm): 22.94 (br s, 5H, 3,5,5'-*H*), 10.48 (s, 2H, 4-*H*), 4.67 (s, 2H, 8-*H*) (Figure S20). ^{19}F-NMR (470 MHz, CD_3CN, δ, ppm): −75.02, −134.2, −164.3, and −168.8 (Figure S21). ESI-MS ([(MeTFE-tmpa)Cu^{II}(Cl)]$^+$) calcd./found (*m/z*): 500.0652/500.0555 (Figure S22). FT-IR (solid): $\nu_{(C\text{-}H,\ Py\ \&\ CH2)}$ = 3110, 3076, 2952, and 2924 cm^{-1} (Figure A19).

2.2.4. Synthesis and characterization of manganese porphyrin complexes

[(TPP)Mn^{II}]. The complex was prepared following slight modification of the literature procedure reported for the ferric choro complexes bearing similar porphyrin rings [5,6]. Using standard Schlenk techniques, a solution of [(TPP)Mn^{III}Cl] (500 mg, 0.711 mmol) in DCM (200 mL) was mixed with a solution of sodium dithionite (22 g, 0.126 mol) in water (100 mL) for 1 h by bubbling argon. The reaction mixture was allowed to sit for approximately 20 min to allow the separation of the two layers. The DCM layer was filtered through sodium sulfate to remove residual water, then dried under vacuum, producing the deep-purple microcrystalline product. Yield: 416 mg (91%). UV-vis (λ_{max}, nm [ε, $M^{-1}cm^{-1}$]): 327 (22,800), 412 (54,300), 432 (495,000), 527 (4000), 568 (16,600), 606 (11,300) in MeTHF; 327 (f,000), 412 (53,800), 432 (492,000), 527 (3000), 568 (15,500), 606 (11,300) in THF. ^{1}H-NMR (THF-d_8, δ, ppm): 38.67 (s, 8H, *β*-pyrrole), 8.01 and 7.84 (s, 20H, phenyl).

[(TPP)$Mn^{III}$$(THF)_2$]$SbF_6$. The complex was prepared following slight modification of the reported procedure for a similar manganese complex [7]. In the glovebox, a solution of [(TPP)Mn^{III}Cl] (101 mg, 0.138 mmol) and $AgSbF_6$ (52 mg, 0.152 mmol) in THF (20 mL) was stirred for 1.5 h under reduced light at room temperature, then filtered to remove precipitated AgCl. The filtrate was concentrated under vacuum and layered with hexanes to obtain the dark-red semi-crystalline product, which was further vacuum dried. Yield: 119 mg (83%). UV-vis (λ_{max}, nm [ε,

$M^{-1}cm^{-1}$]): 382 (52,400), 402 (46,800), 420 (31,300), 472 (67,800), 516 (6500), 565 (9800), 600 (8000) in MeTHF; 382 (51,500), 403 (46,700), 420 (31,400), 472 (64,900), 516 (6200), 565 (9700), 600 (7700) in THF. A UV-vis spectrum of $[(TPP)Mn^{III}(THF)_2]SbF_6$ was also recorded in MeTHF at −110 °C for comparison (Figure B2): 377, 399, 418, 467, 514, 565, and 601 nm. ^{1}H-NMR (THF-d8, δ, ppm): −34.35 (s, 8H, *β*-pyrrole), 9.65 (s, 8H, phenyl-*o*), 8.01 (s, 4H, phenyl-*p*), 7.43 (s, 8H, phenyl-*m*), 3.60 (s, 8H), 1.76 (s, 8H). IR (solid, cm^{-1}): $\nu_{(C\text{-}H,\ MeTHF)}$ = 2950, 2869; $\nu_{(SbF6)}$ = 651.

2.2.5. Single-crystal X-ray diffraction

Suitable X-ray quality single crystals of $[(F_2tmpa)Cu^{II}(Cl)][B(C_6F_5)_4]$ were obtained by recrystallization in hot MeOH/water. Suitable X-ray quality single crystals of $[(TPP)Mn^{III}(MeTHF)_2]SbF_6$ were obtained by transferring a 7 μM solution of $[(TPP)Mn^{III}(THF)_2]SbF_6$ in MeTHF into a 5-mm glass tube, layering with heptane, and storing it in the glovebox at room temperature. All reflection intensities were measured at 100(2) K using a Gemini R diffractometer (equipped with Atlas detector) with MoKα radiation (λ = 0.71073 Å) under the program CrysAlisPro (Version CrysAlisPro 1.171.38.43f, Rigaku OD, 2015). The same program (but a different version viz. CrysAlisPro 1.171.40.53, Rigaku OD, 2019) was used to refine the cell dimensions and for data reduction. The temperature of the data collection was controlled using the system Cryojet (manufactured by Oxford Instruments, Abingdon, UK). The structure was solved with the program SHELXT-2018/2 and was refined on F^2 by full-matrix least-squares technique using the SHELXL-2018/3 program package [8]. Numerical absorption correction based on Gaussian integration was applied using a multifaceted crystal model by CrysAlisPro. Non-hydrogen atoms were refined anisotropically. In the refinement, hydrogen

atoms were treated as riding atoms using SHELXL default parameters. The SUMP command in SHELXL was used to fix the occupancy factors of the fluorine atoms on pyridyl ring to two.

Cambridge Crystallographic Data Center (CCDC no. 2163521) and CSD 2128108 contains the supplementary crystallographic data for this paper. The data can be obtained free of charge via https://www.ccdc.cam.ac.uk/data_request/cif.

2.2.6. Electrochemical studies

Electrochemical data were collected under nitrogen atmosphere in the glovebox using a three-electrode cell. A leak-free Ag/AgCl reference electrode (Innovative Instruments, Inc.), a 3.0-mm glassy carbon working electrode, and a graphite carbon rod counter electrode were used for the measurements. The electrodes were cleaned using nanopure water and acetone prior to each experiment. The supporting electrolyte solution was 100 mM of [(*n*Bu)$_4$N][PF$_6$] in MeCN. The sample solutions (2 mM analyte, 100 mM electrolyte) were scanned anodically then cathodically, at varying scan rates (25, 50, 100, 250, 500, 750, and 1000 mV·s^{-1}; Figures A23-A28 and Table A1). All potentials were further confirmed with the ferricenium/ferrocene couple ($E_{1/2}$ = 0.450 V vs. Ag/AgCl under identical conditions) as an internal reference [9].

2.2.7. Dioxygen reactivity studies

2.2.7.1. Room-temperature UV-vis measurements for [(L)Cu^I][B(C$_6$F$_5$)$_4$]

The general procedure for the dioxygen reactivities of the [(L)Cu^I][B(C$_6$F$_5$)$_4$] complexes (L: F$_2$TMPA, TMPA, or MeTFE-TMPA) is described below, with L being TMPA as a representative case. A stock solution of 5.4 mg (0.005 mmol) of [(tmpa)Cu^I][B(C$_6$F$_5$)$_4$] in MeTHF (2 mL) was prepared inside the glovebox. Samples for UV-vis measurements (450 μM concentration) were prepared by diluting 180 μL of this stock solution with MeTHF to 1 mL, then

transferred to a 4-mm modified Schlenk cuvette equipped with a septum. UV-vis spectra were recorded upon the bubbling of dry O_2 gas directly into the solution at room temperature.

2.2.7.2. Low-temperature UV-vis measurements for [(L)Cu^{I}][B(C_6F_5)$_4$]

The general procedure for the dioxygen reactivities of the [(L)Cu^{I}][B(C_6F_5)$_4$] complexes (L: F_2TMPA, TMPA, or MeTFE-TMPA) is described below, with L being MeTFE-TMPA as a representative case. A stock solution of 6.9 mg (0.006 mmol) of [(MeTFE-tmpa)Cu^{I}][B(C_6F_5)$_4$] in MeTHF (2 mL) was prepared inside the glovebox. Samples for UV-vis measurements (450 μM concentration) were prepared by diluting 180 μL of this stock solution with MeTHF to 1 mL, then transferred to a 4-mm modified Schlenk cuvette equipped with a septum. UV-vis spectra were recorded upon the bubbling of dry O_2 gas directly into the solution at –80 or –110 °C. The solution was monitored at –80 or –110 °C for 30 min after O_2 bubbling, then allowed to warm up to room temperature. The solution was further monitored for 1 h 30 min, with spectra recorded at –80 or –110 °C.

2.2.7.3. Room-temperature UV-vis measurements for [(TPP)Mn^{II}]

Inside the glovebox, 4.8 mg (0.007 mmol) of [(TPP)Mn^{II}] was dissolved in MeTHF (5 mL). Samples for UV-vis spectral measurements were prepared by diluting 7 μL of this stock solution with MeTHF to 1 mL, which was then transferred to a 4-mm modified Schlenk cuvette equipped with a septum. The spectra were recorded upon bubbling of dry O_2 gas directly into the solution at room temperature (Figure 10a).

2.2.7.4. Low-temperature UV-vis measurements for [(TPP)Mn^{II}]

A stock solution of [(TPP)Mn^{II}] (5.3 mg, 0.008 mmol) in MeTHF (5 mL) was prepared inside the glovebox. UV-vis samples for low-temperature measurements were prepared by diluting 7 μL of this stock solution with MeTHF to 1 mL, which was then transferred to a 4-mm modified Schlenk cuvette equipped with a septum. The spectra were recorded upon bubbling of dry O_2 gas

directly into the solution at −90 °C (Figure 10b). The solution was monitored at −90 °C for 30 min after O_2 bubbling, then allowed to warm up to room temperature. The solution was further monitored for 2 h, with spectra recorded at −90 °C.

2.2.7.5. Room-temperature UV-vis measurements for 1:1 and 1:2 mixtures of (TPP)Mn^{II}] and [(tmpa)Cu^{I}(MeCN)][$B(C_6F_5)_4$]

For the 1:1 mixture, 4.7 mg (0.007 mmol) of [(TPP)Mn^{II}] and 7.5 mg (0.007 mmol) of [(tmpa)Cu^{I}(MeCN)][$B(C_6F_5)_4$] were dissolved in MeTHF (5 mL) inside the glovebox. Samples for UV-vis spectral measurements were prepared by diluting 5 μL of this stock solution with MeTHF to 1 mL. The UV-vis sample was then transferred to a 4-mm modified Schlenk cuvette equipped with a septum. The spectra were recorded upon bubbling of dry O_2 gas directly into the solution at room temperature (Figure 11a). The reaction was repeated for the 1:2 mixture (Figure 12a). Here, the stock solution was prepared by dissolving 4.7 mg (0.007 mmol) of [(TPP)Mn^{II}] and 15.1 mg (0.014 mmol) of [(tmpa)Cu^{I}(MeCN)][$B(C_6F_5)_4$] in MeTHF (5 mL) inside the glovebox. All other steps were identical to those described for the 1:1 mixture.

2.2.7.6. Low-temperature UV-vis measurements for 1:1 and 1:2 mixtures of [(TPP)Mn^{II}] and [(tmpa)Cu^{I}(MeCN)][$B(C_6F_5)_4$]

For the 1:1 mixture, 5.3 mg (0.008 mmol) of [(TPP)Mn^{II}] and 8.5 mg (0.008 mmol) of [(tmpa)Cu^{I}(MeCN)][$B(C_6F_5)_4$] were dissolved in MeTHF (5 mL) inside the glovebox. UV-vis samples were prepared by diluting 5 μL of this stock solution with MeTHF to 1 mL. This solution was then transferred to a 4-mm modified Schlenk cuvette equipped with a septum. The spectra were recorded upon bubbling of dry O_2 gas directly into the solution at −110 °C (Figure 11b). The solution was monitored at −110 °C for 1 h after O_2 bubbling, then allowed to warm up to room temperature over 1 h. The spectrum of the warmed solution was recorded at −110 °C. For the 1:2

mixture, 5.3 mg (0.008 mmol) of [(TPP)Mn^{II}] and 17.1 mg (0.016 mmol) of [(tmpa)Cu^{I}(MeCN)][$B(C_6F_5)_4$] were dissolved in MeTHF (5 mL) inside the glovebox. All other steps, described for the 1:1 mixture, were repeated for this sample (Figure 12b).

2.2.7.7. ^{1}H-Nuclear Magnetic Resonance (^{1}H-NMR) measurements for [(L)Cu^{I}][$B(C_6F_5)_4$]

Room temperature ^{1}H-NMR studies were carried out following a slightly modified version of the literature procedure [10]. The general procedure for the dioxygen reactivities of the [(L)Cu^{I}][$B(C_6F_5)_4$] complexes (L: F_2TMPA, TMPA, or MeTFE-TMPA) is described below, with L being TMPA as a representative case. Inside the glovebox, [(tmpa)Cu^{I}(MeCN)][$B(C_6F_5)_4$] (24.2 mg, 0.022 mmol) was dissolved in THF-d_8 (800 μL) and transferred to an NMR tube. The sample was sealed with a rubber septum and transferred outside, and its spectrum was recorded at room temperature. For oxygenation, 4 mL of dry O_2 gas was slowly bubbled into the sample solution using a Hamilton gastight syringe equipped with a three-way valve. After O_2 bubbling, the first spectrum was recorded within 2 min of mixing, and the reaction was monitored over 6 h (Figures B12 and B13).

2.2.7.8. ^{1}H-Nuclear Magnetic Resonance (^{1}H-NMR) measurements for 1:1 and 1:2 mixtures of [(TPP)Mn^{II}] and [(tmpa)Cu^{I}(MeCN)][$B(C_6F_5)_4$]

To prepare the 1:1 mixture NMR sample, 7.5 mg (0.011 mmol) of [(TPP)Mn^{II}] and 12.1 mg (0.011 mmol) of [(tmpa)Cu^{I}(MeCN)][$B(C_6F_5)_4$] were dissolved in THF-d_8 (800 μL) and transferred to an NMR tube inside the glovebox. The NMR sample sealed with a rubber septum was taken out, and the spectrum prior to dioxygen bubbling was recorded at room temperature. For oxygenation, 4 mL of dry O_2 gas was bubbled into the metal complex solution in the NMR tube using a Hamilton gastight syringe equipped with a three-way valve. After O_2 bubbling, the first spectrum was recorded within 2 min of mixing, and the reaction was monitored over 18 h

(Figures 5 and B11). The same steps were repeated for the 1:2 mixture NMR sample which was prepared by dissolving 7.5 mg (0.011 mmol) of [(TPP)Mn^{II}] and 24.2 mg (0.022 mmol) of [(tmpa)Cu^{I}(MeCN)][$B(C_6F_5)_4$] in THF-d_8 (800 μL).

2.2.8. Electrospray Ionization Mass Spectrometry (ESI-MS) measurements

The 1:1 mixture stock solution was prepared by dissolving 7.5 mg (0.011 mmol) of [(TPP)Mn^{II}] and 12.1 mg (0.011 mmol) of [(tmpa)Cu^{I}(MeCN)][$B(C_6F_5)_4$] in MeTHF (800 μL) inside the glovebox. The stock solution was brought out in a Schlenk flask equipped with a rubber septum, and dry O_2 gas was bubbled into the mixture for 30 s. Samples for ESI-MS measurement were taken from this Schlenk flask and diluted by 20 folds in MeTHF before injection. The same procedure was repeated for the 1:2 mixture, whose stock solution was prepared by dissolving 7.5 mg (0.011 mmol) of [(TPP)Mn^{II}] and 24.2 mg (0.022 mmol) of [(tmpa)Cu^{I}(MeCN)][$B(C_6F_5)_4$] in MeTHF (800 μL), followed by bubbling dry O_2. In order to detect multinuclear assemblies, soft ionization was maintained at a relatively low source voltage of 1.0 kV.

CHAPTER III: DIOXYGEN REACTIVITY OF COPPER(I) COMPLEXES

This chapter is adapted from our publication in *Journal of Coordination Chemistry*, "Oxygenation of copper(I) complexes containing fluorine tagged tripodal tetradentate chelates: Significant ligand electronic effects" [37].

3.1. Introduction: Copper(I)/Dioxygen Chemistry

The dioxygen (O_2) chemistry of synthetic copper(I) complexes and the oxidative properties of the resulting copper-O_2 adducts are of great importance due to their potential relevance to copper-containing proteins vital for aerobic life as well as their applications in chemical catalysis [1-5]. In nature, copper-dioxygen interactions are essential for facilitating an array of biological functions in many proteins including the dioxygen-carrier hemocyanin, monooxygenases where O_2 is activated such as in tyrosinase, dopamine β-hydroxylase, and phenylalanine hydroxylase, or oxidases where O_2 is reduced to H_2O or H_2O_2 including in laccase, galactose oxidase, ascorbate oxidase, amine oxidase, and the heme-copper binuclear active site of cytochrome *c* oxidase [2,6-8].

One of the most well-studied synthetic systems that has provided insights into copper-O_2 chemistry is the mononuclear cuprous complex of the nitrogen-containing tetradentate tripodal ligand, *tris*[(2-pyridyl)methyl]amine (TMPA) [9-13]. The mononuclear complex $[(tmpa)Cu^{I}(MeCN)]^{+}$ reversibly binds O_2 to form an η^1 "*end-on*" cupric superoxide ($Cu^{II}–O_2^{\bullet-}$) species which then rapidly reacts, even at low temperatures, with another equivalent of cuprous complex to generate a binuclear *trans*-peroxo-dicopper(II) complex, $[(tmpa)Cu^{II}–(O_2)–Cu^{II}(tmpa)]^{2+}$ (Figure 1) [11,13-17].

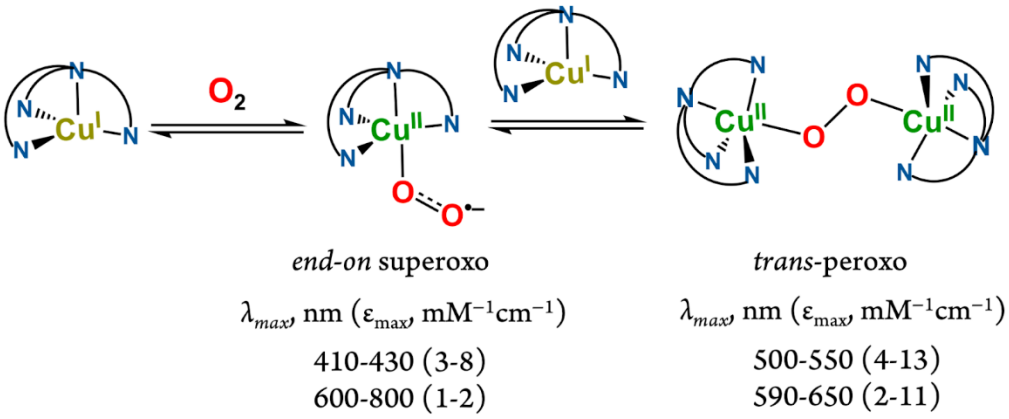

Figure 1. Mechanism for the oxygenation reaction of TMPA-like copper(I) complexes.

Modifications of the TMPA framework to influence the steric and electronic properties of the donor atoms have shown that the presence of electron-donating substituents leads to energetic stabilization of the superoxo intermediate and chelates with large steric demands and a negative charge can prevent the dimerization and formation of the corresponding peroxo species in solution [10,13,18,19]. In this report, we describe and compare the oxygenation of the cuprous complexes of two new TMPA-derivatives, one electron rich and one electron deficient, with fluorine atoms attached to the chelate backbones which also provide the ability to probe the dioxygen reactivity of these systems through ^{19}F-NMR spectroscopy (Figure 2). The dioxygen reactivities of the copper(I) complexes were investigated using ^{1}H- and ^{19}F-NMR spectroscopies along with variable-temperature UV-vis measurements. For comparison, the corresponding copper(II)-chloro complexes were also synthesized and characterized using a series of spectroscopic methods as well as cyclic voltammetry, mass spectrometry, and X-ray crystallography. The properties of copper(I) and copper(II)-chloro complexes are compared, particularly with respect to the influence of the pyridyl substituents present in the new ligand scaffolds. Some mechanistic insights regarding oxygenation reactions are also presented.

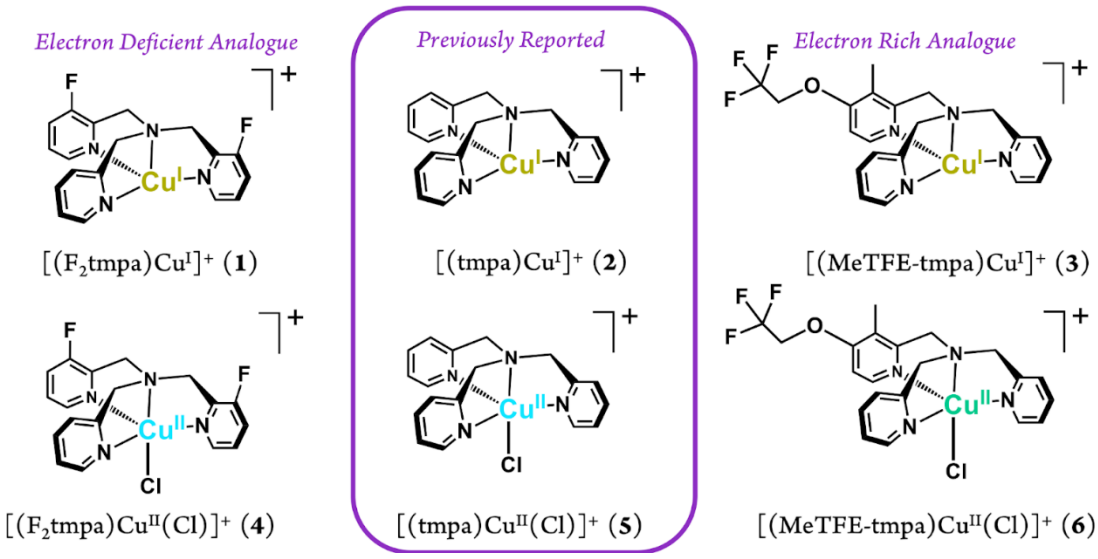

Figure 2. Copper(I) and copper(II) complexes described in this study. All complexes were prepared with $[B(C_6F_5)_4]^-$ as the counter anion.

3.2. Structural and physical properties of copper complexes

New ligands. To study the electronic effects in modulating the dioxygen reactivity of the cuprous complexes, we prepared two new TMPA-based ligands, with either electron-withdrawing or -donating groups on the pyridyl arms. Inclusion of fluorine groups on the backbone of the chelates also provided an additional tool for probing the oxygenation reactions. In the electron deficient F_2TMPA chelate, fluorine atoms occupy the 3'-position of the two substituted pyridyl rings whereas in the electron rich MeTFE-TMPA derivative a methyl group along with a trifluoroethoxy (TFE) pendant are attached to the 3' and 4'-positions of the substituted pyridyl ring, respectively. From the coordination chemistry perspective, the ligands were designed in such way that in both TMPA derivatives two of the three pyridyl rings serve as weaker σ-donors as compared to the third pyridyl arm (i.e., the two fluorine-substituted pyridine rings in F_2TMPA relative to its unsubstituted arm or the two unsubstituted pyridine rings in MeTFE-TMPA compared to the 3-methyl-4-(2,2,2-trifluoroethoxy)pyridine arm). The ligand F_2TMPA was

synthesized through reductive amination while MeTFE-TMPA was prepared via a nucleophilic substitution reaction. Further details are presented in the Experimental Section and Scheme A1. Both tetradentate ligands contain groups with fluorine atoms which can be probed using ^{19}F-NMR spectroscopy. Both ligands were characterized through ^{1}H- and ^{19}F-NMR, FT-IR, ESI-MS measurements. It is important to note that previously synthetic difficulties encountered were described as the reason for not including any O_2-reactivity studies of the TMPA-based cuprous complexes with electron-withdrawing groups [24].

Copper(I) complexes. Cuprous complexes were synthesized with *tetrakis*(pentafluorophenyl)borate, $[B(C_6F_5)_4]$, as a counter anion for enhanced solubility, by mixing one equivalent of each ligand and $[Cu^{I}(MeCN)_4][B(C_6F_5)_4]$ in THF in the glovebox (see Experimental Section). Previous reports have shown that copper(I) complexes of TMPA-like ligands effect reductive dehalogenation reactions with a wide range of organohalide substrates [25-28]. Even a reactivity study of a TMPA-based chelate possessing a pendant R–Cl moiety (i.e., internal substrate) revealed the involvement of a copper-alkyl intermediate [29]. However, with regard to the MeTFE-TMPA ligand, the presence of the trifluoroethoxy arm on the 4'-pyridyl position during the preparation of the copper(I) complex led to no observable reductive defluorination reaction, likely due to the stronger carbon-fluorine bonds as compared to those of other halides.

Both cuprous complexes, $[(F_2tmpa)Cu^{I}][B(C_6F_5)_4]$ and $[(MeTFE\text{-}tmpa)Cu^{I}][B(C_6F_5)_4]$ were characterized using UV-vis, FT-IR, ^{1}H- and ^{19}F-NMR spectroscopies as well as mass spectrometry and cyclic voltammetry. The ^{19}F-NMR spectra of the two cuprous complexes supported the presence of one equivalent of $[B(C_6F_5)_4]^{-}$ per ligand-copper moiety. Moreover, the parent $[(tmpa)Cu^{I}(MeCN)]^{+}$ has been proven to

possess one coordinated acetonitrile molecule per tetradentate ligand-copper core preferring pentacoordinate geometry while the bound MeCN ligand can be removed by multiple recrystallization from a weakly coordinating solvent such as THF or diethyl ether [25,28]. The ^{1}H-NMR and IR spectra of two new isolated copper(I) complexes with F_2TMPA and MeTFE-TMPA revealed that both systems adopt a tetracoordinate formulation $[(L)Cu^{I}]^{+}$ with no MeCN incorporated as a fifth ligand. This is not surprising as these complexes were prepared and isolated in THF.

Copper(II) complexes. The copper(II)-chloro complexes of the two new chelates, F_2TMPA and MeTFE-TMPA, were prepared following a similar procedure to the one previously reported for the parent complex, $[(tmpa)Cu^{II}(Cl)][B(C_6F_5)_4]$ [20]. The ^{19}F-NMR spectra of the copper(II)-chloro complexes, with F_2TMPA and MeTFE-TMPA, confirmed the association of two equivalents of $[B(C_6F_5)_4]^{-}$ with one ligand-copper moiety in each system. The complexation of copper(II)-chloro complexes was further confirmed via ^{1}H-NMR, FT-IR, mass spectrometry, and cyclic voltammetry measurements. The reduction potentials of the copper(II)-chloro complexes are significantly lower (> –340 mV) than those of the cuprous complexes (vide infra).

In contrast to the four-coordinate structures of $[(L)Cu^{I}][B(C_6F_5)_4]$ (L: F_2TMPA, TMPA, and MeTFE-TMPA) but common in copper(I) ion chemistry, the copper centers in the copper(II)-chloro counterparts are penta-coordinate. In general, a five-coordinate cupric center in a square pyramidal (*SP*) environment exhibits a broad band in the visible region (590–780 nm) along with a low-energy spin forbidden shoulder at $\lambda > 800$ nm, whereas in a trigonal bipyramidal (*TBP*) geometry displays a main *d-d* transition at $\lambda > 800$ nm with a high-energy shoulder in the visible region [30]. The electronic absorption spectra of the two

new as well as the parent copper(II)-chloro complexes exhibit one main *d-d* transition band centred at 964 nm and a shoulder at around 734 nm revealing that the *TBP* geometry is dominant is all three cupric systems in solution (Figure S15).

The intense ligand-to-metal charge transfer (LMCT) bands from the bound chloride ligand to the cupric center in the complexes bearing the F_2TMPA, TMPA, and MeTFE-TMPA chelates, appear at 310, 305, and 302 nm, respectively, supporting the more stabilized d_{z2} orbitals in the former, $[(F_2tmpa)Cu^{II}(Cl)][B(C_6F_5)_4]$.

Crystal structure of $[(F_2tmpa)Cu^{II}(Cl)][B(C_6F_5)_4]$. The complex crystallizes in a triclinic crystal system with *P*-1 space group (see Experimental Section, Figure A29, and Table A2). The molecular structure of the complex is shown in Figure 3 and relevant bond distances and angles are given in the figure captions. The cupric center is penta-coordinated with three pyridyl nitrogen atoms (N1, N3, and N4) and one tertiary alkyl amino nitrogen (N2) along with a chloride ion.

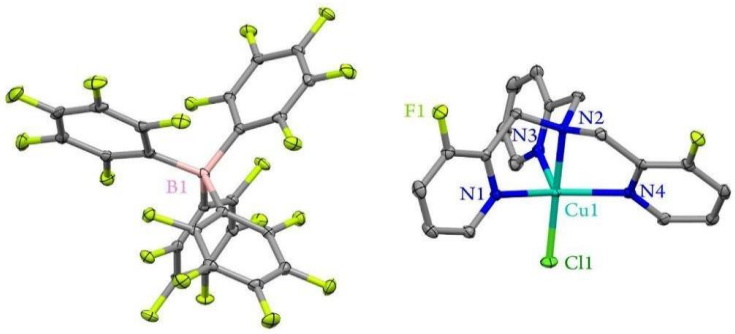

Figure 3. Displacement ellipsoid plot (50% probability level) of $[(F_2tmpa)Cu^{II}(Cl)][B(C_6F_5)_4]$, showing the atom-labeling scheme. Hydrogen atoms have been omitted for the sake of clarity. Selected bond lengths (Å) and angles (deg): Cu(1)-N(1), 2.0596(15); Cu(1)-N(2), 2.0553(14); Cu(1)-N(3), 2.1016(15); Cu(1)-N(4), 2.0400(15); Cu(1)-Cl(1), 2.2311(5); N(4)-Cu(1)-N(2), 80.29(6); N(4)-Cu(1)-N(1), 131.10(6); N(2)-Cu(1)-N(1), 81.24(6); N(4)-Cu(1)-N(3), 112.45(6); N(2)-Cu(1)-N(3), 80.55(6); N(1)-Cu(1)-N(3), 108.51(6); N(4)-Cu(1)-Cl(1), 98.83(4); N(2)-Cu(1)-Cl(1), 178.19(4); N(1)-Cu(1)-Cl(1), 98.24(4); N(3)-Cu(1)-Cl(1), 101.25(4).

The Addison-Reedijk geometry analysis allows for the semiquantitative estimation of the prevalent geometry in crystalline phase [31], further supporting that the cupric center adjusts to a distorted *TBP* (τ_5 = 0.78) coordination environment in F_2TMPA while the ligation in the parent TMPA analogue is reported to occur within a nearly perfect *TBP* geometry (τ_5 = 0.95) [20]. The prominent *TBP* organization of the ligands around the cupric center observed in the crystalline phase agrees well with those speculated from their *d-d* absorption patterns for the solution phase (vide supra).

Electrochemistry. The electrochemical behavior of the copper complexes was studied by cyclic voltammetry (CV) under an inert atmosphere in MeCN. All complexes display a single one-electron transfer process showing quasi-reversible behavior with peak-to-peak separation values, ΔE, no more than 112 mV (Table 1) and anodic/cathodic peak current ratios (i_{pa}/i_{pc}) between 0.96 and 0.79.

Table 1. $E_{½}$ and $\Delta E_{½}$[a] values of copper complexes described in this study in MeCN with $[(n\text{Bu})_4\text{N}][PF_6]$ as the supporting electrolyte (100 mM).

Complex	$E_{½}$ vs. Ag/AgCl (V)	$E_{½}$ vs. Fc/Fc^+ (V)	ΔE (mV)[a]	i_{pa}/i_{pc}
$[(F_2\text{tmpa})Cu^{I}][B(C_6F_5)_4]$	+0.150	–0.300	105	0.955
$[(\text{tmpa})Cu^{I}][B(C_6F_5)_4]$	+0.038	–0.412	94	0.941
$[(\text{MeTFE-tmpa})Cu^{I}][B(C_6F_5)_4]$	–0.010	–0.460	112	0.944
$[(F_2\text{tmpa})Cu^{II}(Cl)][B(C_6F_5)_4]$	–0.213	–0.663	95	0.861
$[(\text{tmpa})Cu^{II}(Cl)][B(C_6F_5)_4]$	–0.306	–0.756	100	0.786
$[(\text{MeTFE-tmpa})Cu^{II})(Cl)][B(C_6F_5)_4]$	–0.348	–0.798	107	0.955

[a]The values were obtained at 100 mV s^{-1} scan rate.

Our Randles-Sevcik analysis of the peak current vs. the square root of the scan rate confirmed that in all cases the species involved in the redox reactions were freely diffusing through the solution. The diffusion coefficients (*D*) are presented in Table A1. The diffusion coefficients of the cupric and cuprous forms of the $[(L)Cu]^{n+}$ species are between 1.38 and 2.96 × 10^{-4} cm^2 s^{-1}. It is also worth noting that the presence of the chloride ligand systematically decreases the reduction potential of the copper center by about 350 mV in all three chelate environments (Figure 4).

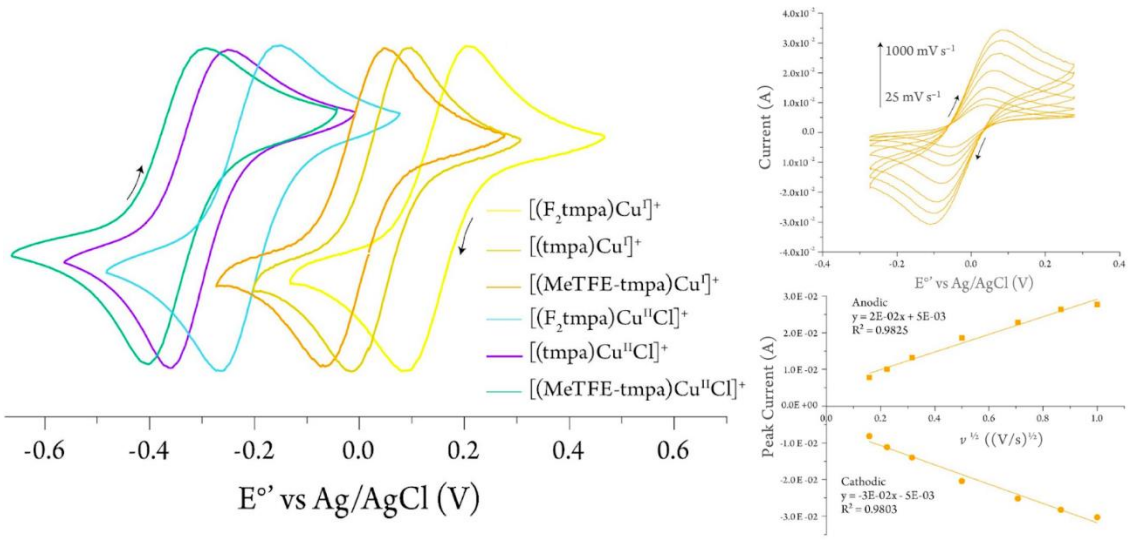

Figure 4. Electrochemical data obtained for copper complexes described in this study. (*Left*) normalized cyclic voltammograms of 1-6 at 100 mV·s^{-1} scan rate. (*Right*) Representative cyclic voltammograms of the [(MeTFE-tmpa)Cu^{I}][B(C_6F_5)$_4$] (2 mM) at various scan rates along with the Randles–Sevcik plot of the CV data. All measurements were performed in MeCN with 100 mM of [(*n*Bu)$_4$N][PF_6] as the supporting electrolyte.

The data shown for copper complexes reveal that, with substituted pyridyl ligands bearing electron-donating or -withdrawing groups, the $E_{½}$ value for the $Cu^{II/I}$ redox couple becomes more negative or more positive compared to that for the complex with the parent TMPA ligand, respectively. In other words, MeTFE-TMPA scaffold results in a more thermodynamically stable copper(II) complex while F_2TMPA forms a more thermodynamically stable copper(I) species as compared to the parent system. The variation in electrochemical behavior of copper(I) species with pyridyl ligands correlates to the O_2-reactivity differences observed in these systems (vide infra).

3.3. Oxygenation reactions of copper(I) complexes

The interaction of cuprous complexes, [(L)Cu^{I}][B(C_6F_5)$_4$] (L: F_2TMPA, TMPA, and MeTFE-TMPA), with dioxygen in MeTHF follows the same basic mechanism which has been reported for other TMPA-like systems as described in the Introduction (Figure 1). The oxygenation reactions

were monitored by variable temperature electronic absorption as well as ^{1}H- and ^{19}F-NMR spectroscopies.

UV-vis absorption spectroscopy. Bubbling O_2 into the solution of each copper(I) complex at room temperature resulted in the signature, intense color change from light yellow to purple known for the formation of binuclear *trans*-peroxo-dicopper(II) complexes (Figure 5). The absorption spectra of the purple *trans*-peroxo-dicopper(II) intermediates with the F_2TMPA, TMPA, and MeTFE-TMPA chelates in MeTHF solution showed intense absorption bands at 526, 525, and 523 nm along with shoulders at around 617, 616, 614 nm, respectively. These two characteristic spectral features in the visible region are respectively ascribed to $\pi_\sigma^* \rightarrow d$ and $\pi_v^* \rightarrow d$ charge transfer (CT) transitions from the *trans*-peroxo ligand to the two copper centers and are consistent with the presence of highly covalent Cu–O bonds [7,32,33].

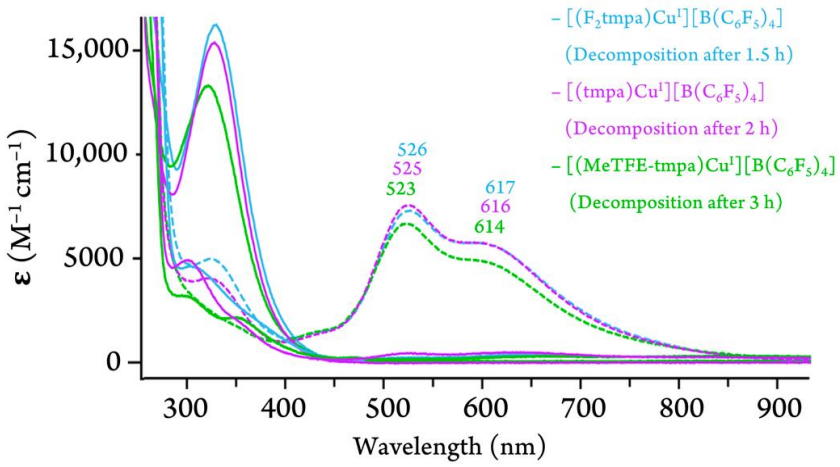

Figure 5. Room temperature UV-vis spectra of MeTHF solutions of the copper(I) complexes before O_2 addition (solid lines), immediately after 5 s of O_2 bubbling (dotted lines), and after ~100% decomposition. *Note:* The molar extinction coefficients are shown per two copper centers forming the *trans*-peroxo-dicopper(II) species (i.e., the ε values for the monomer cuprous complexes are in the range of 6-8 $mM^{-1}cm^{-1}$).

It is worth mentioning that a close analysis of the previously reported X-ray structure of the parent *trans*-peroxo species, $[(tmpa)Cu^{II}–(O_2)–Cu^{II}(tmpa)]^{2+}$, reveals that the copper centers display an almost ideal *TBP* geometry (τ_5 = 0.89), consistent with the structure of its copper copper(II)-chloro analogue, $[(tmpa)Cu^{II}(Cl)]^{+}$ (τ_5 = 0.95). Assuming the same relationship exists between the two new *trans*-peroxo-dicopper(II) complexes and the corresponding copper(II)-chloro counterparts, the τ_5 value and supporting electronic absorption results would suggest that the cupric site of the corresponding t*rans*-peroxo species, though to different degrees, adjust to a distorted *TBP* coordination environment, thus, supporting a d_{z2} ground state. The systematic hypsochromic (i.e., blue) shift of both CT bands in moving from the electron deficient system bearing F_2TMPA to the electron rich analogue with MeTFE-TMPA strongly suggests that the higher degree of electron donation from the chelate destabilizes d_{z2}, hence, shifting the LMCT bands from the bridging peroxide π*-orbitals to the cupric center to the higher energies (i.e., hypsochromic shift).

Interestingly, the spectra recorded immediately after the addition of O_2 to the three cuprous solutions revealed that the electron rich $[(MeTFE\text{-}tmpa)Cu^{I}][B(C_6F_5)_4]$ (**3**) system instantaneously reacted with O_2 with no residual amount of cuprous species left while in the case of the parent $[(tmpa)Cu^{I}][B(C_6F_5)_4]$ (**2**) complex and its electron deficient derivative, $[(F_2tmpa)Cu^{I}][B(C_6F_5)_4]$ (**1**), some cuprous species were still present in the solution. The observed trend follows the redox potential pattern of the cuprous complexes. Thus, the thermodynamic stability of the *trans*-peroxo species bearing MeTFE-TMPA is much higher than that of the TMPA or F_2TMPA analogues manifesting a considerable ligand electronic effect. This finding is in agreement with our NMR

studies at room temperature, confirming that the *trans*-peroxo species of MeTFE-TMPA is significantly more stable than the more electron deficient analogues (vide infra).

The association of two cuprous complexes with O_2 to form a *trans*-peroxo bridged dicopper assembly is an entropically unfavorable process. The effect of this entropic cost can be alleviated by lowering the temperature. Lower temperatures also increase the lifetime of the initially formed copper-dioxygen intermediates not only by reducing the entropic costs of formation but also by attenuating subsequent reactions. Therefore, further investigation of the oxygenation reactions of the copper(I) complexes were performed at lower reaction temperatures. At –80 °C, the copper(I) complexes of TMPA and F_2TMPA instantly reacted with dioxygen to form the corresponding *trans*-peroxo dicopper (i.e., 1:2 copper-dioxygen) intermediates with no sign of residual cuprous complex (Figure 6). The resulting *trans*-peroxo species were stable at –80 °C and only decomposed upon briefly warming up to room temperature. While no *end-on* superoxo (i.e., 1:1 copper-dioxygen) intermediates were detected within the measurement time (i.e., 5 s) during the oxygenation of either copper(I)-TMPA or -F_2TMPA complex, a significant amount of this transient species was observed from the reaction of O_2 with the copper(I)-MeTFE-TMPA complex with λ_{max} at 425 nm and 765 nm, which within 30 min of O_2 bubbling, fully converted into the stable *trans*-peroxo complex, $[(\text{MeTFE-tmpa})Cu^{II}–(O_2)–Cu^{II}(\text{MeTFE-tmpa})]^{2+}$, with λ_{max} at 518 nm and 600 nm.

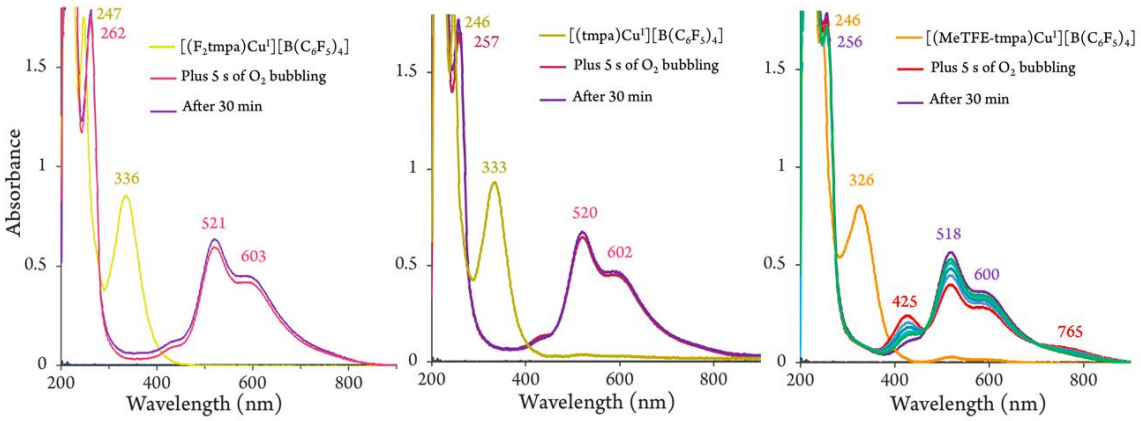

Figure 6. UV-vis spectral changes observed during reaction of the copper(I) complexes with O_2 in MeTHF at –80 °C.

Further lowering of temperature to –110 °C led to remarkable differences in the oxygenation reactivities compared to those at –80 °C as is evident in Figures 6 and 7. The addition of O_2 to all three copper(I) complexes at –110 °C in MeTHF, instantly led to full formation of the corresponding *end-on* superoxo intermediates. In the case of MeTFE-TMPA, a clean and stable *end-on* superoxo species was formed with an intense absorption band at 420 nm and two weaker features at 519 and 587 nm and a more prominent band at 759 nm. The former has been tentatively assigned to a $\pi_\sigma^* \rightarrow d$ CT transition, in which the in-plane π_σ^* orbital of the superoxide ion overlaps in σ fashion, with the d_{z2} orbital of the cupric center [13]. The oxygenation of the other two copper(I) complexes, **1** and **2**, however, resulted in the formation of a mixture of the corresponding 1:1 and 1:2 copper-O_2 adducts, with the *end-on* superoxo intermediate initially being the major species and readily converting to the corresponding *trans*-peroxo dicopper complex.

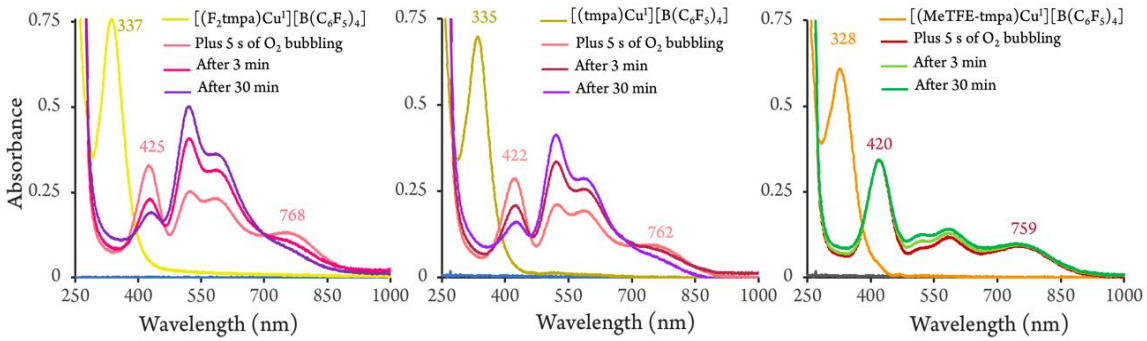

Figure 7. UV-vis spectral changes observed during reaction of the copper(I) complexes with O_2 in MeTHF at –110 °C.

Comparisons of copper(I)-dioxygen reactivities at different temperatures, point to varying degrees of change in the rate of the initial reversible O_2 binding and the subsequent formation of the bridged *trans*-peroxo complex. At –80 °C, much slower transformation of the *end-on* superoxo into the *trans*-peroxo species with the MeTFE-TMPA chelate as compared to the other two systems, suggests that the concentration of the copper(I) complex, **3**, must be minute due to a very large equilibrium constant for formation of the *end-on* superoxo complex at that temperature. These results are indicative of a clear ligand electronic effect, precluding formation of the corresponding *trans*-peroxo at the lowest temperature, –110 °C. At higher temperatures, the rate of formation of the *trans*-peroxo complex bearing MeTFE-TMPA strongly increases as is particularly noticeable in comparing Figures 5-7. This is again likely due to the shift in the equilibrium between **3** and the corresponding *end-on* superoxo species, making **3** available for the formation of the peroxo complex.

We also note that a similar correlation between the electronic effects of the three chelates and the energy of the absorption features in both *end-on* superoxo and *trans*-peroxo dicopper species were observed. As listed in Table 2, all CT bands shift to lower energies as the chelates become more electron deficient and stabilize the d_{z2} orbitals.

Table 2. Major electronic absorption features of the cupric *end-on* superoxo at –110 °C[a] and *trans*-peroxo complexes at room temperature[b].

Dioxygen Adduct	max(nm)*
$[(F_2tmpa)Cu^{II}\text{-}(O_2^{\cdot-})]^+$	425 and 768[a]
$[(tmpa)Cu^{II}\text{-}(O_2^{\cdot-})]^+$	422 and 762[a]
$[(MeTFE\text{-}tmpa)Cu^{II}\text{-}(O_2^{\cdot-})]^+$	420 and 759[a]
$[(F_2tmpa)Cu^{II}\text{–}(O_2^{2-})\text{–}Cu^{II}(F_2tmpa)]^{2+}$	526 and 617[b]
$[(tmpa)Cu^{II}\text{–}(O_2^{2-})\text{–}Cu^{II}(tmpa)]^{2+}$	525 and 616[b]
$[(MeTFE\text{-}tmpa)Cu^{II}\text{–}(O_2^{2-})\text{–}Cu^{II}(MeTFE\text{-}tmpa)]^{2+}$	523 and 614[b]

Nuclear Magnetic Resonance Spectroscopy. To further confirm the formation of *trans*-peroxo-dicopper(II) species and subsequent decomposition as observed in the UV-vis studies (vide supra), the dioxygen reactivity of the cuprous complexes was studied through ^{1}H- and ^{19}F-NMR spectroscopies at room temperature. Karlin and co-workers have previously shown that the two cupric centers in the parent *trans*-peroxo-dicopper(II) assembly were strongly antiferromagnetically coupled (i.e., singlet ground state) [25], therefore, well resolved ligand resonances in both ^{1}H- and ^{19}F-NMR spectra were expected.

The ^{1}H-NMR spectrum of $[(F_2tmpa)Cu^I][B(C_6F_5)_4]$ (**1**) in THF-d_8 displayed four signals between δ = 8.75–7.57 ppm corresponding to the protons of the pyridyl arms while the methylene protons appeared at δ = 4.63 ppm (Figure 8). The addition of dry O_2 and the subsequent formation of the *trans*-peroxo-dicopper(II) species resulted in a downfield shift of the proton resonances (i.e., $\delta_{Py\text{-}H}$ = 10.83, 8.24, 7.95, and 7.76 ppm and $\delta_{\text{-}CH2}$ = 5.77 ppm) reflecting the expected deshielding that was associated with the removal of electron density from the copper center. A similar trend was also observed in the ^{1}H-NMR spectra for oxygenation of the parent system with

the TMPA chelate, in THF-d_8 (Figures S30 and S31) [23] consistent with the reactivity pattern previously reported in CD_2Cl_2 [25].

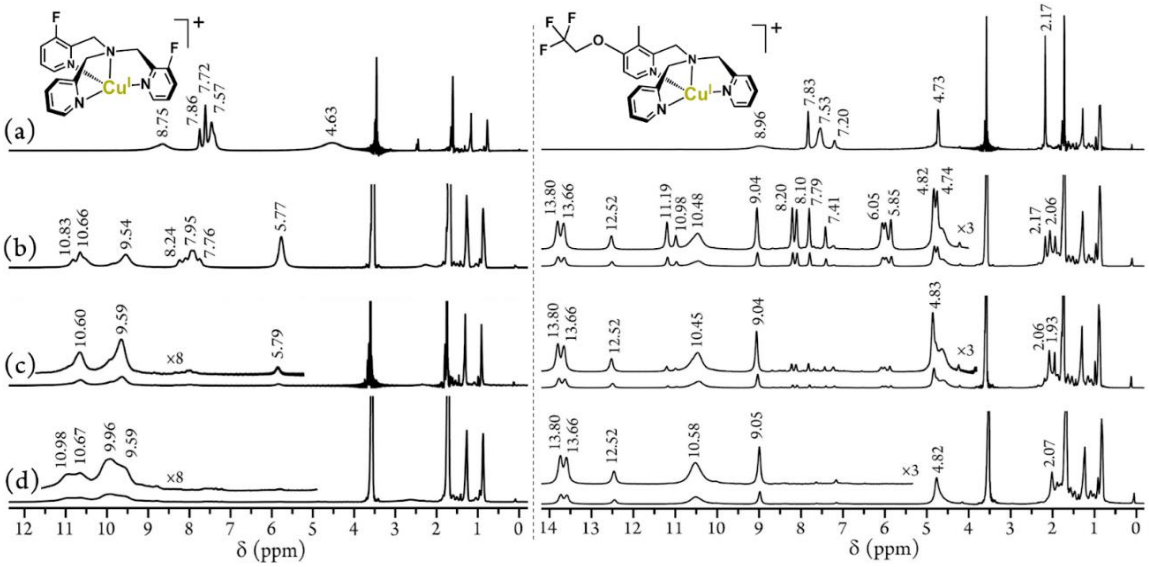

Figure 8. Diamagnetic region of the ^{1}H-NMR spectra of the oxygenation reactions of (*left*) $[(F_2tmpa)Cu^I][B(C_6F_5)_4]$ and (*right*) $[(MeTFE\text{-}tmpa)Cu^I][B(C_6F_5)_4]$ at (a) 0 min, (b) 1 min, (c) 15 min, (d) 6 h in THF-d_8 (500 MHz) at room temperature.

It is important to note that due to the decomposition of the *trans*-peroxo-dicopper(II) intermediates to paramagnetic monomeric copper(II) species, different and growing amounts of these final decomposition products were present throughout the oxygenation reactions of all the cuprous systems. For instance, the initial spectrum for the dioxygen exposed solution of $[(F_2tmpa)Cu^I][B(C_6F_5)_4]$ also showed additional peaks at δ = 10.66 and 9.54 ppm along with a series of paramagnetic signals in the downfield region (δ = 16.42–43.56 ppm) which all corresponded to the monomeric $[(F_2tmpa)Cu^{II}(X)]^{n+}$ species. Decomposition of the *trans*-peroxo-dicopper(II) intermediates to the final monomeric cupric products were completed within a few hours at room temperature.

The dioxygen reactivity of **1** was also monitored through ^{19}F-NMR spectroscopy (Figure 9). The ^{19}F-NMR spectra of $[(F_2tmpa)Cu^{I}][B(C_6F_5)_4]$ displayed one signal at δ = –126.86 ppm for the two fluorine atoms occupying the 3'-position of the two substituted pyridyl arms and three signals at δ = –132.04, –164.28, and –167.77 ppm for the fluorines of the $[B(C_6F_5)_4]^-$ counter anion. Upon dioxygen bubbling into the solution, the 3'-fluorine signal transformed into two new signals, one sharp peak at δ = –123.38 ppm and another broad peak at –101.44 ppm while the signals from $[B(C_6F_5)_4]^-$ remained unchanged. We assigned the former (i.e., δ = –123.38 ppm) to the 3'-fluorine resonance of the diamagnetic μ-peroxo $[(F_2tmpa)Cu^{II}–(O_2^{2-})–(F_2tmpa)]^{2+}$ species while the latter (i.e., δ = –101.44 ppm) corresponded to the monomeric decomposition product, $[(F_2tmpa)Cu^{II}(X)]^{n+}$.

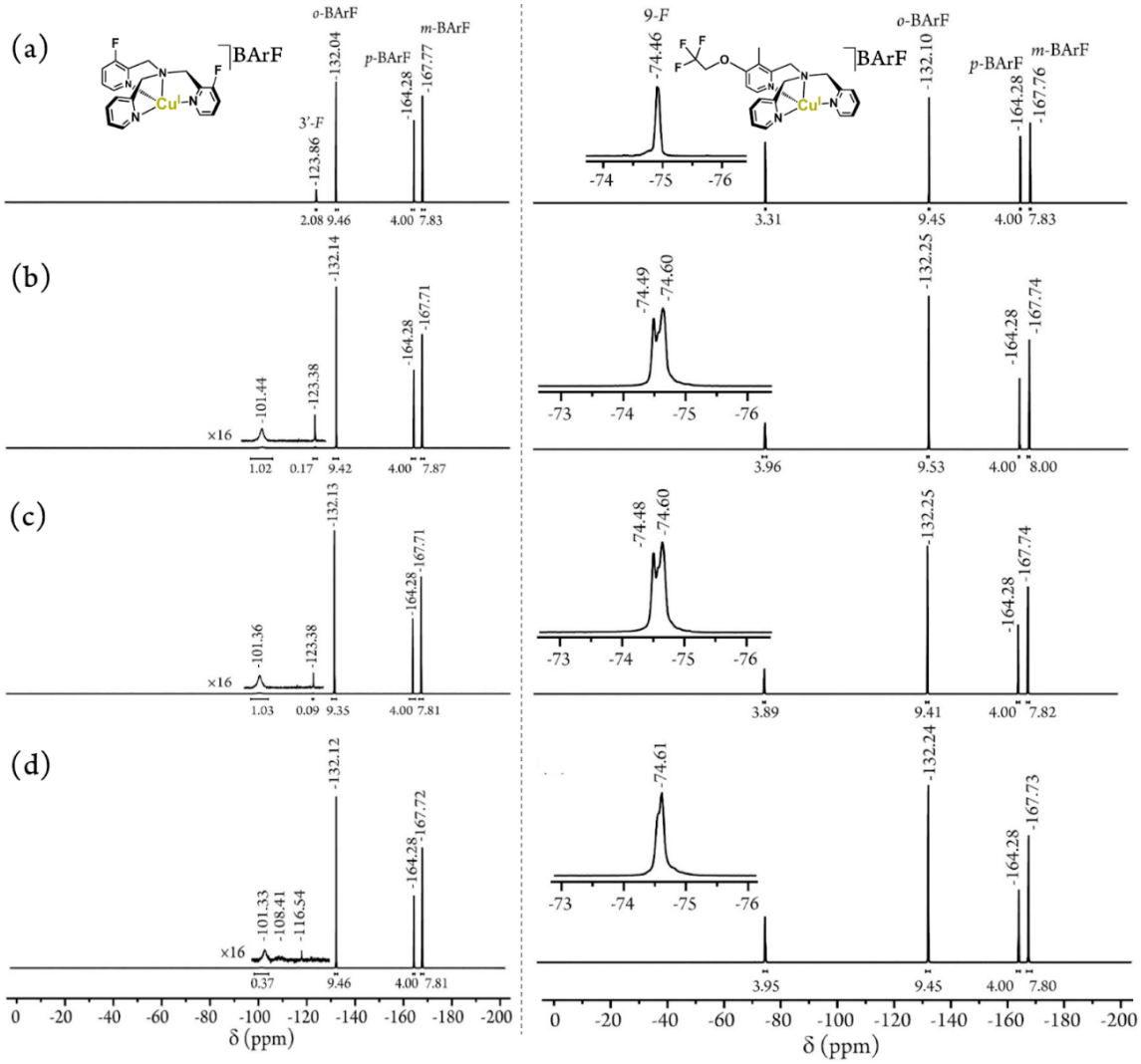

Figure 9. ^{19}F-NMR spectra of the oxygenation reaction of (*left*) [(F_2tmpa)Cu^I][$B(C_6F_5)_4$] and (*right*) [(MeTFE-tmpa)Cu^I][$B(C_6F_5)_4$] at (a) 0 min, (b) 1 min, (c) 15 min, and (d) 6 h in THF-d_8 (470 MHz) at room temperature. Peaks labeled as *o*-BArF, *p*-BArF, and *m*-BArF are for the *ortho*-, *para*-, and *meta*-fluorine atoms of the $[B(C_6F_5)_4]^-$ anion, respectively.

The dioxygen reactivity for [(MeTFE-tmpa)Cu^I][$B(C_6F_5)_4$] in THF-d_8 was also monitored through NMR spectroscopy (Figure 8). The ^{1}H-NMR spectrum of the copper(I) complex also showed four pyridyl proton signals between δ = 8.96 to 7.20 ppm as well as two sharp resonances at δ = 4.73 and δ = 2.17 ppm corresponding to the methylene and methyl protons, respectively.

Here, O_2 bubbling led to a spectral change similar to those observed for the copper(I) complexes of the parent TMPA and its electron deficient derivative, F_2TMPA. The relatively sharp signals at δ = 11.19 and 10.98 along with a series of resonances from 8.20 to 5.85 ppm originate from the μ-peroxo [(MeTFE-tmpa)Cu^{II}–(O_2^{2-})–(MeTFE-tmpa)]$^{2+}$ complex which slowly decomposes over time as observed from the gradual decrease in these signal intensities. The final decomposition product was again a paramagnetic monomer copper(II) species identified by the signals at δ = 13.80, 13.66, 12.52, 10.58, 9.05 ppm along with resonances between 46.59 and 22.07 ppm in the paramagnetic region. It is important to point out the presence of a more complicated ^{1}H-NMR pattern observed for the MeTFE-TMPA oxygenation reaction as compared to those observed for the TMPA or F_2TMPA analogue, possibly due to the lower symmetry of the cupric center or more significant separation of chemical shifts.

The ^{19}F-NMR spectra of the oxygenation of a THF-d_8 solution of [(MeTFE-tmpa)Cu^I][$B(C_6F_5)_4$] were also collected at room temperature (Figure 9). For the starting cuprous complex, the signal for the trifluoroethoxy (TFE) group appeared at δ = –74.46 ppm while the three fluorines of the [$B(C_6F_5)_4$]$^-$ anion were present in the more shielded, aromatic region. Upon dioxygen exposure, the TFE peak transformed into two new fluorine resonances at δ = –74.49 and –74.60 ppm. Over time, the signal at δ = –74.49 ppm gradually disappeared whereas the peak intensity at δ = –74.60 ppm increased. Therefore, the peak at δ = –74.49 ppm was assigned to the TFE-fluorines of the μ-peroxo [(MeTFE-tmpa)Cu^{II}–(O_2^{2-})–(MeTFE-tmpa)]$^{2+}$ complex while the one at δ = –74.60 ppm corresponded to the TFE-fluorines of the final monomeric decomposition product. Here, the difference in ^{19}F-chemical shifts are significantly smaller as compared to those observed in the F_2TMPA analogue, possibly due to the fact that fluorine atoms are further removed from the copper center.

It should be noted that a qualitative comparison of the signal intensities of *trans*-peroxo-dicopper(II) species and the final cupric decomposition product, in both ^{1}H- and ^{19}F-NMR studies (Figures 8 and 9), also support the finding concluded from the UV-vis experiments at room temperature (Figure 5), that is, that the *trans*-peroxo-dicopper(II) species bearing the more electron rich MeTFE-TMPA chelate is more stable as compared to its more electron deficient counterparts bearing either TMPA or F_2TMPA.

3.4. Conclusions

Tagging the two new, remotely substituted, TMPA-based chelates with fluorine and the use of ^{19}F-NMR spectroscopy provided a useful means for probing the oxygenation reactions. This is particularly beneficial for antiferromagnetically coupled species such as the *trans*-peroxo dicopper(II) intermediate in which the sharpness and lack of extensive broadening of the NMR resonances result in their facile detection.

Our spectroscopic and electrochemical studies of the effects of variation in ligand electronic properties on the redox behavior and dioxygen reactivity of the corresponding copper(I) complexes support that ligand electron-donating ability can significantly affect the oxygenation reactions. The relative rates of the formation of the 1:1 (i.e., *end-on* superoxo) and subsequent generation of the 1:2 (i.e., *trans*-peroxo) copper-O_2 intermediates are governed by temperature and ligand electronic effects. For both classes of the copper-dioxygen adducts, the main electronic transitions shift to lower energies as the electron-donating ability of the chelate diminishes. This change in the electronic character of the copper-O_2 core can be explained by the stabilization of d_{z2} orbitals which is consistent with the increase in the reduction potentials.

CHAPTER IV: DIOXYGEN REACTIVITY OF COPPER(I)/MANGANESE(II)-PORPHYRIN ASSEMBLIES

This chapter is adapted from our publication in *Molecules*, "Dioxygen reactivity of copper(I)/manganese(II)-porphyrin assemblies: Mechanistic studies and cooperative activation of O_2" [62].

4.1. Introduction: Copper(I)/Manganese(II)-Porphyrin/Dioxygen Chemistry

Manganese-containing enzymes facilitate a wide variety of biological redox processes through interactions of manganese with dioxygen (O_2) and its reduced derivatives such as superoxide ($O_2^{\bullet-}$) and peroxide (O_2^{2-}) [1–3]. Because of its relative abundance and multiple accessible oxidation states, manganese can facilitate biochemical multielectron redox conversions and is essential for a variety of biological redox processes such as photosynthetic O_2 evolution, antioxidant defense mechanisms regulating reactive oxygen species (ROS), and DNA synthesis [1–4]. Several Mn-containing enzymes involved in facilitating these redox processes include manganese superoxide dismutase (SOD), manganese catalase, the oxygen-evolving complex (OEC) in photosystem II, and Mn/Mn or Mn/Fe ribonucleotide reductase (RNR) [2,3,5]. The nuclearity of such manganese active sites varies, with more complex redox processes typically occurring at multinuclear sites with two or more metal centers [6,7]. Over the years, many Mn-porphyrins have been investigated for their ability to mimic various enzymatic activities or have been used as catalysts to promote a variety of other redox reactions [1,8–21]. An extensively studied example is tetraphenylporphyrin manganese(II), $(TPP)Mn^{II}$, which was used for generating the first dioxygen adduct of a manganese-containing complex [22]. While no reactivity toward O_2 was observed at room temperature, it was found that the complex can be reversibly oxygenated at cryogenic conditions (<−80 °C), forming a manganese(IV) peroxide species, i.e., $[(TPP)Mn^{IV}O_2]^{2-}$

[22,23]. This reactivity significantly differs from those observed for iron(II) or cobalt(II) analogues, which typically produce "superoxide-like" adducts [24,25]. Later, Valentine and co-workers reported the formation of a manganese(III) peroxide adduct, $(TPP)Mn^{III}O_2^{2-}$, through the reaction of equimolar quantities of potassium superoxide (KO_2) and $(TPP)Mn^{II}$ [24,26]. However, the addition of more than one equivalent of the superoxide ion was not reported.

Although O_2 is a highly powerful four-electron oxidant, its one-electron reduction to generate superoxide as the product is relatively disfavored (Scheme 2). Instead, metal/O_2 reactivity typically requires the presence of protons or proceeds through a two-electron step to form a peroxide adduct. The two-electron step may involve O_2 obtaining two electrons from one metal or from two discrete metal centers forming a binuclear μ-peroxo complex [4,5].

Due to the versatility of manganese-O_2 chemistry, the catalytic advantage of multinuclear sites, and the undeniably rich chemistry of copper with dioxygen, in this study, this study investigated the oxygenation chemistry of 1:1 and 1:2 mixtures of a copper(I)/manganese(II)-porphyrin system, i.e., $[(TPP)Mn^{II}]$ (**1**) and $[(tmpa)Cu^{I}(MeCN)][B(C_6F_5)_4]$ (**2**), where TMPA is tris(2-pyridylmethyl)amine.

A very rich chemistry ensued (Scheme 2), wherein there was an initial rapid generation of a cupric-superoxo complex, $[(tmpa)Cu^{II}(O_2^{\bullet-})]^+$ (**3**), as described previously [27–31]. In the reaction mixture, the cupric-superoxo species subsequently reacted with **1**, forming a heterobinuclear O_2-adduct formulated as the μ-peroxo $[(tmpa)Cu^{II}–(O_2^{2-})–Mn^{III}(TPP)]^+$ (**4**) assembly. In the 1:2 mixture, this was followed by the subsequent addition of a second equivalent of **3** to **4**, forming a *bis*-μ-peroxo $[(tmpa)Cu^{II}–(O_2^{2-})–Mn^{IV}(TPP)–(O_2^{2-})–Cu^{II}(tmpa)]^{2+}$ (**7**) species. These two dioxygen-adducts have been characterized by ultraviolet–visible (UV-vis) absorption and nuclear magnetic resonance (NMR) spectroscopies. These bridged peroxo

assemblies (i.e., **4** and **7**) thermally transform to the corresponding μ-oxo and possibly *bis*-μ-oxo complexes, respectively, which, in turn, decompose to $[(TPP)Mn^{III}(MeTHF)_2]^+$, whose X-ray structure is described.

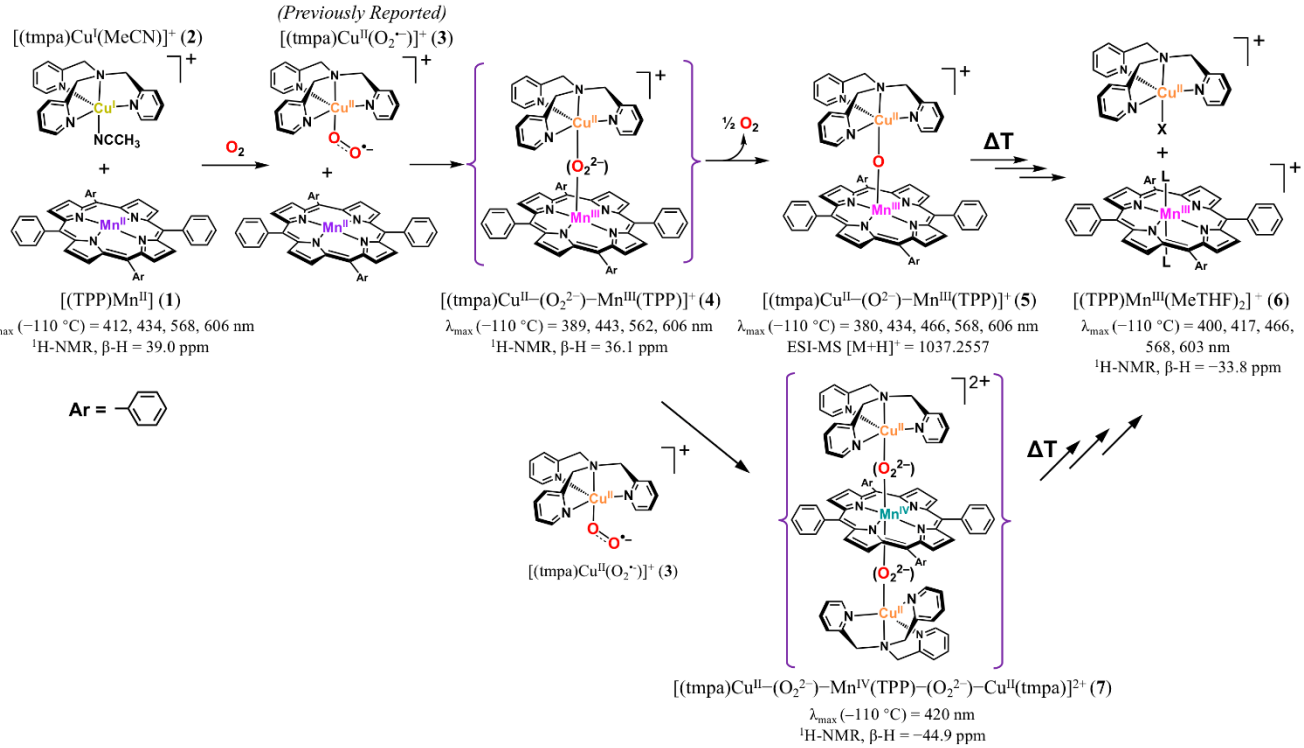

Scheme 2. Proposed reaction steps for the oxygenation of 1:1 and 1:2 mixtures of $[(TPP)Mn^{II}]$ (**1**) and $[(tmpa)Cu^{I}(MeCN)][B(C_6F_5)_4]$ (**2**) in MeTHF leading to the observed products. TPP: Tetraphenylporphyrin; TMPA: Tris(2-pyridylmethyl)amine).

4.2. UV-vis Absorption Spectroscopy

4.2.1. Dioxygen Chemistry of $[(TPP)Mn^{II}]$

In coordinating solvents such as 2-methyltetrahydrofuran (MeTHF), $[(TPP)Mn^{II}]$ is rather unreactive toward O_2 at room temperature. As shown in Figure 10a, despite long O_2 exposure, the UV-vis spectrum of the reaction mixture mostly retained the Soret (433 nm) and Q-band (568 and 606 nm) absorption characteristics of the manganous complex. The UV-vis spectroscopic changes of $[(TPP)Mn^{II}]$ oxygenation in MeTHF at −90 °C are shown in Figure 10b. At low temperature, a

small but noticeable decrease in the 434 nm Soret band, along with the formation of a minor (TPP)Mn^{III} species (λ_{max} = 470 nm), was observed. Allowing the solution to warm to room temperature yielded a product with features at 378, 400, 423, and 470 nm. We posited this final product as a $[(TPP)Mn^{III}(MeTHF)_2]^+$ species, based on its characteristic "split Soret band" and other absorption features similar to those of an authentic MeTHF solution of $[(TPP)Mn^{III}(THF)_2]SbF_6$ (λ_{max} = 377, 399, 418, 467 nm) (Figures B1 and B2) [32–34]. The X-ray structure of $[(TPP)Mn^{III}(MeTHF)_2]SbF_6$, as well as ^{1}H-NMR and IR data further support the identity of this product species as $[(TPP)Mn^{III}(MeTHF)_2]^+$ (vide infra).

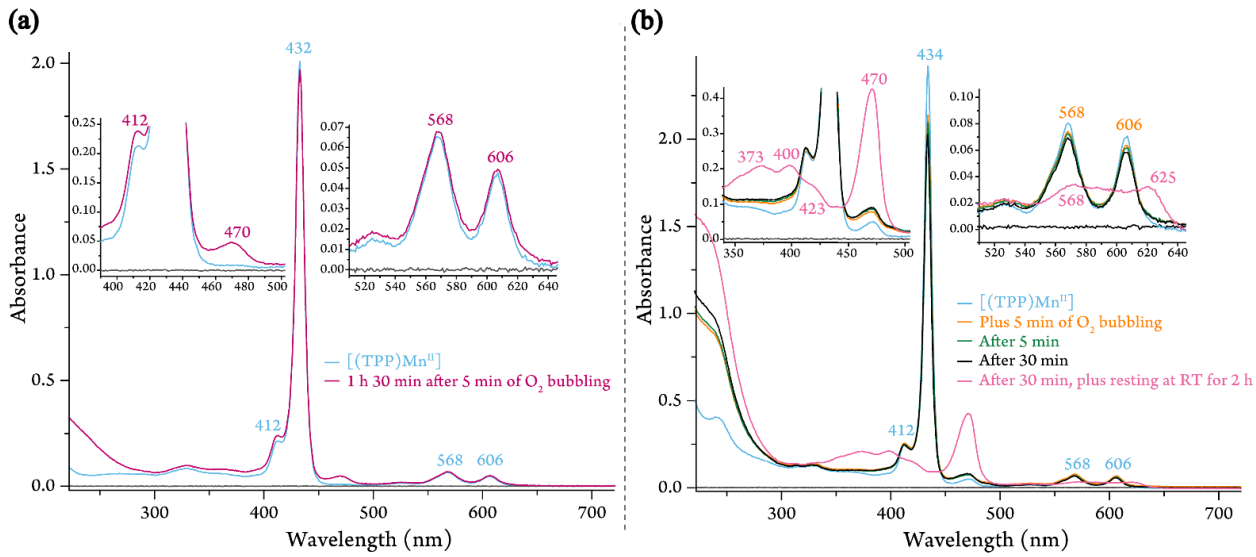

Figure 10. UV-vis spectra of [(TPP)Mn^{II}] in MeTHF in a 4-mm cuvette upon 5 min of O_2 bubbling at: (**a**) room temperature (10 µM), and (**b**) −90 °C (11 µM).

4.2.2. Dioxygen Chemistry of [(TPP)Mn^{II}]/[(tmpa)Cu^{I}(MeCN)][$B(C_6F_5)_4$]

While [(TPP)Mn^{II}] showed no appreciable reactivity toward O_2 at room temperature, remarkably, equimolar amounts of [(TPP)Mn^{II}] and [(tmpa)Cu^{I}(MeCN)][$B(C_6F_5)_4$] immediately reacted with O_2 to produce a new species (Figure 11a), now to be referred to as the μ-oxo Mn^{III}/Cu^{II}

assembly, as monitored by UV-vis spectroscopy (λ_{max} = 432 and 466 nm). The nature of this bridged complex was further supported by ESI-MS and ^{1}H-NMR results, vide infra. This complex gradually decomposes to a final (TPP)Mn^{III} species (λ_{max} = 470 nm) with features similar to that of the [(TPP)Mn^{II}] oxygenation product, i.e., [(TPP)Mn^{III}(MeTHF)$_2$]$^+$.

Investigations of the independent O_2 chemistry for the copper complex, [(tmpa)Cu^I(MeCN)][B(C_6F_5)$_4$], have been described previously [28,30]. The O_2 adduct observed from low-temperature reactions of this copper complex bearing the tripodal TMPA ligand with O_2 was solvent-, temperature-, and concentration-dependent (Cu/O_2 = 1:1 or 2:1). Upon initial binding of O_2 to [(tmpa)Cu^I(MeCN)]$^+$, an end-on cupric η^1-superoxo intermediate, [(tmpa)Cu^{II}($O_2^{\bullet-}$)]$^+$, formed via single electron transfer from the cuprous center to the ligated dioxygen moiety. At higher concentrations of the copper complex solution, and/or higher reaction temperatures, a second cuprous center provided the second electron, generating a dicopper end-on μ-*1,2*-peroxo species, [(tmpa)Cu^{II}–(O_2^{2-})–Cu^{II}(tmpa)]$^{2+}$.

With this background, we investigated the oxygenation of an equimolar mixture of [(TPP)Mn^{II}] and [(tmpa)Cu^I(MeCN)][B(C_6F_5)$_4$] at low temperatures. At −110 °C, bubbling with dioxygen immediately produced a metastable O_2-adduct with new spectral features at 389, 443, 562, and 606 nm (Figure 11b). We formulated this as a heterobinuclear peroxo complex, [(tmpa)Cu^{II}–(O_2^{2-})–Mn^{III}(TPP)]$^+$. The reaction proceeded through initial formation of a cupric superoxo species, [(tmpa)Cu^{II}($O_2^{\bullet-}$)]$^+$, followed by a fast electron transfer from the manganous center to the superoxide moiety, forming the bridged peroxo species. This μ-peroxo Mn^{III}/Cu^{II} complex was not stable at higher temperatures, primarily leading to the formation of a μ-oxo complex, [(tmpa)Cu^{II}–O–Mn^{III}(TPP)]$^+$. By analogy to the process shown to occur in similar bridged peroxo systems, it was presumed that this transformation occurred through a

disproportionation reaction of two μ-peroxo species that generated two μ-oxo complexes and releases of O_2 [27,35].

Warming the μ-peroxo complex, $[(tmpa)Cu^{II}–(O_2^{2-})–Mn^{III}(TPP)]^+$, to room temperature leads to the formation of the μ-oxo complex that subsequently converts to $[(TPP)Mn^{III}(MeTHF)_2]^+$, i.e., the identical $(TPP)Mn^{III}$ product obtained from the oxygenation experiment at room temperature.

It is important to note that, under the given experimental conditions, i.e., low temperature (−110 °C) and low concentration (μM range), the oxygenation reaction of $[(tmpa)Cu^{I}(MeCN)][B(C_6F_5)_4]$ exclusively resulted in the formation of the cupric superoxo species [29,30,36]. This strongly suggests that the electron transfer from a second cuprous complex to $[(tmpa)Cu^{II}(O_2^{\bullet-})]^+$ is significantly less favored than from a $[(TPP)Mn^{II}]$ complex. We can, therefore, rule out the formation of the dicopper peroxo species, i.e., $[(tmpa)Cu^{II}–(O_2^{2-})–Cu^{II}(tmpa)]^{2+}$, in our experiments, independent of the experimental conditions.

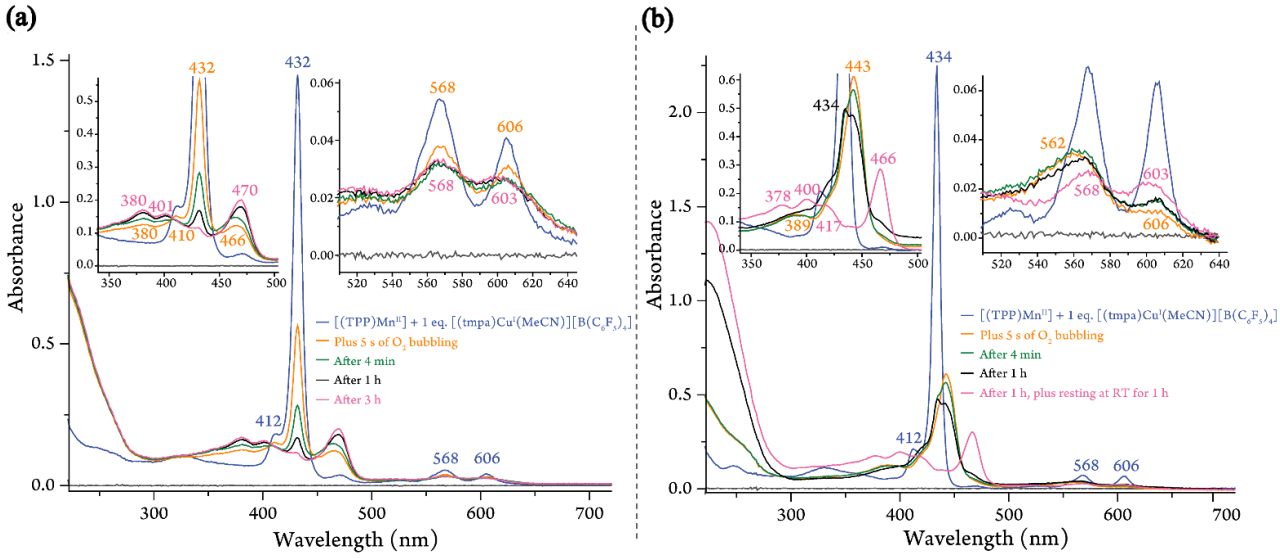

Figure 11. UV-vis spectra of the oxygenation reaction of 1:1 mixture of $[(TPP)Mn^{II}]$ and $[(tmpa)Cu^{I}(MeCN)][B(C_6F_5)_4]$ in MeTHF in a 4-mm cuvette at: (**a**) room temperature (7 μM), and (**b**) −110 °C (8 μM).

4.2.3. Dioxygen Chemistry of [(TPP)Mn^{II}]/2 [(tmpa)Cu^{I}(MeCN)][$B(C_6F_5)_4$]

The remaining question about the capability of the manganese(II) porphyrin precursor to react with more than an equimolar amount of the superoxide was addressed by reacting a 1:2 mixture of [(TPP)Mn^{II}] and [(tmpa)Cu^{I}(MeCN)][$B(C_6F_5)_4$] with dioxygen. Here, at room temperature, the oxygenation reaction and formation of the final solvated (TPP)Mn^{III} product were faster compared with those of an equimolar mixture, with nearly all [(TPP)$Mn^{III}$$(MeTHF)_2]^+$ formed within 1 h after O_2 bubbling rather than over the 3 h observed for the 1:1 mixture (Figures 2a and 3a).

The same reaction was repeated at −110 °C, where we were able to detect two intermediates. Low temperature oxygenation of the 1:2 mixture leads to rapid formation of the *μ*-peroxo [(TPP)Mn^{III}–(O_2^{2-})–Cu^{II}(tmpa)]$^+$ intermediate (λ_{max} = 443 nm), identical to that observed during the reaction of the 1:1 mixture with O_2, vide supra. This *μ*-peroxo Mn^{III}/Cu^{II} intermediate then reacted with a second cupric superoxo species, [(tmpa)$Cu^{II}$$(O_2^{\bullet-})]^+$, on the open face of the Mn-porphyrin (Scheme 2) and isosbestically converted to a *bis*-*μ*-peroxo adduct with λ_{max} = 420 nm, i.e., [(tmpa)Cu^{II}–(O_2^{2-})–Mn^{IV}(TPP)–(O_2^{2-})–Cu^{II}(tmpa)]$^{2+}$ (Figure 12b). The characteristic single blue-shifted Soret absorption at 420 nm and other spectral features of this new species agreed with those of previously reported [(TPP)$Mn^{IV}$$(L)_2]$ species (Table 3), supporting the oxidation state of manganese(IV) in this intermediate [17,37–39]. Further indication that the *bis*-*μ*-peroxo intermediate is a manganese(IV) complex was derived from the resonance observed for its pyrrolic protons using ^{1}H-NMR spectroscopy, vide infra. Upon warming, the *bis*-*μ*-peroxo intermediate may disproportionate to form a *bis*-*μ*-oxo adduct, [(tmpa)Cu^{II}–O–Mn^{IV}(TPP)–O–Cu^{II}(tmpa)]$^{2+}$, which can subsequently decompose to the observed (TPP)Mn^{III} product, [(TPP)$Mn^{III}$$(MeTHF)_2]^+$ (Figure 12b).

It is worth mentioning that quantitative analyses of UV-vis spectra of the oxygenation products of [(TPP)Mn^{II}] in the presence of 0 to 2 equivalents of [(tmpa)Cu^{I}(MeCN)]$^{+}$, at either low or room temperature, confirmed the generation of one equivalent of the final product, [(TPP)Mn^{III}(MeTHF)$_2$]$^{+}$, with features near 380, 400, and 470 nm in high yields (~100% yield).

Table 3. Examples of UV-vis absorption features reported for Mn^{IV} complexes bearing TPP-based ligands.

Complex *	Solvent	λ_{max} (nm)	Reference
{(TPP)Mn^{IV}[(O_2^{2-})Cu^{II}(tmpa)]$_2$}$^{2+}$ (**7**)	MeTHF	420	This work
[(TPP)Mn^{IV}(OCH_3)$_2$]	methanol	360, 420, 520	[40]
[Cl(TPP)Mn^{IV}(OIPh)]$_2$O	chlorobenzene	421, 502	[41]
[(TMP)Mn^{IV}(O)(OH)]	DCM	422	[8]
[(TMP)$Mn^{IV}$$Cl_2$]	DCM benzene	420, 530, 620, 720 420, 535, 720	[42]

* TPP: Tetraphenylporphyrin; TMPA: Tris(2-pyridylmethyl)amine); TMP: Tetramesitylporphyrin.

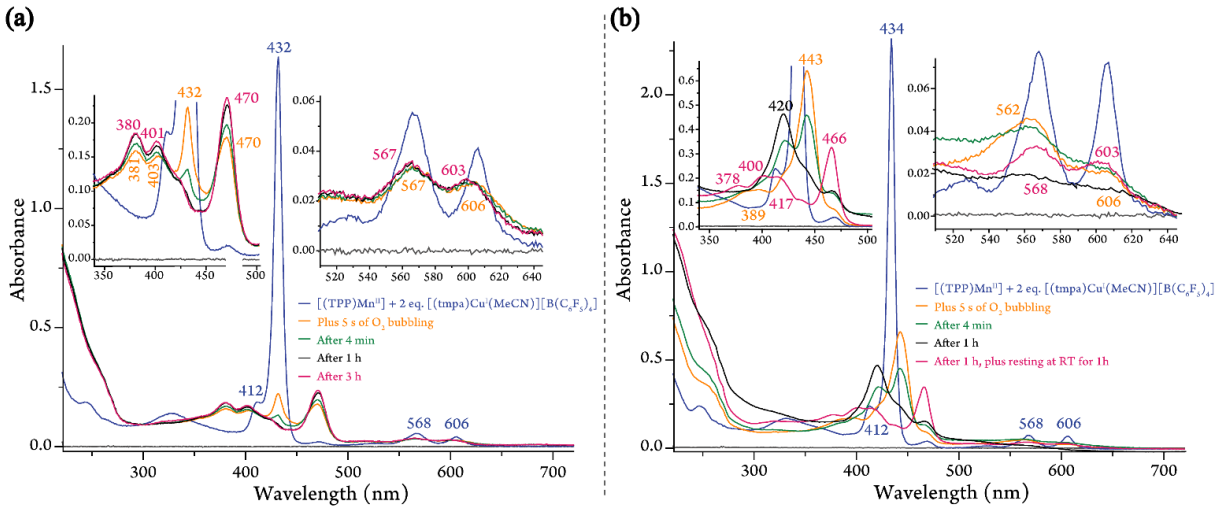

Figure 12. UV-vis spectra of the oxygenation reaction of 1:2 mixture of [(TPP)Mn^{II}] and [(tmpa)Cu^{I}(MeCN)][B(C_6F_5)$_4$] in MeTHF in a 4-mm cuvette at: (**a**) room temperature (7 μM), and (**b**) −110 °C (8 μM).

4.3. X-ray Structure of [(TPP)Mn^{III}(MeTHF)$_2$]SbF_6

The molecular structure of an authentic sample of the proposed final product, [(TPP)Mn^{III}(MeTHF)$_2$]$^{+}$, was obtained. Dark red crystals of [(TPP)Mn^{III}(MeTHF)$_2$]SbF_6·2MeTHF were grown by slow diffusion of heptane into a MeTHF solution of [(TPP)Mn^{III}(THF)$_2$]SbF_6 (Table

B1). The complex crystallizes in a tetragonal crystal system with the $P4_32_12$ space group. A perspective view of the complex, along with the selected structural and geometrical parameters, are given in Figure 13; the molecular packing in the unit cell is shown in Figure B3. The hexacoordinate Mn center lies perfectly in the plane of the porphyrin and is axially ligated by two MeTHF molecules. The length of the bond between the manganese and the axially-ligated MeTHF molecule, Mn−O_{ax},, of 2.272(3) Å was within the range reported for other hexacoordinate Mn(III) porphyrins with two O-based ligands (Table B2) [43–48]. Moreover, the longer Mn−O_{ax} distances, as compared to Mn−N_{por} (i.e., average of 2.008 Å) were in accord with the presence of a high-spin tetragonally elongated Mn(III) center. The elongation of the bonds to the axial oxygen sites has been ascribed to a singly occupied axially antibonding d_z^2 orbital that renders a ground electronic state of $(d_{xz},d_{yz})^2(d_{xy})^1(d_{z2})^1$ [49–51].

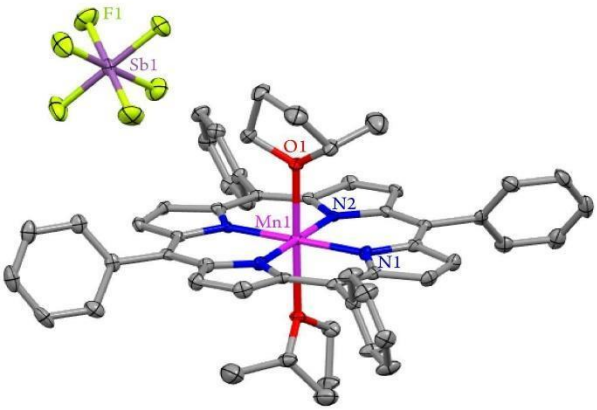

Figure 13. Displacement ellipsoid plot (50% probability level) of $[(TPP)Mn^{III}(MeTHF)_2]SbF_6$ at 100(2) K, showing the atom-labeling scheme. Hydrogen atoms and solvent molecules have been omitted for clarity. Selected bond lengths (Å) and angles (deg): Mn(1)-O(1), 2.272(3); Mn(1)-N(1), 2.007(4); Mn(1)-N(2), 2.008(4); O(1)-Mn(1)-O(1a), 177.51(17); N(1)-Mn(1)-N(2), 90.15(17); N(1)-Mn(1)-N(1a), 89.8(2); N(1)-Mn(1)-N(2a), 179.91(19); N(1)-Mn(1)-O(1), 88.43(14); N(1)-Mn(1)-O(1a), 89.81(14); N(2)-Mn(1)-N(2a), 89.9(2); N(2)-Mn(1)-O(1), 90.21(14); N(2)-Mn(1)-O(1a), 91.55(14); N(1a)-Mn(1)-O(1), 89.80(14); N(2a)-Mn(1)-O(1), 91.55(14).

4.4. Nuclear Magnetic Resonance (NMR) Spectroscopy

The oxygenation reactions of 1:1 and 1:2 mixtures of [(TPP)Mn^{II}] and [(tmpa)Cu^{I}(MeCN)]$^{+}$ were monitored by ^{1}H-NMR spectroscopy at room temperature. In both cases, NMR data support the formation of copper-bound manganese porphyrin intermediates, as well as the identity of [(TPP)Mn^{III}(MeTHF)$_2$]$^{+}$ as the final product. Here, the resonances of the *β*-pyrrole protons can aid manganese oxidation and spin-state assignments. Our tentative assignments of the pyrrolic peaks are based on analogy to values reported in the literature or comparison with authentic samples (Figures B4–B10).

The ^{1}H-NMR spectrum of an equimolar mixture of [(TPP)Mn^{II}] and [(tmpa)Cu^{I}(MeCN)]$^{+}$ in THF-d_8 displays distinct signals originating from individual reduced complexes. The broad peak at δ = 39.04 ppm corresponds to the *β*-pyrrole protons of the Mn(II) species while the broad signal at δ = 8.02 ppm originates from the *meso*-aryl protons in [(TPP)Mn^{II}] (Figures 5 Left and B11a Left). The peaks at δ = 8.60, 7.74, and 7.34 ppm arise from the pyridyl groups of [(tmpa)Cu^{I}(MeCN)][B(C_6F_5)$_4$] (Figure B11a Left). The peak assignments were obtained by comparing the ^{1}H-NMR spectral pattern of the reaction mixture with the individual spectra of the reduced complexes (Figures B6 and B10).

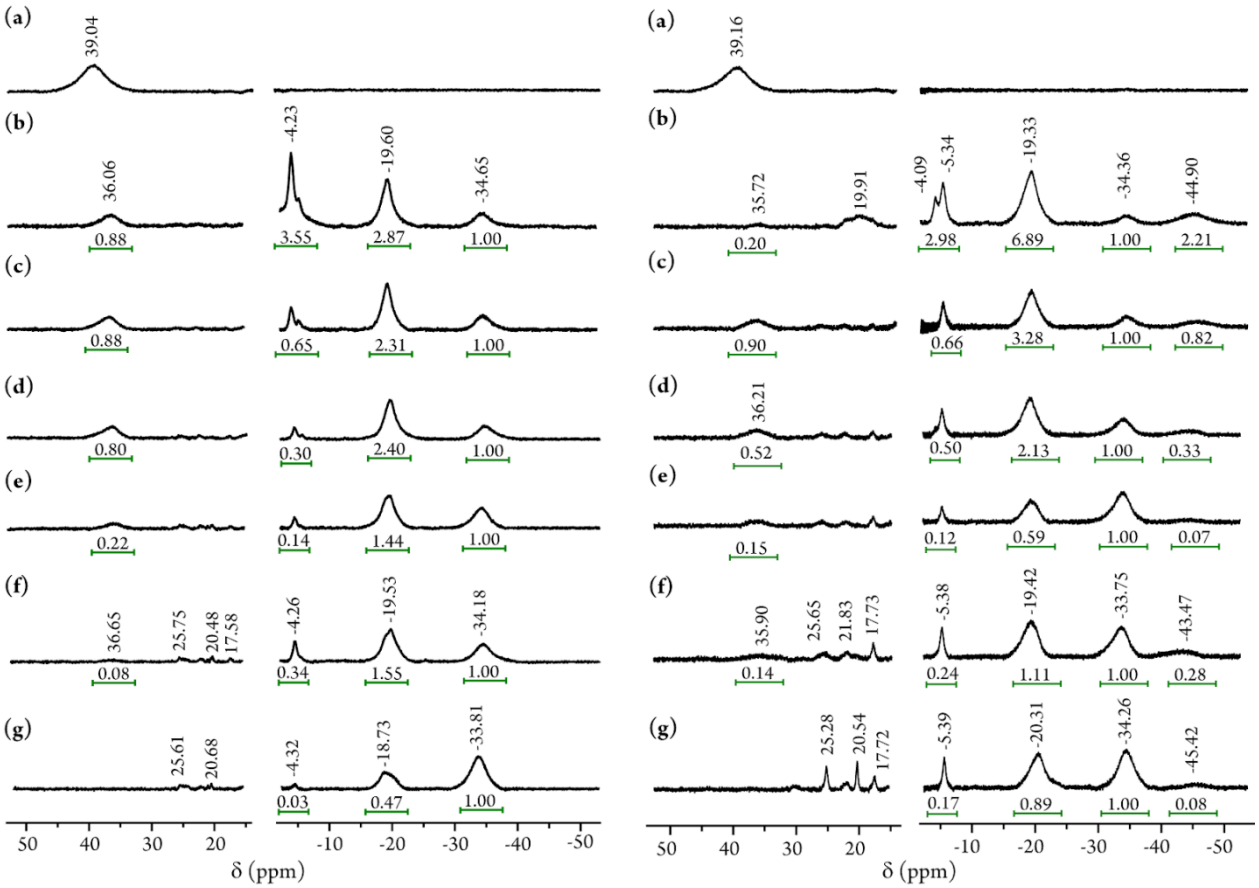

Figure 14. Parts of the ^{1}H-NMR spectra of the oxygenation reaction of a 1:1 mixture, (**Left**), and 1:2 mixture, (**Right**), of [(TPP)Mn^{II}] and [(tmpa)Cu^{I}(MeCN)][B(C_6F_5)$_4$] (THF-d_8, room temperature) at different time intervals: (**a**) 0 min, (**b**) 1 min, (**c**) 15 min, (**d**) 1 h 30 min, (**e**) 4 h 30 min, (**f**) 6 h, and (**g**) 18 h. The peak for [(TPP)Mn^{III}(THF)$_2$]$^+$ at δ = −34.65 ppm was set as the reference for comparing peak areas.

Upon O_2 bubbling, several new signals appeared in the upfield and downfield regions in the spectrum, which resulted from oxidation of the two metal centers (Figures 5 Left and B11). After 1 min of O_2 bubbling, the ^{1}H-NMR spectrum showed a distinct pyrrolic peak at δ = 36.06 ppm, which corresponds to the presence of a peroxo Mn(III) center [24,52], in agreement with our UV-vis spectroscopic results (vide supra). This proposed μ-peroxo Mn^{III}/Cu^{II} intermediate was unstable and the corresponding pyrrolic resonance disappeared over time (Figure 14 Left).

The upfield region displayed the three most intense peaks at δ = −4.23, −19.60, and −34.65 ppm. The signal at δ = −4.23 ppm likely originated from the TMPA moiety of the attached copper center as the significant upfield shift of this peak indicated that the protons of this chelate were directly located above the porphyrin core, as observed in similar oxo-bridged heterobinuclear systems [53–55]. The second upfield broad signal at δ = −19.60 ppm could be ascribed to $[(TPP)Mn^{III}–O–Cu^{II}(tmpa)]^+$ and may correspond to a combination of the pyrrolic, as well as part of the attached, TMPA protons. The third upfield signal at δ = −34.65 ppm corresponded to the pyrrolic protons of $[(TPP)Mn^{III}(THF)_2]^+$ in the reaction mixture, which was identical to that of the authentic $[(TPP)Mn^{III}(THF)_2]^+$ sample, confirming the presence of a high-spin (S = 2) Mn(III) center (Figure B8). All proton peaks were integrated with respect to the δ = −34.65 ppm peak for relative comparisons. As the reaction progressed, the signal at δ = −34.65 ppm continued growing and the intensities of the other signals in the upfield region decreased, which suggested decomposition to $[(TPP)Mn^{III}(THF)_2]^+$, consistent with the overall reactivity patterns observed in our UV-vis studies. Appearance of the small peaks in the δ = 10 to 26 ppm region over time (Figures 5 Left and B11b–g Left) that correspond to the TMPA protons in a free $[(tmpa)Cu^{II}(X)]^+$ complex [53] further confirmed the dissociation of the Mn/Cu assembly.

To further support our supposition that an individual homobinuclear copper species did not form during the oxygenation of the mixture of manganese and copper complexes, we also monitored the independent dioxygen reactivity of $[(tmpa)Cu^{I}(MeCN)][B(C_6F_5)_4]$ through ^{1}H-NMR spectroscopy (Figures B12 and B13). The cuprous complex showed three distinct signals between δ = 8.84 and 7.48 ppm, corresponding to the protons of the pyridyl arms, while the methyl-protons resonated at δ = 4.53 ppm. Bubbling with O_2 led to the formation of a dioxygen adduct with new features. The pyridyl signals appeared at δ = 11.02, 8.16, 8.11, and 7.79 ppm, while the

methyl-protons resonated at δ = 5.80; this spectral pattern agrees with the presence of the μ-peroxo $[(tmpa)Cu^{II}–(O_2^{2–})–Cu^{II}(tmpa)]^{2+}$ complex in the reaction mixture [56]. The spectrum also showed an additional peak at δ = 10.39 ppm, which corresponded to the pyridyl protons of a $[(tmpa)Cu^{II}(X)]^{+}$ species [53]. Within a couple of hours, the μ-peroxo complex fully decomposed into the $[(tmpa)Cu^{II}]^{+}$ species, as evidenced by the gradual disappearance of the peroxo species signals and concomitant growth of the δ = 10.39 ppm peak. No proton signals in the negative region were observed throughout the oxygenation reaction of the cuprous complex; the final cupric complex only displayed proton signals in the downfield region.

The ^{1}H-NMR spectral pattern obtained for a 1:2 mixture of $[(TPP)Mn^{II}]$ and $[(tmpa)Cu^{I}(MeCN)][B(C_6F_5)_4]$ was quite similar to that obtained for their equimolar mixture, aside from the expected higher relative peak intensities observed for the pyridyl-protons of the cuprous complex (δ = 8.62, 7.73, and 7.35 ppm) as compared to the *meso*-aryl protons (δ = 8.02 ppm) of the porphyrin ring (Figure S11a Right). Moreover, the very broad -CH_2- signal of $(tmpa)Cu^{I}$ appeared at δ = 3.99 ppm. Similarly, dioxygen was bubbled through the 1:2 reaction mixture and the proton NMR spectra were recorded at different time intervals (Figures 5 Right and B11b–g Right). After one minute, the sample exhibited a series of new peaks in both upfield and downfield regions. While some of the spectral features were similar to those observed for the oxygenation of the 1:1 reaction mixture, there were a few important differences. A broad peak at δ = −44.90 ppm was observed, which could be ascribed to the β-pyrrole protons of a high-spin (S = 3/2) Mn(IV) center [37,42], possibly $[(tmpa)Cu^{II}–(O_2^{2–})–Mn^{IV}(TPP)–(O_2^{2–})–Cu^{II}(tmpa)]^{2+}$ or the *bis*-μ-oxo adduct. This broad peak is absent during oxygenation of a 1:1 reaction mixture; this finding is in agreement with our supposition concerning the formation of a manganese(IV) species during the oxygenation reaction mixture only when an additional equivalent $[(tmpa)Cu^{II}(O_2^{\bullet–})]^{+}$ is present,

thus, promoting the second electron transfer. This peak at δ = −44.90 slowly disappeared with a concurrent increase of the peak at δ = −34.36 ppm over the course of the reaction, hinting towards the decomposition of the Mn(IV) assembly into the (TPP)Mn^{III} species. As expected, the TMPA signals associated with a free [(tmpa)Cu^{II}(X)]$^+$ complex (possibly X = OH^-) in the δ = 10 to 26 ppm region appeared at higher intensity (Figures 5 Right and B11b–g Right), further supporting the dissociation of the Mn/Cu assembly.

4.5. Electrospray Ionization Mass Spectrometry (ESI-MS)

The formation of the μ-oxo [(TPP)Mn^{III}–O–Cu^{II}(tmpa)]$^+$ complex was further confirmed by ESI-MS studies. The ESI-MS spectrum of a 1:1 mixture of [(TPP)Mn^{II}] and [(MeCN)Cu^{I}(tmpa)][$B(C_6F_5)_4$] in MeTHF immediately after bubbling with O_2 at room temperature showed a peak for [(TPP)Mn^{II}–OH–Cu^{II}(tmpa)]$^+$ at *m*/*z* 1037.2557. The isotopic distribution pattern of the experimental mass correlated well with theory (Figure 15), which further confirms the formation of the Mn/Cu assembly. To try to provide further insight, the oxygenation of a 1:2 mixture of the reduced complexes did not lead to the mass spectrometric detection of a *bis*-μ-oxo adduct, most likely due to its even lower stability and, therefore, easier reduction/fragmentation.

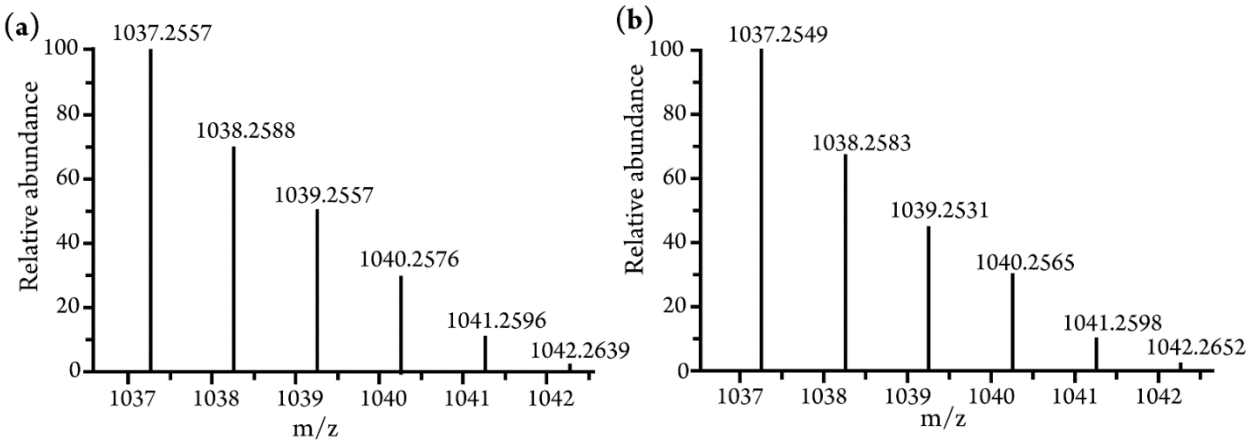

Figure 15. Isotopic distribution pattern of the (a) experimental, and (b) simulated ESI-MS spectra of [(TPP)Mn–O–Cu(tmpa)+H]+. The sample was prepared in MeTHF and recorded in positive-ion mode with a source voltage of 1.0 kV.

4.6. Fourier-Transform Infrared Spectroscopy (FT-IR)

IR spectroscopy also supports the formation of the same final oxygenation product, i.e., $[(TPP)Mn^{III}(MeTHF)_2]^+$, for 1:1, as well as 1:2, mixtures of $[(TPP)Mn^{II}]$ and $[(tmpa)Cu^{I}(MeCN)][B(C_6F_5)_4]$ (Figures S14–17). The presence of bound MeTHF in $[(TPP)Mn^{III}(MeTHF)_2]^+$ was confirmed by C-H stretching bands at or near 2966 and 2864 cm^{-1}. The high-frequency metal-sensitive IR bands of the TPP complexes have been previously found to, slightly but regularly, vary depending on the nature of the metal ion [57]. Here, the metal-sensitive TPP bands at 1598, 1487, 1342, and 1010 cm^{-1} were identical or within 2 cm^{-1} for the 1:1 and 1:2 oxygenation products, and similar to those of authentic $[(TPP)Mn^{III}(MeTHF)_2]SbF_6$ (Table B3), further confirming the presence of a Mn(III) center.

4.7. Conclusions

The foregoing results demonstrate the cooperative activation of dioxygen by the copper(I)/manganese(II)-porphyrin systems. A combined array of variable-temperature UV-vis,

NMR, IR as well as ESI-MS and X-ray crystallographic analyses collectively demonstrated that [(TPP)Mn^{II}] reacts with O_2 in the presence of 0 to 2 equivalents of a cuprous chelate, [(tmpa)Cu^{I}(MeCN)]$^+$, in MeTHF to produce a common final decomposition product, [(TPP)Mn^{III}(MeTHF)$_2$]$^+$. However, the O_2 reactivity in the presence of the copper(I) center is remarkably faster and proceeds through a distinct mechanism. As evidenced by low temperature (−110 °C) UV-vis and room temperature ^{1}H-NMR measurements, copper(I) is responsible for the binding and initial activation of dioxygen, forming a cupric superoxo intermediate, [(tmpa)Cu^{II}($O_2^{\bullet-}$)]$^+$. This is followed by an electron transfer from the manganous complex generating a bridged heterobinuclear peroxo species, [(tmpa)Cu^{II}–(O_2^{2-})–Mn^{III}(TPP)]$^+$. In the presence of a second equivalent of the cupric superoxo complex, an additional electron transfer from the Mn(III) center of the μ-peroxo assembly to the superoxo species takes place, forming a *bis*-μ-peroxo assembly, [(tmpa)Cu^{II}–(O_2^{2-})–Mn^{IV}(TPP)–(O_2^{2-})–Cu^{II}(tmpa)]$^{2+}$. These systems represent the first examples of such Mn/Cu/O_2 adducts and illustrate the importance of cooperative activation of O_2 in the heteromultimetallic systems. Experiments designed to further investigate these dioxygen-adducts are currently in hand.

REFERENCES

References for "CHAPTER I: Introduction: Dioxygen Chemistry"

1. Zhang, W.; Lai, W.; Cao, R. *Chem. Rev.* **2017**, 117, 3717– 3797. https://doi.org/10.1021/acs.chemrev.6b00299.
2. *Angew. Chem., Int. Ed*. **2011**, 50, 11570– 11572. https://doi.org/10.1002/anie.201106166.
3. Adam, S. M.; Wijeratne, G. B.; Rogler, P. J.; Diaz, D. E.; Quist, D. A.; Liu, J. J.; Karlin, K. D. *Chem. Rev.* **2018**, 118, 22, 10840-11022. https://doi.org/10.1021/acs.chemrev.8b00074.
4. Mano, N.; De Poulpiquet, A. *Chem. Rev*. **2018**, *118*, 2392. https://doi.org/10.1021/acs.chemrev.7b00220.
5. Bhagi-Damodaran, A.; Michael, M. A.; Zhu, Q.; Reed, J.; Sandoval, B. A.; Mirts, E. N.; Chakraborty, S.; Moenne-Loccoz, P.; Zhang, Y.; Lu, Y. *Nat. Chem*. **2017**, 257-263. https://doi.org/10.1038/nchem.2643.
6. Li, R.; Khan, F.S.T.; Tapia, M.; Hematian, S. *J. Coord. Chem.* **2022**, *75*:11-14, 1617-1635, https://doi.org/10.1080/00958972.2022.2107429.
7. Li, R.; Khan, F.S.T.; Hematian, S. *Molecules.* **2022**, *27*, 1000. https://doi.org/10.3390/molecules27031000.

References for "CHAPTER II: Materials and Methods"

1. R.R. Jacobson, Z. Tyeklar, A. Farooq, K.D. Karlin, S. Liu, J. Zubieta. *J. Am. Chem. Soc.*, **110**, 3690 (1988). [Crossref], [Web of Science ®], [Google Scholar]
2. S. Hematian, M.A. Siegler, K.D. Karlin. *J. Am. Chem. Soc.*, **134**, 18912 (2012). [Crossref], [PubMed], [Web of Science ®], [Google Scholar]
3. Hematian, S.; Siegler, M.A.; Karlin, K.D. Heme/Copper Assembly Mediated Nitrite and Nitric Oxide Interconversion. *J. Am. Chem. Soc.* **2012**, *134*, 18912–18915. [**Google Scholar**] [**CrossRef**] [**PubMed**][**Green Version**]
4. Adler, A.D.; Longo, F.R.; Kampas, F.; Kim, J. On the Preparation of Metalloporphyrins. *J. Inorg. Nucl. Chem.* **1970**, *32*, 2443–2445. [**Google Scholar**] [**CrossRef**]
5. Ghiladi, R.A.; Kretzer, R.M.; Guzei, I.; Rheingold, A.L.; Neuhold, Y.-M.; Hatwell, K.R.; Zuberbühler, A.D.; Karlin, K.D. (F_8TPP)Fe^{II}/O_2 Reactivity Studies {F_8TPP = Tetrakis(2,6-difluorophenyl)porphyrinate(2−)}: Spectroscopic (UV−Visible and NMR) and Kinetic Study of Solvent-Dependent (Fe/O_2 = 1:1 or 2:1) Reversible O_2-Reduction and Ferryl Formation. *Inorg. Chem.* **2001**, *40*, 5754–5767. [**Google Scholar**] [**CrossRef**]
6. Hematian, S.; Siegler, M.A.; Karlin, K.D. Nitric Oxide Generation from Heme/Copper Assembly Mediated Nitrite Reductase Activity. *J. Biol. Inorg. Chem.* **2014**, *19*, 515–528. [**Google Scholar**] [**CrossRef**] [**PubMed**]

7. Fox, S.J.; Chen, L.; Khan, M.A.; Richter-Addo, G.B. Nitrosoarene Complexes of Manganese Porphyrins. *Inorg. Chem.* **1997**, *36*, 6465–6467. [**Google Scholar**] [**CrossRef**]
8. G.M. Sheldrick. *SHELXL-2018: Program for Crystal Structure Refinement*, University of GöTtingen, GöTtingen, Germany (2018). [Google Scholar]
9. F.S.T. Khan, A.L. Waldbusser, M.C. Carrasco, H. Pourhadi, S. Hematian. *Dalton Trans.*, **50**, 7433 (2021). [Crossref], [PubMed], [Google Scholar]
10. Tyeklar, Z.; Jacobson, R.R.; Wei, N.; Murthy, N.N.; Zubieta, J.; Karlin, K.D. Reversible Reaction of Dioxygen (and Carbon Monoxide) with a Copper(I) Complex. X-ray Structures of Relevant Mononuclear Cu(I) Precursor Adducts and the Trans-(μ-1,2-peroxo)dicopper(II) Product. *J. Am. Chem. Soc.* **1993**, *115*, 2677–2689. [**Google Scholar**] [**CrossRef**]

References for "CHAPTER III: Dioxygen Reactivity of Copper(I) Complexes"

1. R. Trammell, K. Rajabimoghadam, I. Garcia-Bosch. *Chem. Rev.*, **119**, 2954 (2019). [Crossref], [PubMed], [Web of Science ®], [Google Scholar]
2. E.I. Solomon, D.E. Heppner, E.M. Johnston, J.W. Ginsbach, J. Cirera, M. Qayyum, M.T. Kieber-Emmons, C.H. Kjaergaard, R.G. Hadt, L. Tian. *Chem. Rev.*, **114**, 3659 (2014). [Crossref], [PubMed], [Web of Science ®], [Google Scholar]
3. S.E. Allen, R.R. Walvoord, R. Padilla-Salinas, M.C. Kozlowski. *Chem. Rev.*, **113**, 6234 (2013). [Crossref], [PubMed], [Web of Science ®], [Google Scholar]
4. E.A. Lewis, W.B. Tolman. *Chem. Rev.*, **104**, 1047 (2004). [Crossref], [PubMed], [Web of Science ®], [Google Scholar]
5. K.D. Karlin, S. Kaderli, A.D. Zuberbühler. *Acc. Chem. Res.*, **30**, 139 (1997). [Crossref], [Web of Science ®], [Google Scholar]
6. D.A. Quist, D.E. Diaz, J.J. Liu, K.D. Karlin. *J. Biol. Inorg. Chem.*, **22**, 253 (2017). [Crossref], [PubMed], [Web of Science ®], [Google Scholar]
7. E.I. Solomon, J.W. Ginsbach, D.E. Heppner, M.T. Kieber-Emmons, C.H. Kjaergaard, P.J. Smeets, L. Tian, J.S. Woertink. *Faraday Discuss*, **148**, 11 (2011). [Crossref], [PubMed], [Google Scholar]
8. J.P. Klinman. *Chem. Rev.*, **96**, 2541 (1996). [Crossref], [PubMed], [Web of Science ®], [Google Scholar]
9. R. Davydov, A.E. Herzog, R.J. Jodts, K.D. Karlin, B.M. Hoffman. *J Am Chem Soc*, **144**, 377 (2022). [Crossref], [PubMed], [Google Scholar]
10. S.M. Adam, G.B. Wijeratne, P.J. Rogler, D.E. Diaz, D.A. Quist, J.J. Liu, K.D. Karlin. *Chem. Rev.*, **118**, 10840 (2018). [Crossref], [PubMed], [Google Scholar]
11. C.E. Elwell, N.L. Gagnon, B.D. Neisen, D. Dhar, A.D. Spaeth, G.M. Yee, W.B. Tolman. *Chem. Rev.*, **117**, 2059 (2017). [Crossref], [PubMed], [Web of Science ®], [Google Scholar]
12. H.R. Lucas, L. Li, A.A.N. Sarjeant, M.A. Vance, E.I. Solomon, K.D. Karlin. *J. Am. Chem. Soc.*, **131**, 3230 (2009). [Crossref], [PubMed], [Web of Science ®], [Google Scholar]

13. L.M. Mirica, X. Ottenwaelder, T.D.P. Stack. *Chem. Rev*, **104**, 1013 (2004). [Crossref], [PubMed], [Web of Science ®], [Google Scholar]
14. K.D. Karlin, N. Wei, B. Jung, S. Kaderli, P. Niklaus, A.D. Zuberbuehler. *J. Am. Chem. Soc.*, **115**, 9506 (1993). [Crossref], [Web of Science ®], [Google Scholar]
15. M.J. Baldwin, P.K. Ross, J.E. Pate, Z. Tyeklar, K.D. Karlin, E.I. Solomon. *J. Am. Chem. Soc.*, **113**, 8671 (1991). [Crossref], [Google Scholar]
16. K.D. Karlin, N. Wei, B. Jung, S. Kaderli, A.D. Zuberbuehler. *J. Am. Chem. Soc.*, **113**, 5868 (1991). [Crossref], [Google Scholar]
17. R.R. Jacobson, Z. Tyeklar, A. Farooq, K.D. Karlin, S. Liu, J. Zubieta. *J. Am. Chem. Soc.*, **110**, 3690 (1988). [Crossref], [Web of Science ®], [Google Scholar]
18. S.Y. Quek, S. Debnath, S. Laxmi, M. van Gastel, T. Krämer, J. England. *J. Am. Chem. Soc.*, **143**, 19731 (2021). [Crossref], [PubMed], [Google Scholar]
19. E.W. Dahl, H.T. Dong, N.K. Szymczak. *Chem. Commun. (Camb.)*, **54**, 892 (2018). [Crossref], [PubMed], [Google Scholar]
20. S. Hematian, M.A. Siegler, K.D. Karlin. *J. Am. Chem. Soc.*, **134**, 18912 (2012). [Crossref], [PubMed], [Web of Science ®], [Google Scholar]
21. G.M. Sheldrick. *SHELXL-2018: Program for Crystal Structure Refinement*, University of GöTtingen, GöTtingen, Germany (2018). [Google Scholar]
22. F.S.T. Khan, A.L. Waldbusser, M.C. Carrasco, H. Pourhadi, S. Hematian. *Dalton Trans.*, **50**, 7433 (2021). [Crossref], [PubMed], [Google Scholar]
23. R. Li, F.S. Khan, S. Hematian. *Molecules*, **27**, 1000 (2022). [Crossref], [PubMed], [Google Scholar]
24. C.X. Zhang, S. Kaderli, M. Costas, E-i Kim, Y.-M. Neuhold, K.D. Karlin, A.D. Zuberbühler. *Inorg. Chem.*, **42**, 1807 (2003). [Crossref], [PubMed], [Web of Science ®], [Google Scholar]
25. Z. Tyeklar, R.R. Jacobson, N. Wei, N.N. Murthy, J. Zubieta, K.D. Karlin. *J. Am. Chem. Soc.*, **115**, 2677 (1993). [Crossref], [Web of Science ®], [Google Scholar]
26. R.R. Jacobson, Z. Tyeklár, K.D. Karlin. *Inorg. Chim. Acta*, **181**, 111 (1991). [Crossref], [Google Scholar]
27. T. Osako, K.D. Karlin, S. Itoh. *Inorg. Chem.*, **44**, 410 (2005). [Crossref], [PubMed], [Google Scholar]
28. B. Lucchese, K.J. Humphreys, D.-H. Lee, C.D. Incarvito, R.D. Sommer, A.L. Rheingold, K.D. Karlin. *Inorg. Chem.*, **43**, 5987 (2004). [Crossref], [PubMed], [Google Scholar]
29. D. Maiti, A.A. Narducci Sarjeant, S. Itoh, K.D. Karlin. *J. Am. Chem. Soc.*, **130**, 5644 (2008). [Crossref], [PubMed], [Google Scholar]
30. B. Hathaway, G. Wilkinson, R. Gillard, J. McCleverty. Comprehensive Coordination Chemistry: *The Synthesis, Reactions, Properties and Applications of Coordination Compounds*, Pergamon Press, Oxford, Vol. **5**, pp. 533 (1987). [Google Scholar]
31. A.W. Addison, T.N. Rao, J. Reedijk, J. van Rijn, G.C. Verschoor. *J. Chem. Soc. Dalton Trans.*, 1349 (1984). DOI:10.1039/DT9840001349 [Crossref], [Google Scholar]
32. N. Wei, N.N. Murthy, Q. Chen, J. Zubieta, K.D. Karlin. *Inorg. Chem.*, **33**, 1953 (1994). [Crossref], [Web of Science ®], [Google Scholar]
33. P.K. Ross, E.I. Solomon. *J. Am. Chem. Soc.*, **113**, 3246 (1991). [Crossref], [Google Scholar]

34. E.I. Solomon. *Inorg. Chem.*, **55**, 6364 (2016). [Crossref], [PubMed], [Google Scholar]
35. A. Nanthakumar, S. Fox, N.N. Murthy, K.D. Karlin. *J. Am. Chem. Soc.*, **119**, 3898 (1997). [Crossref], [Google Scholar]
36. N.N. Murthy, K.D. Karlin, I. Bertini, C. Luchinat. *J. Am. Chem. Soc.*, **119**, 2156 (1997). [Crossref], [Web of Science ®], [Google Scholar]
37. Li, R.; Khan, F.S.T.; Tapia, M.; Hematian, S. *J. Coord. Chem.* **2022**, *75*:11-14, 1617-1635, https://doi.org/10.1080/00958972.2022.2107429.

References for "CHAPTER IV: Dioxygen Reactivity of Copper(I)/Manganese(II)-Porphyrin Assemblies"

1. Pecoraro, V.L.; Baldwin, M.J.; Gelasco, A. Interaction of Manganese with Dioxygen and Its Reduced Derivatives. *Chem. Rev.* **1994**, *94*, 807–826. [**Google Scholar**] [**CrossRef**]
2. Pecoraro, V.L.; Gelasco, A.; Baldwin, M.J. Reactivity and Mechanism of Manganese Enzymes. In *Mechanistic Bioinorganic Chemistry*; Advances in Chemistry; American Chemical Society: Washington, DC, USA, 1996; Volume 246, pp. 265–301. [**Google Scholar**]
3. Lingappa, U.F.; Monteverde, D.R.; Magyar, J.S.; Valentine, J.S.; Fischer, W.W. How Manganese Empowered Life with Dioxygen (and vice versa). *Free Radic. Biol. Med.* **2019**, *140*, 113–125. [**Google Scholar**] [**CrossRef**] [**PubMed**]
4. Emsley, J. Manganese. In *Nature's Building Bocks: An A–Z Guide to the Elements*; Oxford University Press: Oxford, UK, 2001; pp. 249–253. [**Google Scholar**]
5. Law, N.A.; Caudle, M.T.; Pecoraro, V.L. Manganese Redox Enzymes and Model Systems: Properties, Structures, and Reactivity. In *Advances in Inorganic Chemistry*; Sykes, A.G., Ed.; Academic Press: Cambridge, MA, USA, 1998; Volume 46, pp. 305–440. [**Google Scholar**]
6. Dismukes, G.C. Manganese Enzymes with Binuclear Active Sites. *Chem. Rev.* **1996**, *96*, 2909–2926. [**Google Scholar**] [**CrossRef**] [**PubMed**]
7. Zhu, W.; Richards, N.G.J. Biological Functions Controlled by Manganese Redox Changes in Mononuclear Mn-Dependent Enzymes. *Essays Biochem.* **2017**, *61*, 259–270. [**Google Scholar**] [**CrossRef**] [**PubMed**][**Green Version**]
8. Groves, J.T.; Watanabe, Y.; McMurry, T.J. Oxygen Activation by Metalloporphyrins. Formation and Decomposition of an Acylperoxymanganese(III) Complex. *J. Am. Chem. Soc.* **1983**, *105*, 4489–4490. [**Google Scholar**] [**CrossRef**]
9. Liu, W.; Groves, J.T. Manganese Porphyrins Catalyze Selective C−H Bond Halogenations. *J. Am. Chem. Soc.* **2010**, *132*, 12847–12849. [**Google Scholar**] [**CrossRef**]
10. Miriyala, S.; Spasojevic, I.; Tovmasyan, A.; Salvemini, D.; Vujaskovic, Z.; St Clair, D.; Batinic-Haberle, I. Manganese Superoxide Dismutase, MnSOD and Its Mimics. *Biochim. Biophys. Acta Mol. Basis Dis.* **2012**, *1822*, 794–814. [**Google Scholar**] [**CrossRef**][**Green Version**]
11. Guo, M.; Dong, H.; Li, J.; Cheng, B.; Huang, Y.; Feng, Y.; Lei, A. Spectroscopic Observation of Iodosylarene Metalloporphyrin Adducts and Manganese(V)-oxo Porphyrin Species in a Cytochrome P450 Analogue. *Nat. Commun.* **2012**, *3*, 1190. [**Google Scholar**] [**CrossRef**][**Green Version**]

12. Liu, W.; Groves, J.T. Manganese Catalyzed C–H Halogenation. *Acc. Chem. Res.* **2015**, *48*, 1727–1735. [**Google Scholar**] [**CrossRef**]

13. Huang, X.; Zhuang, T.; Kates, P.A.; Gao, H.; Chen, X.; Groves, J.T. Alkyl Isocyanates via Manganese-Catalyzed C–H Activation for the Preparation of Substituted Ureas. *J. Am. Chem. Soc.* **2017**, *139*, 15407–15413. [**Google Scholar**] [**CrossRef**]

14. Passard, G.; Dogutan, D.K.; Qiu, M.; Costentin, C.; Nocera, D.G. Oxygen Reduction Reaction Promoted by Manganese Porphyrins. *ACS Catal.* **2018**, *8*, 8671–8679. [**Google Scholar**] [**CrossRef**]

15. Guo, M.; Seo, M.S.; Lee, Y.-M.; Fukuzumi, S.; Nam, W. Highly Reactive Manganese(IV)-Oxo Porphyrins Showing Temperature-Dependent Reversed Electronic Effect in C–H Bond Activation Reactions. *J. Am. Chem. Soc.* **2019**, *141*, 12187–12191. [**Google Scholar**] [**CrossRef**] [**PubMed**]

16. Li, G.; Kates, P.A.; Dilger, A.K.; Cheng, P.T.; Ewing, W.R.; Groves, J.T. Manganese-Catalyzed Desaturation of N-Acyl Amines and Ethers. *ACS Catal.* **2019**, *9*, 9513–9517. [**Google Scholar**] [**CrossRef**]

17. Klaine, S.; Bratcher, F.; Winchester, C.M.; Zhang, R. Formation and Kinetic Studies of Manganese(IV)-oxo Porphyrins: Oxygen Atom Transfer Mechanism of Sulfide Oxidations. *J. Inorg. Biochem.* **2020**, *204*, 110986. [**Google Scholar**] [**CrossRef**]

18. Zhang, L.; Lee, Y.-M.; Guo, M.; Fukuzumi, S.; Nam, W. Unprecedented Reactivities of Highly Reactive Manganese(III)–Iodosylarene Porphyrins in Oxidation Reactions. *J. Am. Chem. Soc.* **2020**, *142*, 19879–19884. [**Google Scholar**] [**CrossRef**]

19. Mann, S.I.; Nayak, A.; Gassner, G.T.; Therien, M.J.; DeGrado, W.F. De Novo Design, Solution Characterization, and Crystallographic Structure of an Abiological Mn–Porphyrin-Binding Protein Capable of Stabilizing a Mn(V) Species. *J. Am. Chem. Soc.* **2021**, *143*, 252–259. [**Google Scholar**] [**CrossRef**]

20. Kostopoulos, N.; Banse, F.; Fave, C.; Anxolabéhère-Mallart, E. Modulating Alkene Reactivity from Oxygenation to Halogenation via Electrochemical O_2 Activation by Mn Porphyrin. *Chem. Commun.* **2021**, *57*, 1198–1201. [**Google Scholar**] [**CrossRef**]

21. Guo, M.; Zhang, J.; Zhang, L.; Lee, Y.-M.; Fukuzumi, S.; Nam, W. Enthalpy–Entropy Compensation Effect in Oxidation Reactions by Manganese(IV)-Oxo Porphyrins and Nonheme Iron(IV)-Oxo Models. *J. Am. Chem. Soc.* **2021**, *143*, 18559–18570. [**Google Scholar**] [**CrossRef**]

22. Weschler, C.J.; Hoffman, B.M.; Basolo, F. Synthetic Oxygen Carrier. Dioxygen Adduct of a Manganese Porphyrin. *J. Am. Chem. Soc.* **1975**, *97*, 5278–5280. [**Google Scholar**] [**CrossRef**]

23. Hoffman, B.M.; Szymanski, T.; Brown, T.G.; Basolo, F. The Dioxygen Adducts of Several Manganese(II) Porphyrins. Electron Paramagnetic Resonance Studies. *J. Am. Chem. Soc.* **1978**, *100*, 7253–7259. [**Google Scholar**] [**CrossRef**]

24. VanAtta, R.B.; Strouse, C.E.; Hanson, L.K.; Valentine, J.S. Peroxo(tetraphenylporphinato)manganese(III) and Chloro(tetraphenylporphinato)manganese(II) Anions. Synthesis, Crystal Structures, and Electronic Structures. *J. Am. Chem. Soc.* **1987**, *109*, 1425–1434. [**Google Scholar**] [**CrossRef**]

25. Phung, Q.M.; Pierloot, K. The Dioxygen Adducts of Iron and Manganese Porphyrins: Electronic Structure and Binding Energy. *Phys. Chem. Chem. Phys.* **2018**, *20*, 17009–17019. [**Google Scholar**] [**CrossRef**] [**PubMed**]

26. Valentine, J.S.; Quinn, A.E. Reaction of Superoxide with the Manganese(III) Tetraphenylporphine Cation. *Inorg. Chem.* **1976**, *15*, 1997–1999. [**Google Scholar**] [**CrossRef**]

27. Adam, S.M.; Wijeratne, G.B.; Rogler, P.J.; Diaz, D.E.; Quist, D.A.; Liu, J.J.; Karlin, K.D. Synthetic Fe/Cu Complexes: Toward Understanding Heme-Copper Oxidase Structure and Function. *Chem. Rev.* **2018**, *118*, 10840–11022. [**Google Scholar**] [**CrossRef**] [**PubMed**]

28. Karlin, K.D.; Wei, N.; Jung, B.; Kaderli, S.; Niklaus, P.; Zuberbuehler, A.D. Kinetics and Thermodynamics of Formation of Copper-Dioxygen Adducts: Oxygenation of Mononuclear Copper(I) Complexes Containing Tripodal Tetradentate Ligands. *J. Am. Chem. Soc.* **1993**, *115*, 9506–9514. [**Google Scholar**] [**CrossRef**]

29. Karlin, K.D.; Kaderli, S.; Zuberbühler, A.D. Kinetics and Thermodynamics of Copper(I)/Dioxygen Interaction. *Acc. Chem. Res.* **1997**, *30*, 139–147. [**Google Scholar**] [**CrossRef**]

30. Zhang, C.X.; Kaderli, S.; Costas, M.; Kim, E.; Neuhold, Y.-M.; Karlin, K.D.; Zuberbühler, A.D. Copper(I)−Dioxygen Reactivity of $[(L)Cu^{I}]^{+}$ (L = Tris(2-pyridylmethyl)amine): Kinetic/Thermodynamic and Spectroscopic Studies Concerning the Formation of $Cu-O_2$ and Cu_2-O_2 Adducts as a Function of Solvent Medium and 4-Pyridyl Ligand Substituent Variations. *Inorg. Chem.* **2003**, *42*, 1807–1824. [**Google Scholar**] [**CrossRef**]

31. Solomon, E.I.; Heppner, D.E.; Johnston, E.M.; Ginsbach, J.W.; Cirera, J.; Qayyum, M.; Kieber-Emmons, M.T.; Kjaergaard, C.H.; Hadt, R.G.; Tian, L. Copper Active Sites in Biology. *Chem. Rev.* **2014**, *114*, 3659–3853. [**Google Scholar**] [**CrossRef**][**Green Version**]

32. Williamson, M.M.; Hill, C.L. Isolation and Characterization of a Five-Coordinate Manganese(III) Porphyrin Cation. Crystal and Molecular Structure of Aquo(tetraphenylporphinato)manganese(III) Triflate. *Inorg. Chem.* **1986**, *25*, 4668–4671. [**Google Scholar**] [**CrossRef**]

33. Galinato, M.G.I.; Brocious, E.P.; Paulat, F.; Martin, S.; Skodack, J.; Harland, J.B.; Lehnert, N. Elucidating the Electronic Structure of High-Spin [MnIII(TPP)Cl] Using Magnetic Circular Dichroism Spectroscopy. *Inorg. Chem.* **2020**, *59*, 2144–2162. [**Google Scholar**] [**CrossRef**]

34. Carrasco, M.C.; Hematian, S. (Hydr)oxo-Bridged Heme Complexes: From Structure to Reactivity. *J. Porphyr. Phthalocyanines* **2019**, *23*, 1286–1307. [**Google Scholar**] [**CrossRef**][**Green Version**]

35. Citek, C.; Herres-Pawlis, S.; Stack, T.D.P. Low Temperature Syntheses and Reactivity of Cu_2O_2 Active-Site Models. *Acc. Chem. Res.* **2015**, *48*, 2424–2433. [**Google Scholar**] [**CrossRef**] [**PubMed**]

36. Groves, J.T.; Stern, M.K. Synthesis, Characterization, and Reactivity of Oxomanganese(IV) Porphyrin Complexes. *J. Am. Chem. Soc.* **1988**, *110*, 8628–8638. [**Google Scholar**] [**CrossRef**]

37. Groves, J.T.; Lee, J.; Marla, S.S. Detection and Characterization of an Oxomanganese(V) Porphyrin Complex by Rapid-Mixing Stopped-Flow Spectrophotometry. *J. Am. Chem. Soc.* **1997**, *119*, 6269–6273. [**Google Scholar**] [**CrossRef**]

38. Low, D.W.; Abedin, S.; Yang, G.; Winkler, J.R.; Gray, H.B. Manganese Microperoxidase-8. *Inorg. Chem.* **1998**, *37*, 1841–1843. [**Google Scholar**] [**CrossRef**][**Green Version**]

39. Camenzind, M.J.; Hollander, F.J.; Hill, C.L. Syntheses, Ground Electronic State, and Crystal and Molecular Structure of the Monomeric Manganese(IV) Porphyrin Complex Dimethoxy(5,10,15,20-tetraphenylporphinato)manganese(IV). *Inorg. Chem.* **1982**, *21*, 4301–4308. [**Google Scholar**] [**CrossRef**]

40. Smegal, J.A.; Schardt, B.C.; Hill, C.L. Isolation, Purification, and Characterization of Intermediate (Iodosylbenzene)metalloporphyrin Complexes from the (Tetraphenylporphinato)manganese(III)-iodosylbenzene Catalytic Hydrocarbon Functionalization System. *J. Am. Chem. Soc.* **1983**, *105*, 3510–3515. [**Google Scholar**] [**CrossRef**]

41. Kaustov, L.; Tal, M.E.; Shames, A.I.; Gross, Z. Spin Transition in a Manganese(III) Porphyrin Cation Radical, Its Transformation to a Dichloromanganese(IV) Porphyrin, and Chlorination of Hydrocarbons by the Latter. *Inorg. Chem.* **1997**, *36*, 3503–3511. [**Google Scholar**] [**CrossRef**]

42. Hatano, K.; Anzai, K.; Iitaka, Y. The Crystal and Molecular Structure of Bis(methanol)-α,β,γ,δ-tetraphenylporphinatomanganese(III) Perchlorate-Methanol. A Molecular Structure Relevant to the Intermediate-spin Six Coordinate Iron(III) Porphyrin. *Bull. Chem. Soc. Jpn.* **1983**, *56*, 422–427. [**Google Scholar**] [**CrossRef**][**Green Version**]

43. Hill, C.L.; Williamson, M.M. Structural and Electronic Properties of Six-Coordinate Manganese(III) Porphyrin Cations. Crystal and Molecular Structure of Bis(N,N-dimethylformamide)(Tetraphenylporphinato)manganese(III) Perchlorate, $[Mn^{III}\,TPP(DMF)_2]^+ClO_4$. *Inorg. Chem.* **1985**, *24*, 2836–2841. [**Google Scholar**] [**CrossRef**]

44. Hill, C.L.; Williamson, M.W. Electronic and Structural Properties of a Reactive Metalloporphyrin with N-oxide Axial Ligands. Crystal and Molecular Structure of Bis(2,6-lutidine N-oxide)(Tetraphenylporphinato)manganese(III) Perchlorate. *Inorg. Chem.* **1985**, *24*, 3024–3030. [**Google Scholar**] [**CrossRef**]

45. Scheidt, W.R.; Pearson, W.B.; Gosal, N. Structure of Bis(methanol)(*meso*-tetraphenylporphinato)manganese(III) Hexachloroantimonate Bis(tetrachloroethane) Solvate. *Acta Cryst. C* **1988**, *44*, 927–929. [**Google Scholar**] [**CrossRef**] [**PubMed**]

46. Bhyrappa, P.; Wilson, S.R.; Suslick, K.S. Hydrogen-Bonded Porphyrinic Solids: Supramolecular Networks of Octahydroxy Porphyrins. *J. Am. Chem. Soc.* **1997**, *119*, 8492–8502. [**Google Scholar**] [**CrossRef**]

47. Tong, S.-l.; Zhang, J.; Yan, Y.; Hu, S.; Yu, J.; Yu, L. Self-Assembled Supramolecular Architecture with Alternating Porphyrin and Phthalocyanine, Bonded by Hydrogen Bonding and *π–π* Stacking. *Solid State Sci.* **2011**, *13*, 1967–1971. [**Google Scholar**] [**CrossRef**]

48. Williamson, M.N.; Hill, C.L. Molecular Stereochemistry of Aquamanganese(III) Porphyrins. Demonstrable effect of π-Arene-Porphyrin Interaction in the metal Coordination Environment in a Metalloporphyrin. *Inorg. Chem.* **1987**, *26*, 4155–4160. [**Google Scholar**] [**CrossRef**]

49. Salomon, R.G.; Ghosh, S.; Raychaudhuri, S. Homogeneous Metal-Catalyzed Photochemistry in Organic Synthesis. In *Photosensitive Metal—Organic Systems*;

Advances in Chemistry; American Chemical Society: Washington, DC, USA, 1993; Volume 238, pp. 315–333. [**Google Scholar**]
50. Fox, S.J.; Chen, L.; Khan, M.A.; Richter-Addo, G.B. Nitrosoarene Complexes of Manganese Porphyrins. *Inorg. Chem.* **1997**, *36*, 6465–6467. [**Google Scholar**] [**CrossRef**]
51. Shirazi, A.; Goff, H.M. Characterization of Superoxide-Metalloporphyrin Reaction Products: Effective Use of Deuterium NMR Spectroscopy. *J. Am. Chem. Soc.* **1982**, *104*, 6318–6322. [**Google Scholar**] [**CrossRef**]
52. Carrasco, M.C.; Dezarn, K.J.; Khan, F.S.T.; Hematian, S. Protonation of the Oxo-Bridged Heme/Copper Assemblies: Modeling the Oxidized State of the Cytochrome *c* Oxidase Active Site. *J. Inorg. Biochem.* **2021**, *225*, 111593. [**Google Scholar**] [**CrossRef**]
53. Chufán, E.E.; Verani, C.N.; Puiu, S.C.; Rentschler, E.; Schatzschneider, U.; Incarvito, C.; Rheingold, A.L.; Karlin, K.D. Generation and Characterization of $[(P)M^{-}(X)^{-}Co(TMPA)]^{n+}$ Assemblies; P = Porphyrinate, M = Fe^{III} and Co^{III}, X = O^{2-}, OH^{-}, O_2^{2-}, and TMPA = Tris(2-pyridylmethyl)amine. *Inorg. Chem.* **2007**, *46*, 3017–3026. [**Google Scholar**] [**CrossRef**]
54. Wasser, I.M.; Martens, C.F.; Verani, C.N.; Rentschler, E.; Huang, H.-w.; Moënne-Loccoz, P.; Zakharov, L.N.; Rheingold, A.L.; Karlin, K.D. Synthesis and Spectroscopy of μ-Oxo (O^{2-})-Bridged Heme/Non-heme Diiron Complexes: Models for the Active Site of Nitric Oxide Reductase. *Inorg. Chem.* **2004**, *43*, 651–662. [**Google Scholar**] [**CrossRef**]
55. Tyeklar, Z.; Jacobson, R.R.; Wei, N.; Murthy, N.N.; Zubieta, J.; Karlin, K.D. Reversible Reaction of Dioxygen (and Carbon Monoxide) with a Copper(I) Complex. X-ray Structures of Relevant Mononuclear Cu(I) Precursor Adducts and the Trans-(μ-1,2-peroxo)dicopper(II) Product. *J. Am. Chem. Soc.* **1993**, *115*, 2677–2689. [**Google Scholar**] [**CrossRef**]
56. Kincaid, J.; Nakamoto, K. Vibrational Spectra of Transition Metal Complexes of Tetraphenylporphine. *J. Inorg. Nucl. Chem.* **1975**, *37*, 85–89. [**Google Scholar**] [**CrossRef**]
57. Hematian, S.; Siegler, M.A.; Karlin, K.D. Heme/Copper Assembly Mediated Nitrite and Nitric Oxide Interconversion. *J. Am. Chem. Soc.* **2012**, *134*, 18912–18915. [**Google Scholar**] [**CrossRef**] [**PubMed**][**Green Version**]
58. Adler, A.D.; Longo, F.R.; Kampas, F.; Kim, J. On the Preparation of Metalloporphyrins. *J. Inorg. Nucl. Chem.* **1970**, *32*, 2443–2445. [**Google Scholar**] [**CrossRef**]
59. Ghiladi, R.A.; Kretzer, R.M.; Guzei, I.; Rheingold, A.L.; Neuhold, Y.-M.; Hatwell, K.R.; Zuberbühler, A.D.; Karlin, K.D. $(F_8TPP)Fe^{II}/O_2$ Reactivity Studies {F_8TPP = Tetrakis(2,6-difluorophenyl)porphyrinate(2−)}: Spectroscopic (UV−Visible and NMR) and Kinetic Study of Solvent-Dependent (Fe/O_2 = 1:1 or 2:1) Reversible O_2-Reduction and Ferryl Formation. *Inorg. Chem.* **2001**, *40*, 5754–5767. [**Google Scholar**] [**CrossRef**]
60. Hematian, S.; Siegler, M.A.; Karlin, K.D. Nitric Oxide Generation from Heme/Copper Assembly Mediated Nitrite Reductase Activity. *J. Biol. Inorg. Chem.* **2014**, *19*, 515–528. [**Google Scholar**] [**CrossRef**] [**PubMed**]
61. Sheldrick, G.M. *SHELXL-2018: Program for Crystal Structure Refinement*; University of Göttingen: Göttingen, Germany, 2018. [**Google Scholar**]
62. Li, R.; Khan, F.S.T.; Hematian, S. *Molecules.* **2022**, *27*, 1000. https://doi.org/10.3390/molecules27031000.

APPENDIX A: SUPPORTING INFORMATION FOR "CHAPTER III: DIOXYGEN REACTIVITY OF COPPER(I) COMPLEXES"

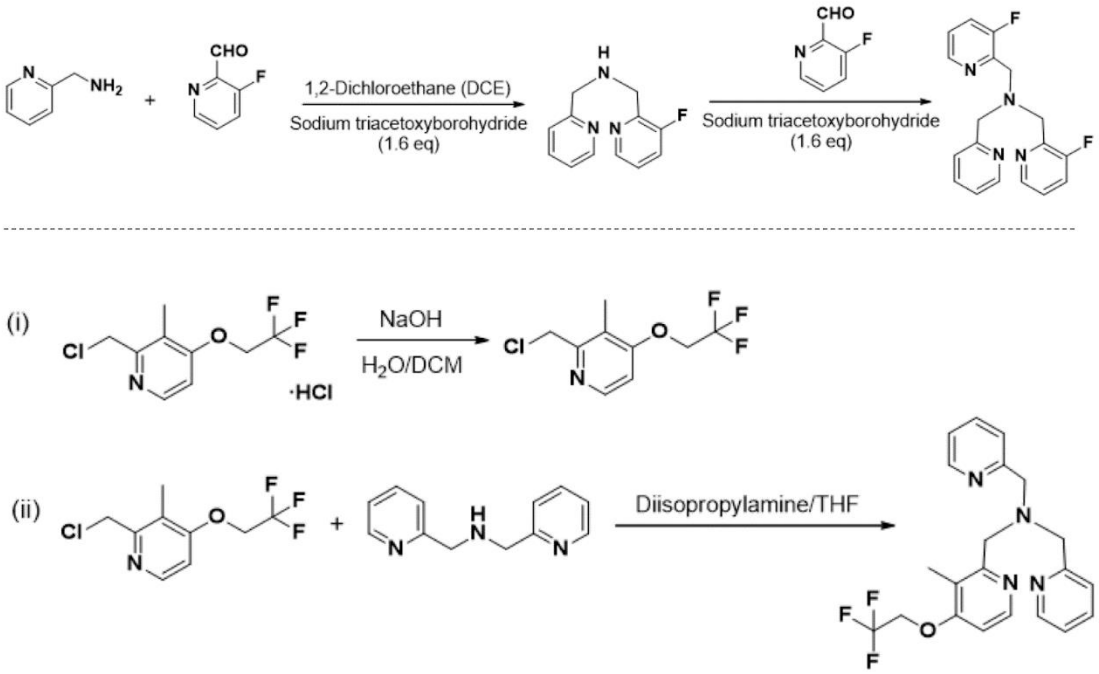

Scheme A1. Synthetic steps for the preparation of (*top*) F_2TMPA and (*bottom*) MeTFE-TMPA.

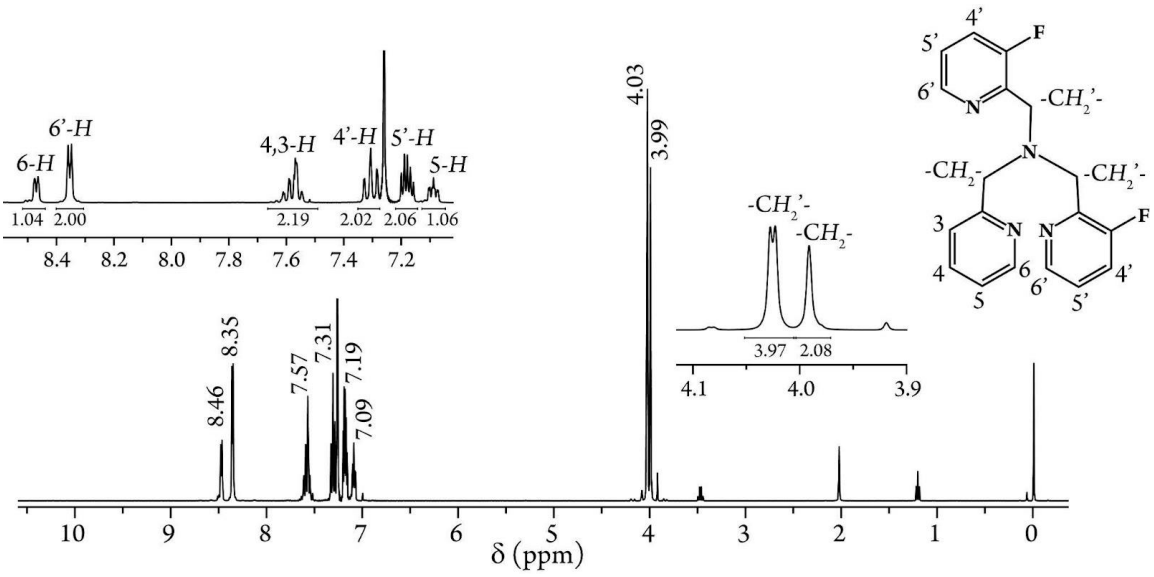

Figure A1. ^{1}H-NMR spectrum of F_2TMPA in $CDCl_3$ (400 MHz) at room temperature.

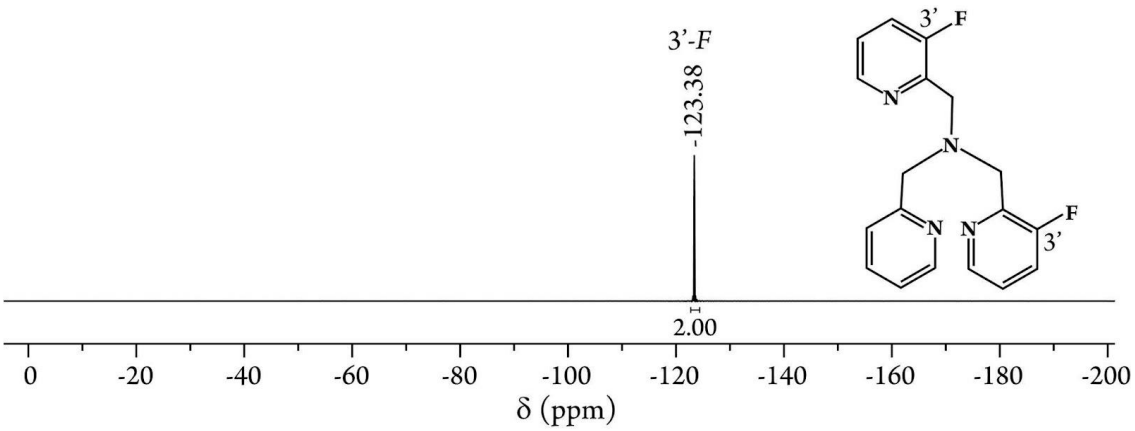

Figure A2. ^{19}F-NMR spectrum of F_2TMPA in $CDCl_3$ (376 MHz) at room temperature.

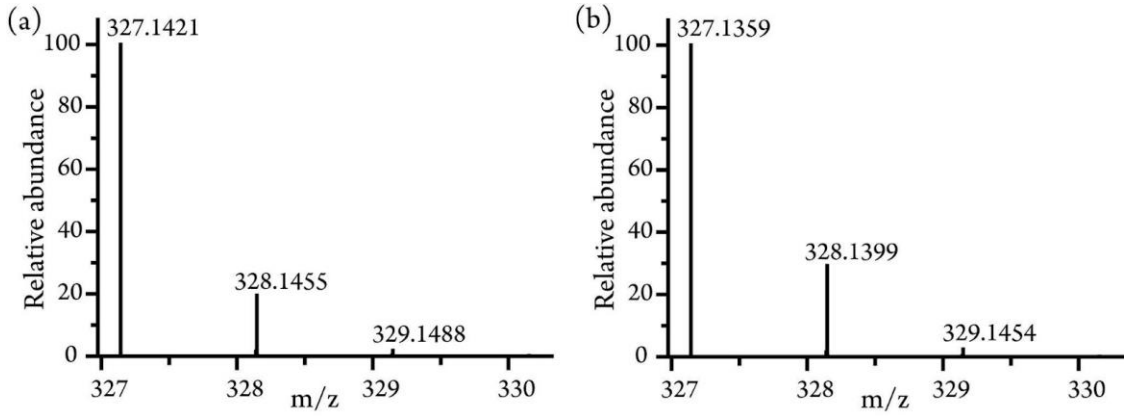

Figure A3. Isotopic distribution pattern of the (a) calculated and (b) experimental mass spectra of $[F_2TMPA+H]^+$. The sample was prepared in MeCN and recorded in positive-ion mode.

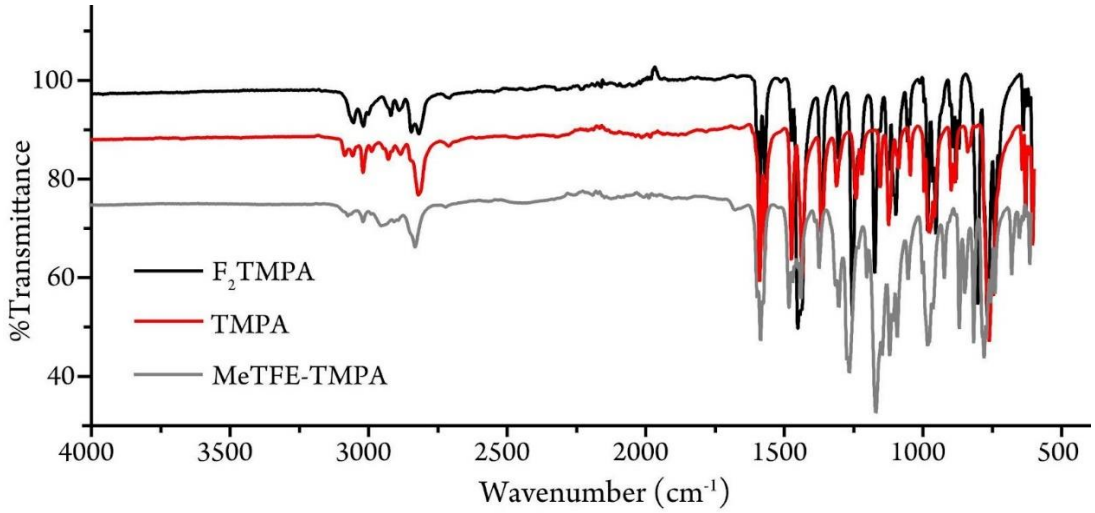

Figure A4. IR spectra (solid-state) of F_2TMPA, TMPA, and MeTFE-TMPA.

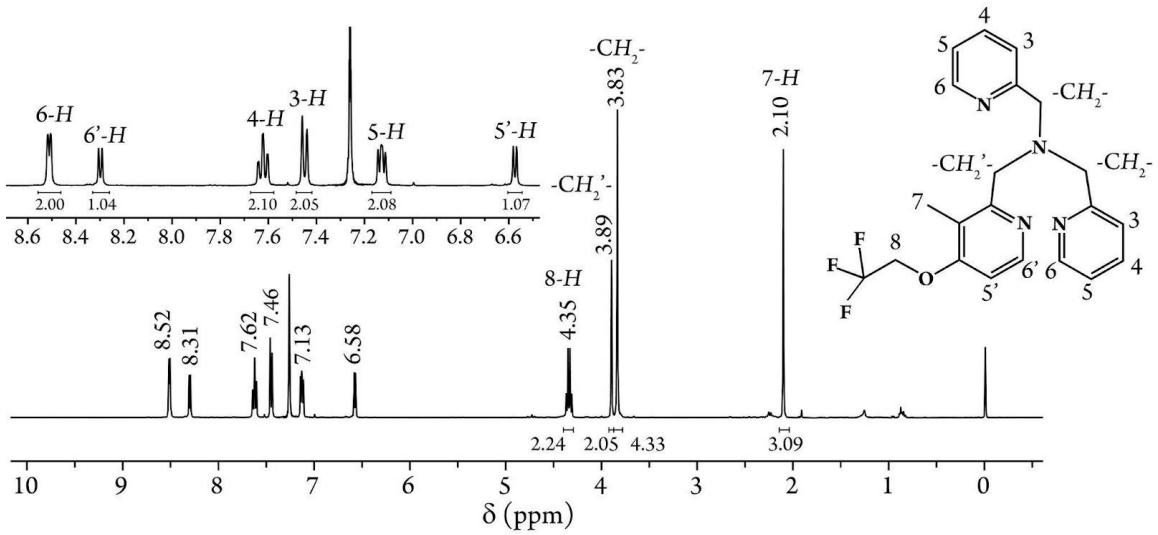

Figure A5. ^{1}H-NMR spectrum of MeTFE-TMPA in $CDCl_3$ (400 MHz) at room temperature.

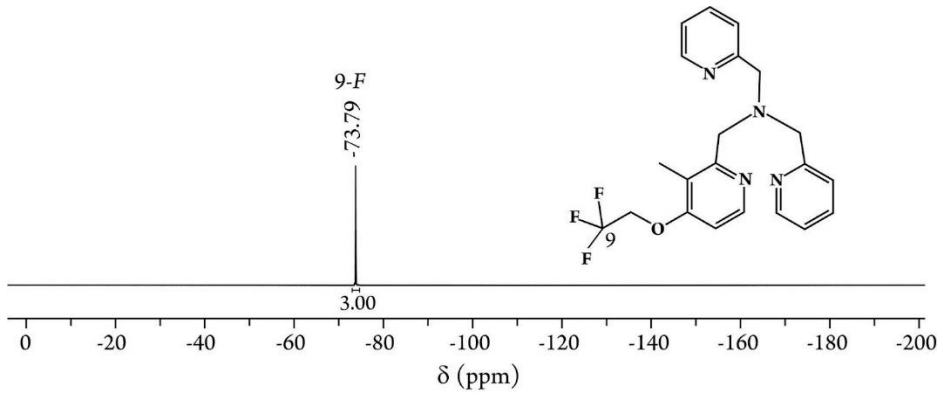

Figure A6. ^{19}F-NMR spectrum of MeTFE-TMPA in $CDCl_3$ (376 MHz) at room temperature.

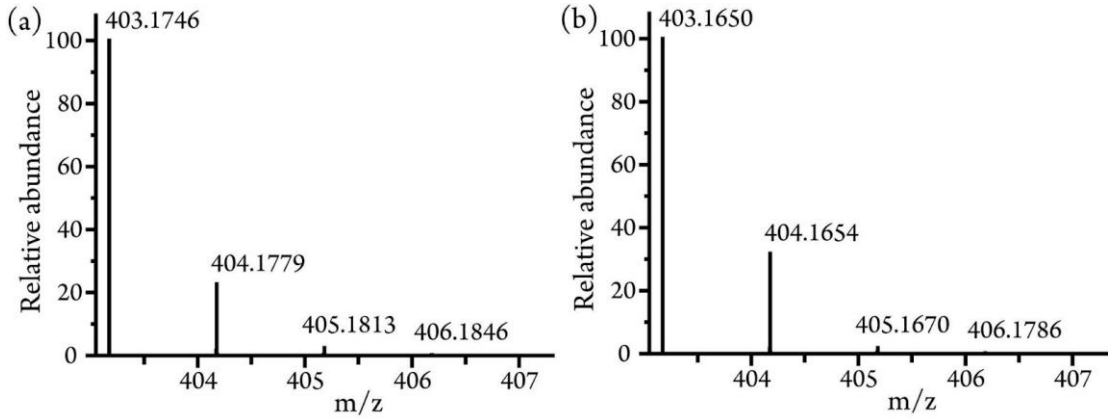

Figure A7. Isotopic distribution pattern of the (a) calculated and (b) experimental mass spectra of $[MeTFE\text{-}TMPA+H]^{+}$. The sample was prepared in MeCN and recorded in positive-ion mode.

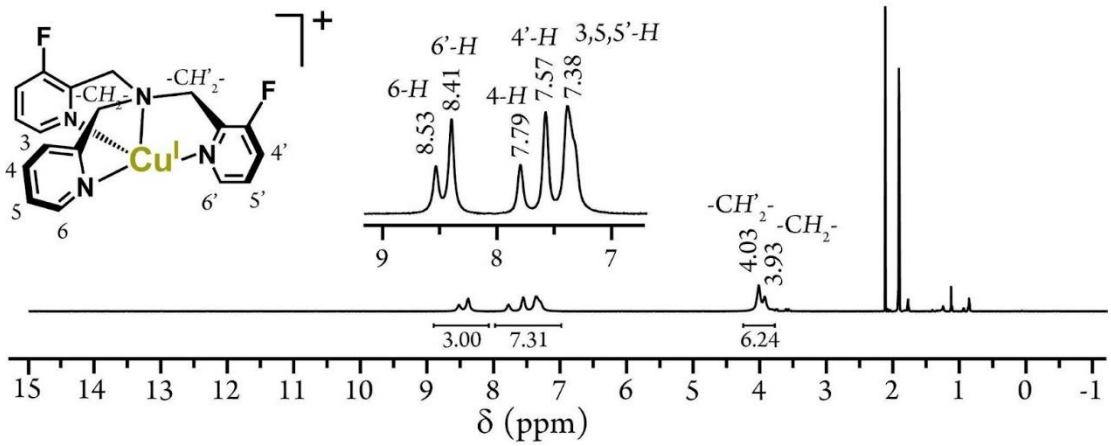

Figure A8. ^{1}H-NMR spectrum of $[(F_2tmpa)Cu^{I}][B(C_6F_5)_4]$ in CD_3CN (500 MHz) at room temperature.

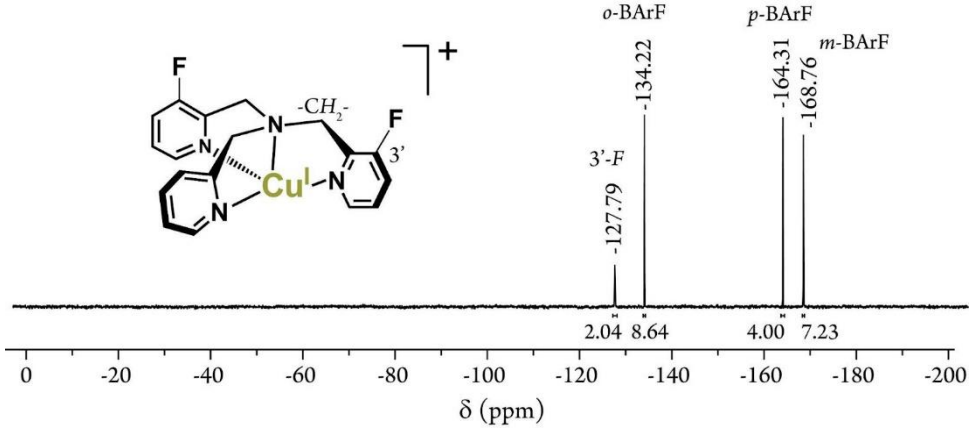

Figure A9. ^{19}F-NMR spectrum of $[(F_2tmpa)Cu^{I}][B(C_6F_5)_4]$ in CD_3CN (470 MHz) at room temperature. Peaks labeled as *o*-BArF, *p*-BArF, and *m*-BArF are for the *ortho*-, *para*-, and *meta*-fluorine atoms of the $[B(C_6F_5)_4]^-$ anion, respectively.

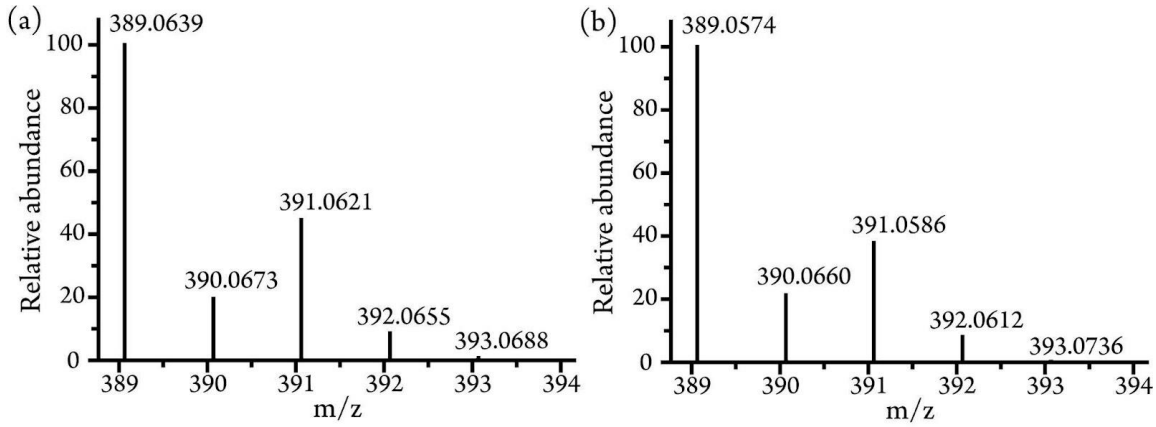

Figure A10. Isotopic distribution pattern of the (a) calculated and (b) experimental mass spectra of $[(F_2tmpa)Cu^I]^+$. The sample was prepared in MeCN and recorded in positive-ion mode.

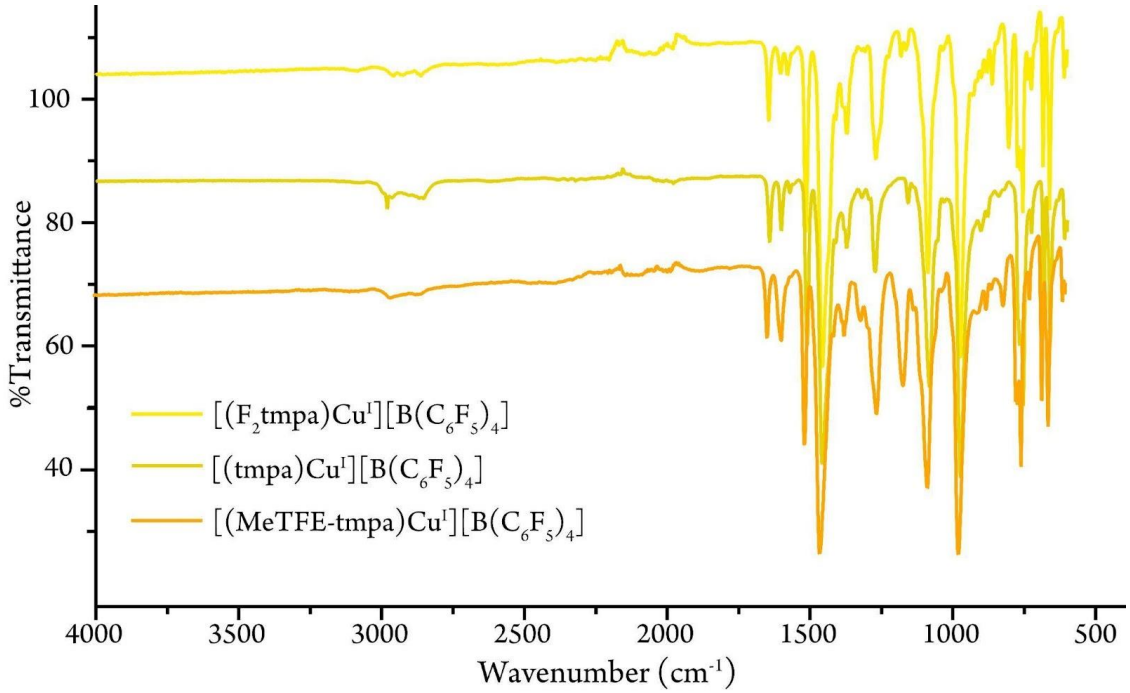

Figure A11. IR spectra (solid-state) of $[(F_2tmpa)Cu^I][B(C_6F_5)_4]$, $[(tmpa)Cu^I][B(C_6F_5)_4]$, and $[(MeTFE\text{-}tmpa)Cu^I][B(C_6F_5)_4]$.

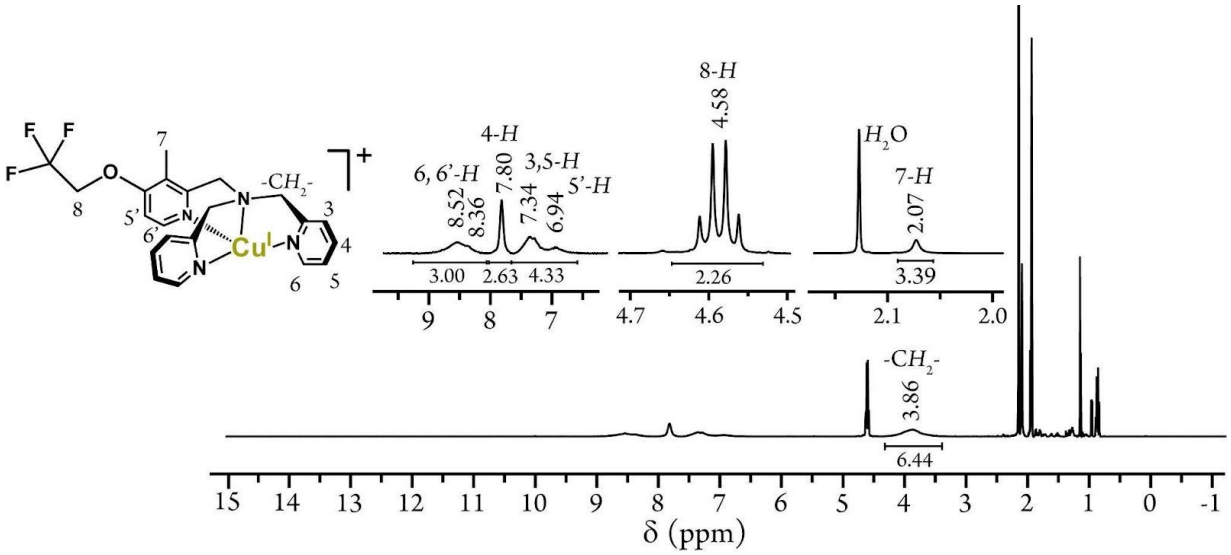

Figure A12. ^{1}H-NMR spectrum of [(MeTFE-tmpa)Cu^{I}][B(C_6F_5)$_4$] in CD_3CN (500 MHz) at room temperature.

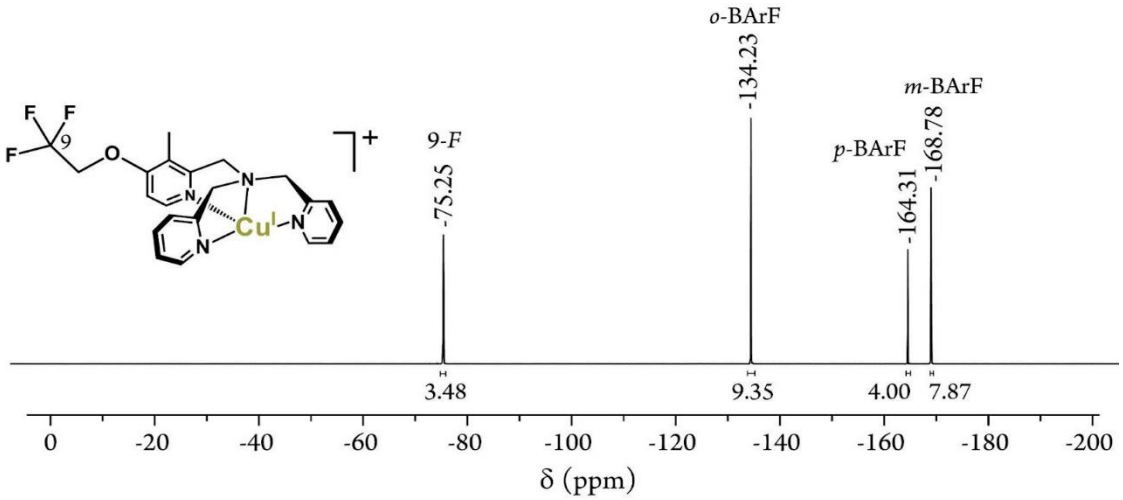

Figure A13. ^{19}F-NMR spectrum of [(MeTFE-tmpa)Cu^{I}][B(C_6F_5)$_4$] in CD_3CN (470 MHz) at room temperature. Peaks labeled as *o*-BArF, *p*-BArF, and *m*-BArF are for the *ortho*-, *para*-, and *meta*-fluorine atoms of the $[B(C_6F_5)_4]^-$ anion, respectively.

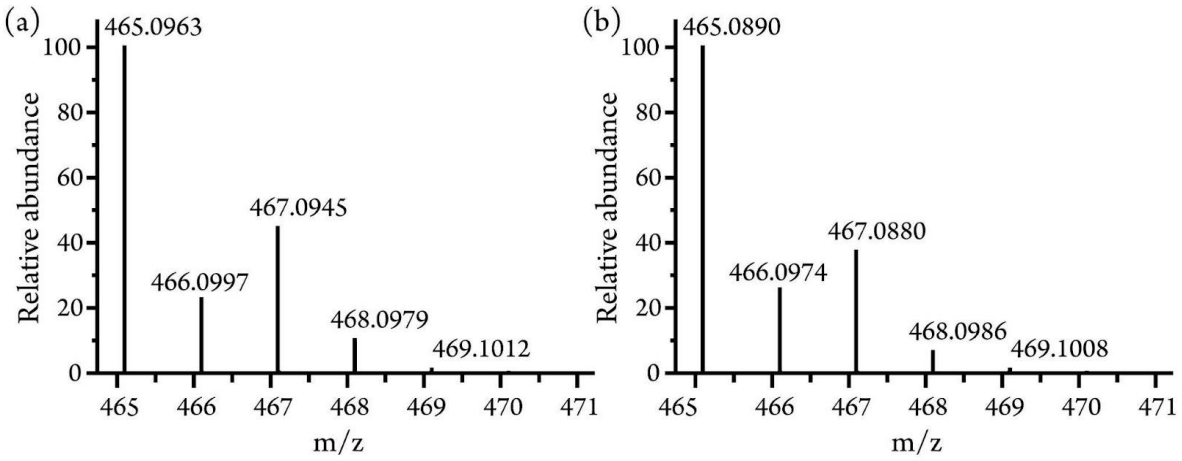

Figure A14. Isotopic distribution pattern of the (a) calculated and (b) experimental mass spectra of $[(\text{MeTFE-tmpa})\text{Cu}^{\text{I}}]^{+}$. The sample was prepared in MeCN and recorded in positive-ion mode.

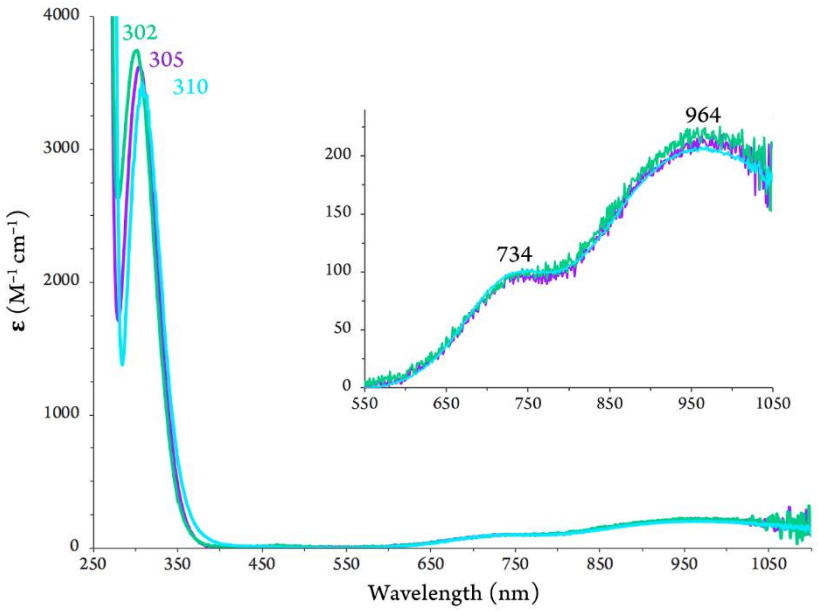

Figure A15. Quantitative electronic spectra of $[(F_2\text{tmpa})\text{Cu}^{\text{II}}(\text{Cl})][B(C_6F_5)_4]$ (turquoise), $[(\text{tmpa})\text{Cu}^{\text{II}}(\text{Cl})][B(C_6F_5)_4]$ (purple), and $[(\text{MeTFE-tmpa})\text{Cu}^{\text{II}}(\text{Cl})][B(C_6F_5)_4]$ (green) in MeTHF at room temperature.

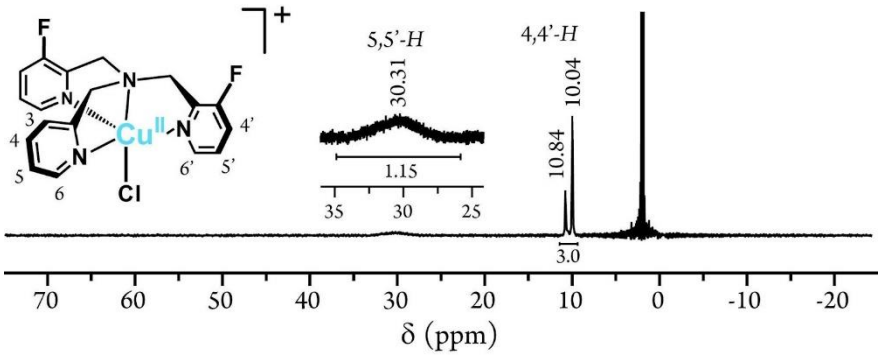

Figure A16. ^{1}H-NMR spectrum of [(F_2tmpa)Cu^{II}(Cl)][$B(C_6F_5)_4$] in CD_3CN (500 MHz) at room temperature.

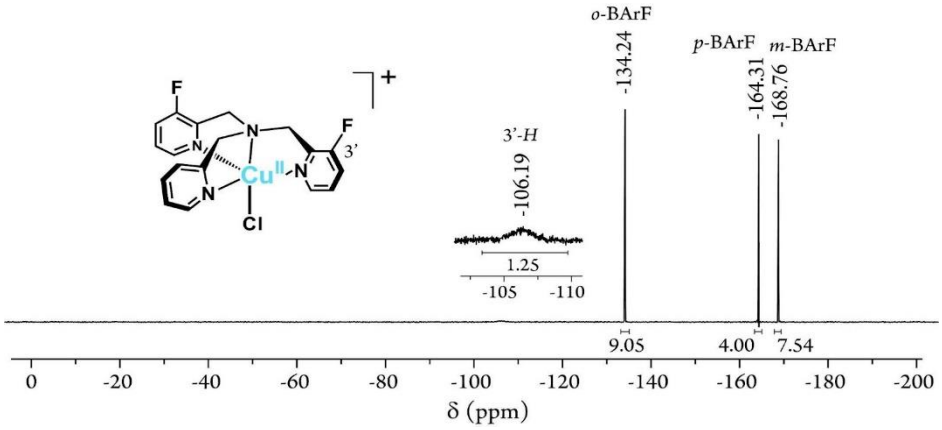

Figure A17. ^{19}F-NMR spectrum of [(F_2tmpa)Cu^{II}(Cl)][$B(C_6F_5)_4$] in CD_3CN (470 MHz) at room temperature.

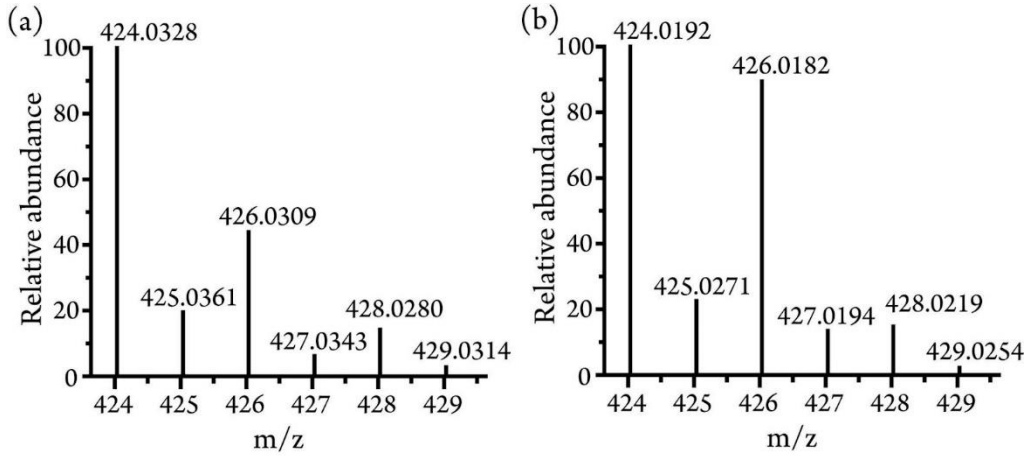

Figure A18. Isotopic distribution pattern of the (a) calculated and (b) experimental mass spectra of [(F_2tmpa)Cu^{II}(Cl)]$^{+}$. The sample was prepared in MeCN and recorded in positive-ion mode.

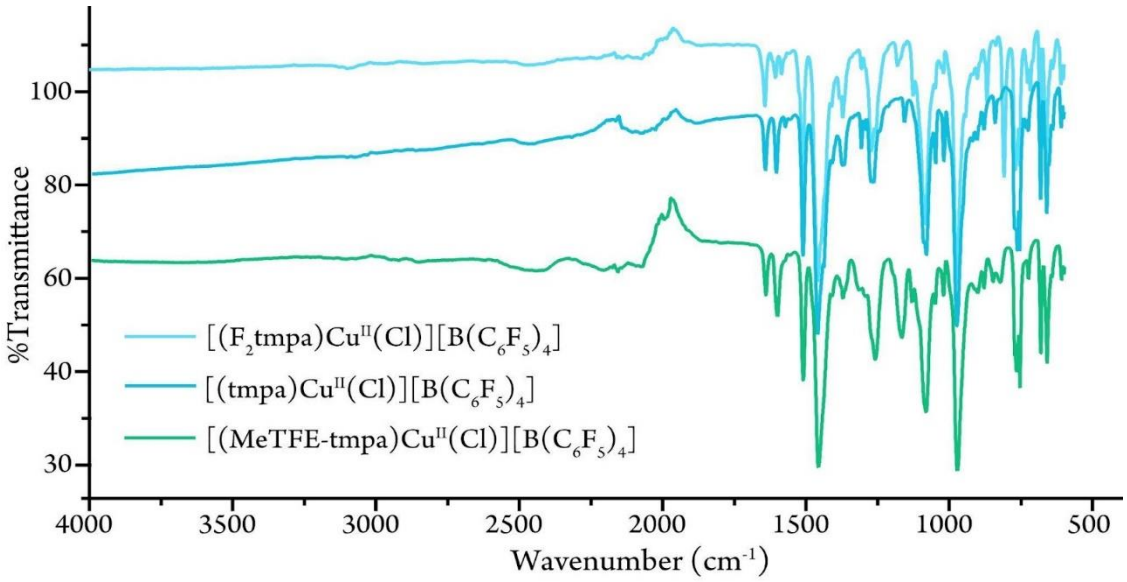

Figure A19. IR spectrum of $[(F_2tmpa)Cu^{II}(Cl)][B(C_6F_5)_4]$, and $[(tmpa)Cu^{II}(Cl)][B(C_6F_5)_4]$, and $[(MeTFE\text{-}tmpa)Cu^{II}(Cl)][B(C_6F_5)_4]$.

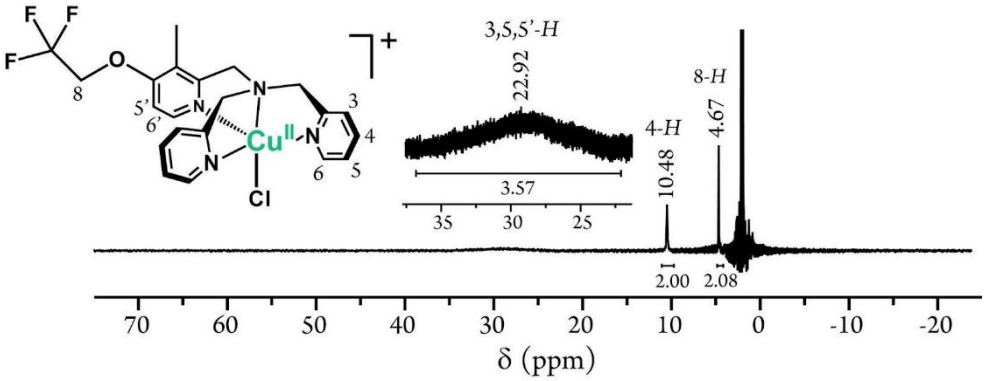

Figure A20. ^{1}H-NMR spectrum of $[(MeTFE\text{-}tmpa)Cu^{II}(Cl)][B(C_6F_5)_4]$ in CD_3CN (500 MHz) at room temperature.

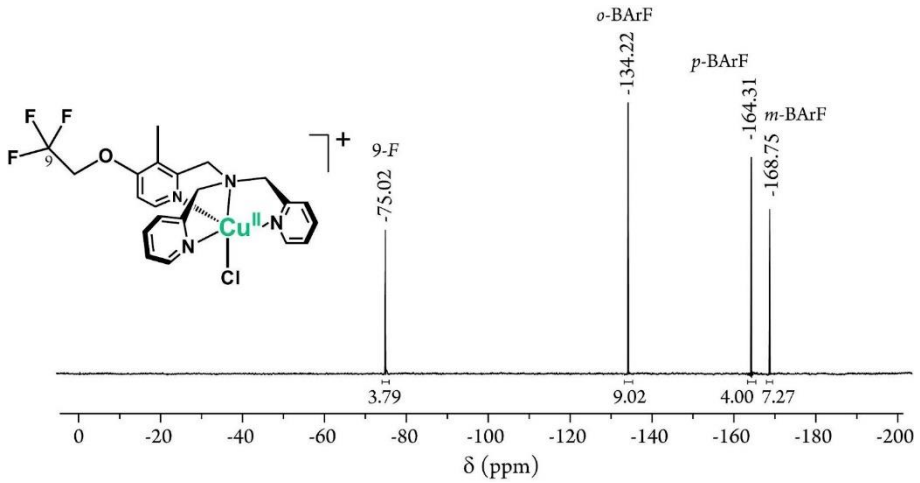

Figure A21. ^{19}F-NMR spectrum of [(MeTFE-tmpa)Cu^{II}(Cl)][B(C_6F_5)$_4$] in CD_3CN (470 MHz) at room temperature.

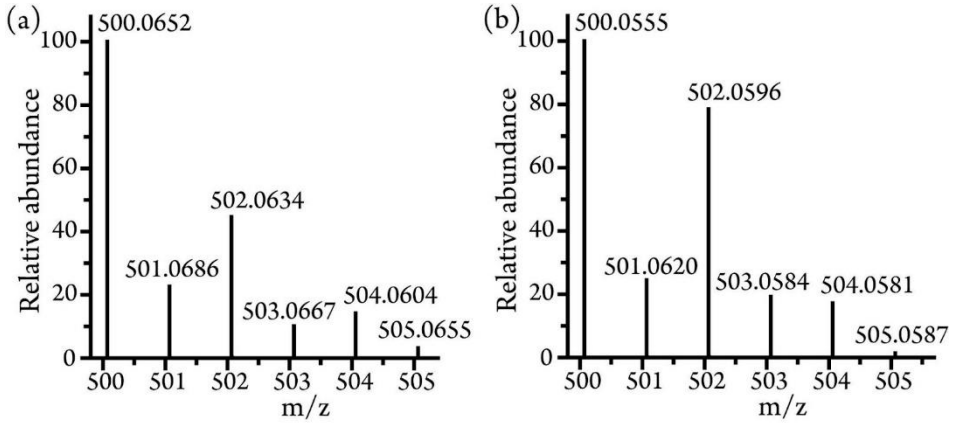

Figure A22. Isotopic distribution pattern of the (a) calculated and (b) experimental mass spectra of [(MeTFE-tmpa)Cu^{II}(Cl)]$^+$. The sample was prepared in MeCN and recorded in positive-ion mode.

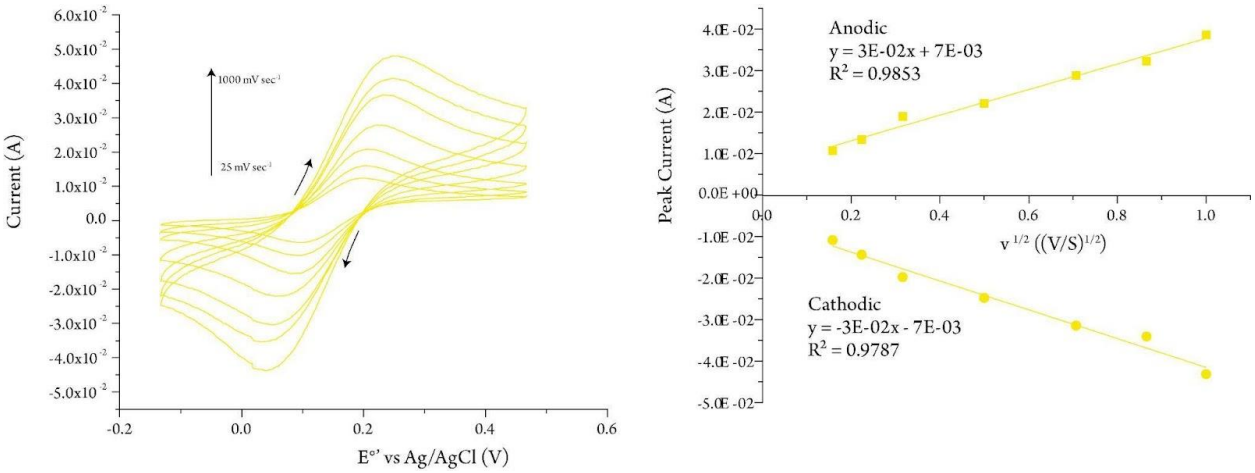

Figure A23. (*Left*) Cyclic voltammograms of 2 mM [(F_2tmpa)Cu^I][($B(C_6F_5)_4$)] in MeCN with 100 mM [(nBu)$_4$N][PF_6] as the supporting electrolyte at different scan rates. (*Right*) Randles-Sevcik plot of the CV data.

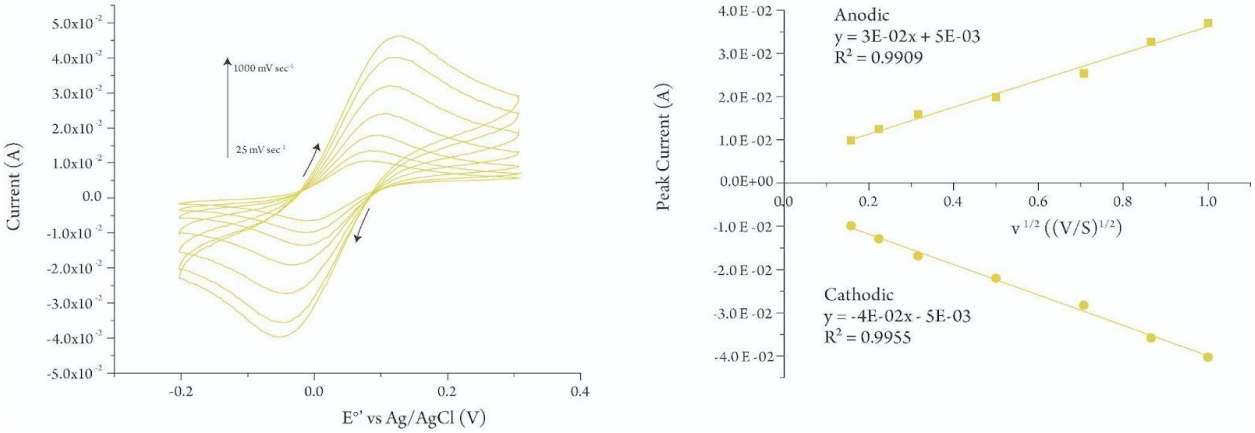

Figure A24. (*Left*) Cyclic voltammograms of 2 mM [(tmpa)Cu^I][($B(C_6F_5)_4$)] in MeCN with 100 mM [(nBu)$_4$N][PF_6] as the supporting electrolyte at different scan rates. (*Right*) Randles-Sevcik plot of the CV data.

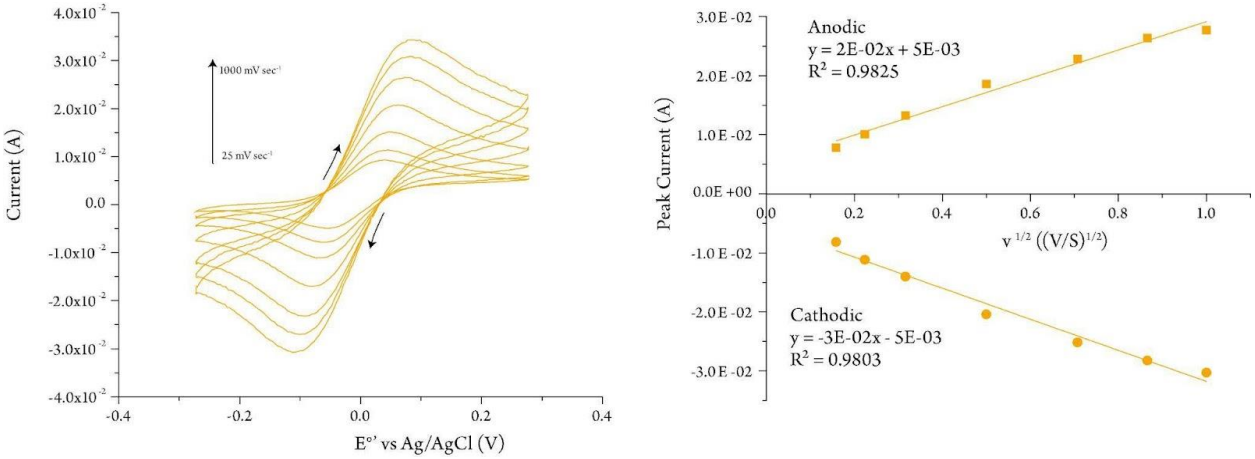

Figure A25. (*Left*) Cyclic voltammograms of 2 mM [(MeTFE-tmpa)Cu^I][($B(C_6F_5)_4$)] in MeCN with 100 mM [(nBu)$_4$N][PF_6] as the supporting electrolyte at different scan rates. (*Right*) Randles-Sevcik plot of the CV data.

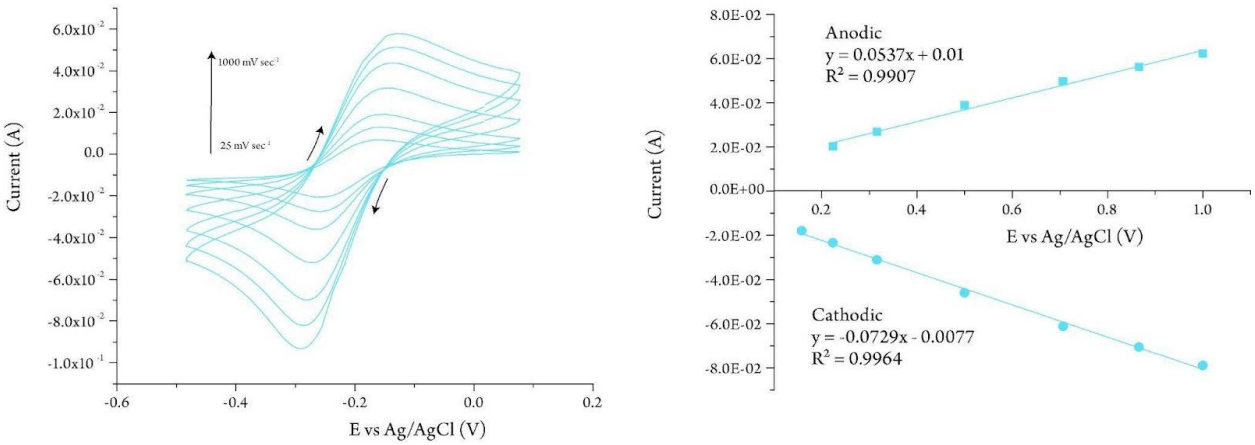

Figure A26. (*Left*) Cyclic voltammograms of 2 mM [(F_2tmpa)Cu^{II}(Cl)][($B(C_6F_5)_4$)] in MeCN with 100 mM [(nBu)$_4$N][PF_6] as the supporting electrolyte at different scan rates. (*Right*) Randles-Sevcik plot of the CV data.

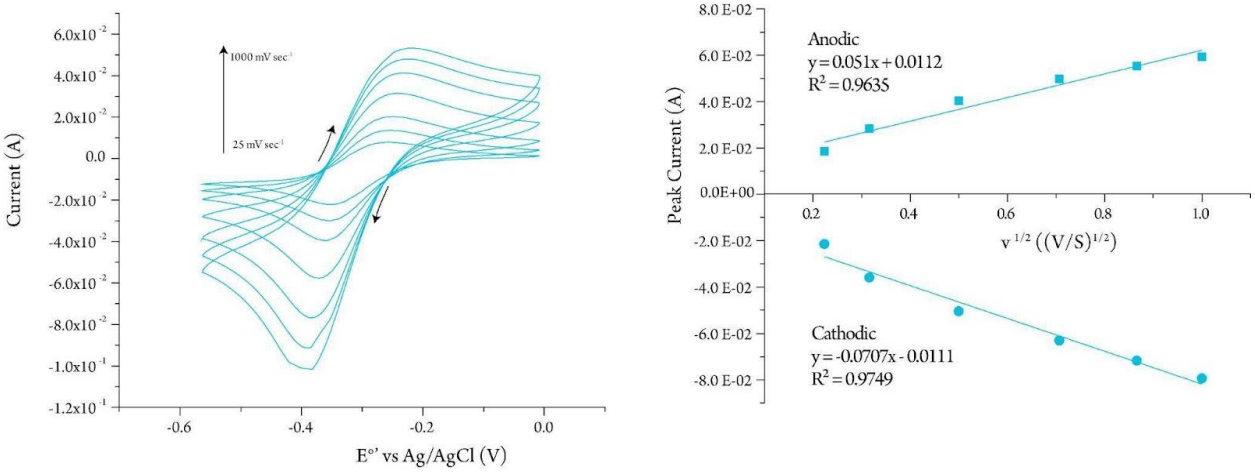

Figure A27. (*Left*) Cyclic voltammograms of 2 mM [(tmpa)Cu^{II}(Cl)][($B(C_6F_5)_4$)] in MeCN with 100 mM [(nBu)$_4$N][PF_6] as the supporting electrolyte at different scan rates. (*Right*) Randles-Sevcik plot of the CV data.

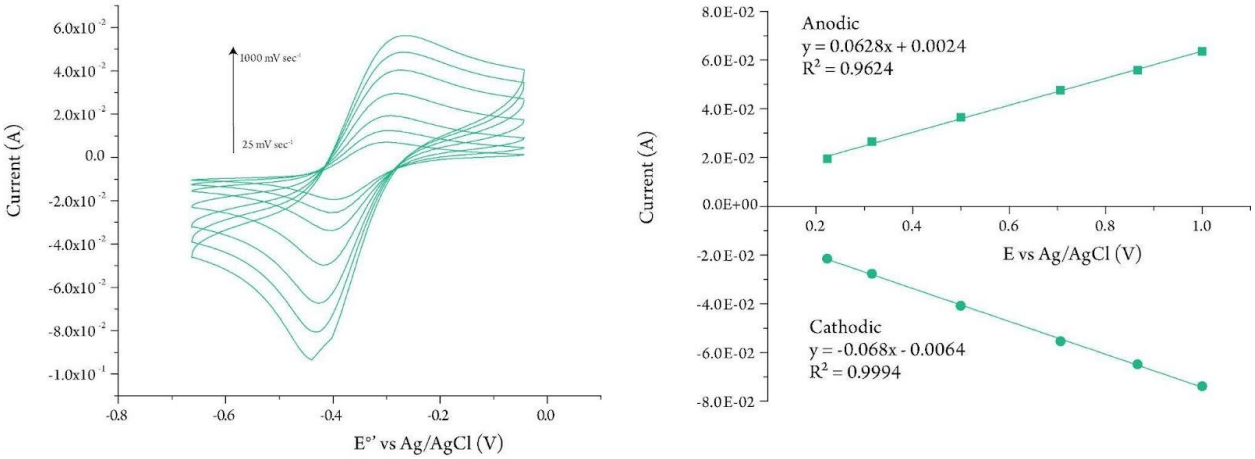

Figure A28. (*Left*) Cyclic voltammograms of 2 mM [(MeTFE-tmpa)Cu^{II}(Cl)][($B(C_6F_5)_4$)] in MeCN with 100 mM [(nBu)$_4$N][PF_6] as the supporting electrolyte at different scan rates. (*Right*) Randles-Sevcik plot of the CV data.

Table A1. Diffusion coefficient values of various copper complexes in MeCN with 100 mM of [(*n*Bu)$_4$N][PF$_6$].

Complex	*10^4 × D [(cm^2 s^{-1})] in MeCN Anodic*	*10^4 × D [(cm^2 s^{-1})] in MeCN Cathodic*
[(F_2tmpa)Cu^I][$B(C_6F_5)_4$]	2.28	2.89
[(tmpa)Cu^I][$B(C_6F_5)_4$]	2.32	2.96
[(MeTFE-tmpa)Cu^I][$B(C_6F_5)_4$]	1.38	1.65
[(F_2tmpa)Cu^{II}(Cl)][$B(C_6F_5)_4$]	6.92	12.8
[(tmpa)Cu^{II}(Cl)][$B(C_6F_5)_4$]	6.24	12.0
[(MeTFE-tmpa)Cu^{II})(Cl)][$B(C_6F_5)_4$]	9.48	11.1

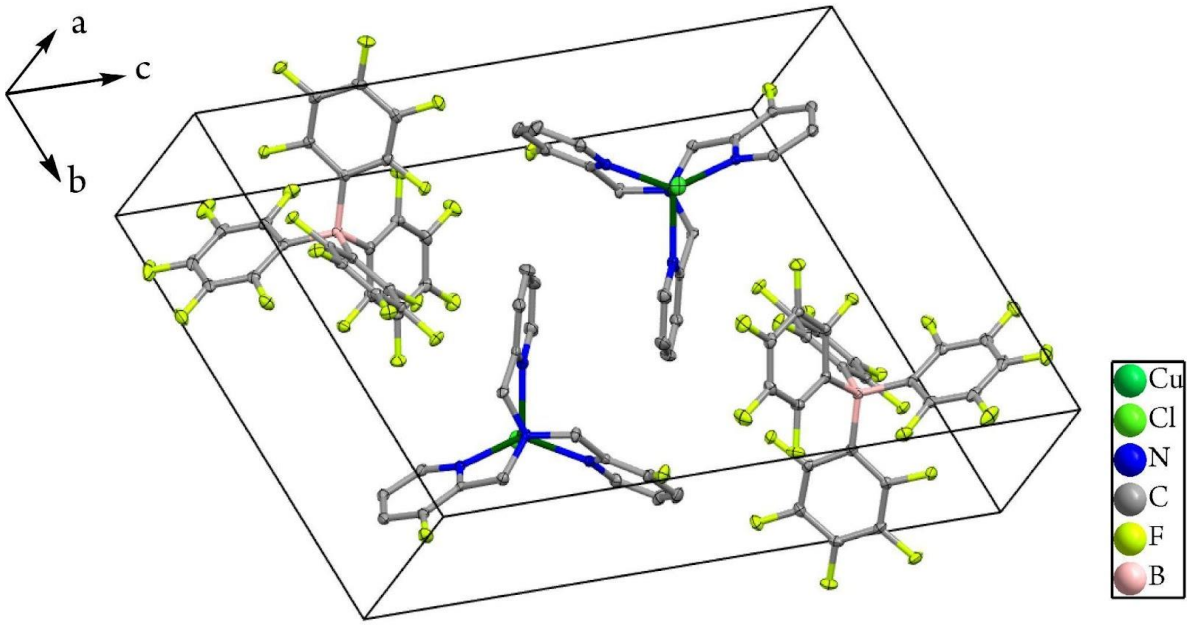

Figure A29. Diagram illustrating the molecular packing of $[(F_2tmpa)Cu^{II}(Cl)][B(C_6F_5)_4]$ at 100(2) K (hydrogen atoms have been omitted for clarity).

Table A2. Crystallographic Data and Data Collection Parameters for of $[(F_2tmpa)Cu^{II}(Cl)][B(C_6F_5)_4]$.

Formula	C42H16BClCuF22N4
T (K)	100(2)
Formula weight	1104.39
Crystal system	Triclinic
Space group	P -1
a, Å	8.0180(2)
b, Å	13.9072(3)
c, Å	18.9264(4)
α , deg	71.521(2)
β, deg	80.883(2)
γ, deg	86.647(2)
V, Å3	1976.27(8)
Z	2
Radiation (λ, Å)	0.71073
dcalcd, g•cm–3	1.856
F(000)	1090
Crystal size (mm3)	0.300 x 0.207 x 0.114
Theta range for data collection	2.294 to 25.500°
μ, mm−1	0.766
No of unique data	7363
Completeness to theta	99.9 %
No. of restraints	2
No. of params. refined	652
GOF on F2	1.039
R1a [I> 2σ(I)]	0.0274
R1a (all data)	0.0309
wR2b (all data)	0.0629
Largest diff. peak and hole	0.294 and -0.512 e.Å-3

$$^{a}R1 = \frac{\sum||F_o|-|F_c||}{\sum|F_o|};\ ^{b}wR2 = \sqrt{\frac{\sum\left[w(F_o^2-F_c^2)^2\right]}{\sum\left[w(F_o^2)^2\right]}}$$

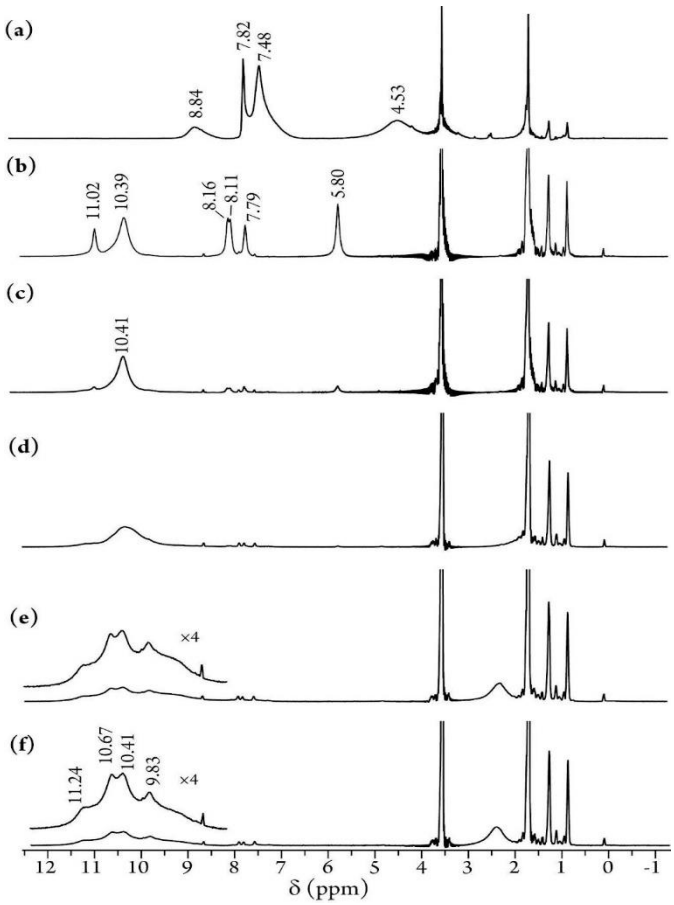

Figure A30. ^{1}H-NMR spectra (selected portions only) of the oxygenation reaction of [(tmpa)Cu^{I}][B(C_6F_5)$_4$] at (a) 0 min, (b) 1 min, (c) 15 min, (d) 1 h 30 min, (e) 4 h 30 min, and (f) 6 h in THF-d_8 (500 MHz) at room temperature.

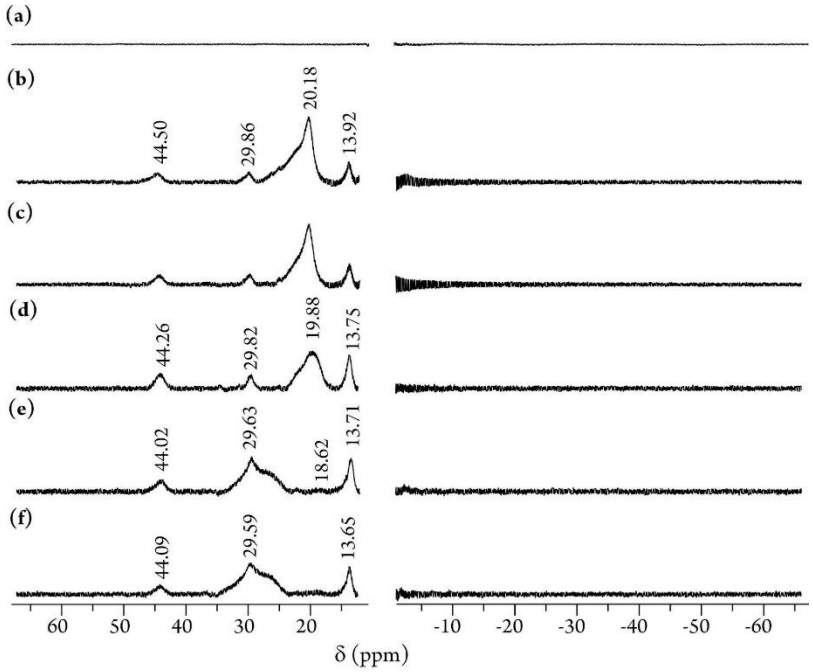

Figure A31. ^{1}H-NMR spectra (selected portions only) of the oxygenation reaction of $[(tmpa)Cu^{I}][B(C_6F_5)_4]$ at (a) 0 min, (b) 1 min, (c) 15 min, (d) 1h 30 min, (e) 4 h 30 min, and (f) 6 h in THF-d_8 (500 MHz) at room temperature.

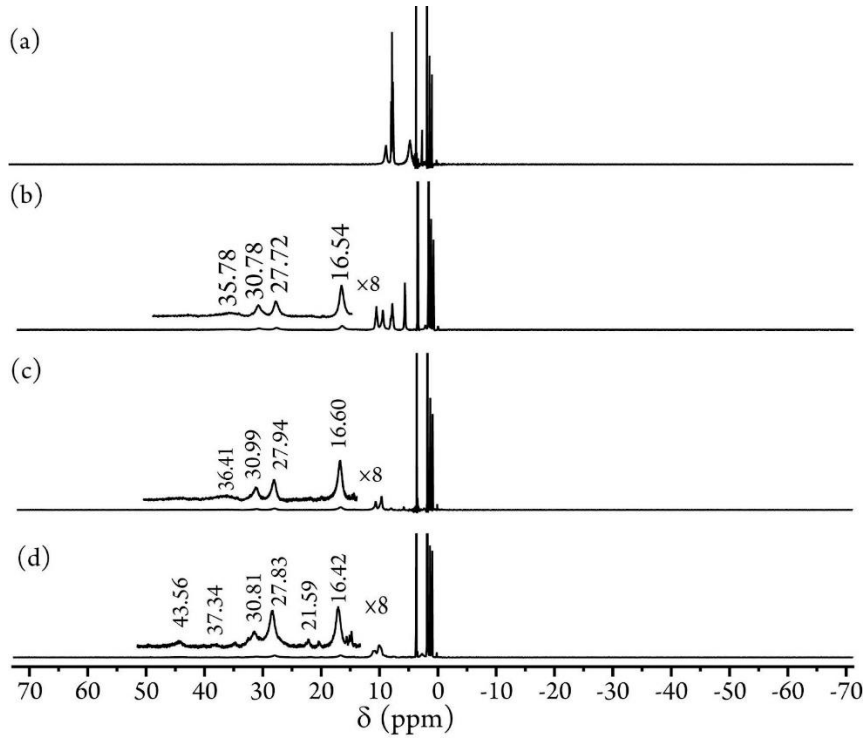

Figure A32. ^{1}H-NMR spectra of the oxygenation reaction of $[(F_2tmpa)Cu^{I}][B(C_6F_5)_4]$ at (a) 0 min, (b) 1 min, (c) 15 min, (d) 6 h in in THF-d_8 (500 MHz) at room temperature.

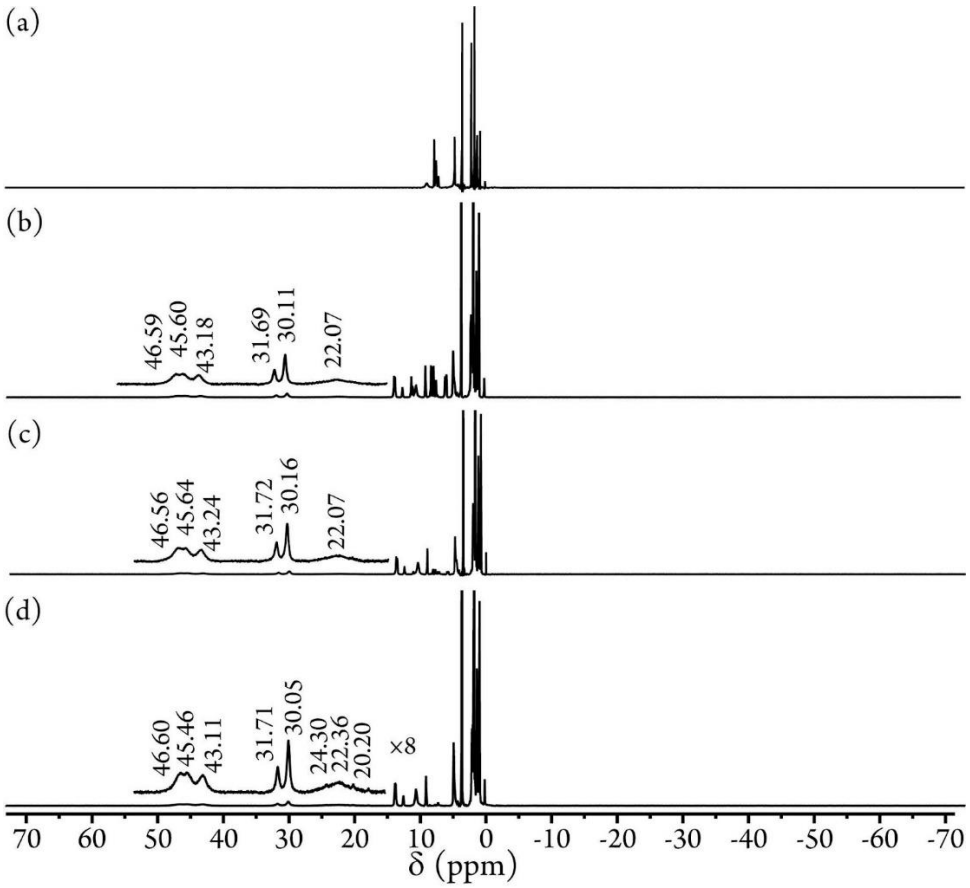

Figure A33. ^{1}H-NMR spectra of the oxygenation reaction of [(MeTFE-tmpa)Cu^{I}][$B(C_6F_5)_4$] at (a) 0 min, (b) 1 min, (c) 15 min, and (d) 6 h in THF-d_8 (500 MHz) at room temperature.

APPENDIX B: SUPPORTING INFORMATION FOR "CHAPTER IV: DIOXYGEN REACTIVITY OF COPPER(I)/MANGANESE(II)-PORPHYRIN ASSEMBLIES"

1. UV-vis Spectroscopy

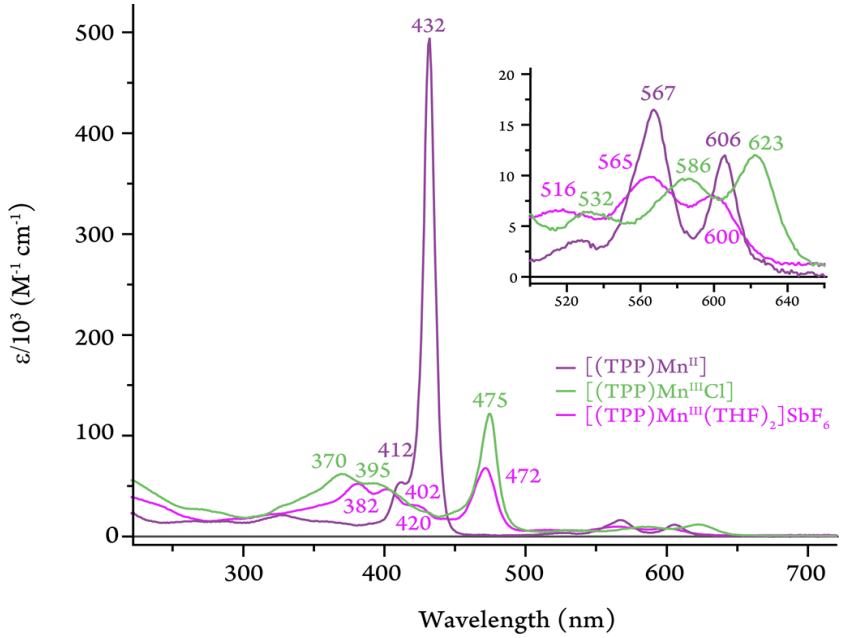

Figure B1. Quantitative electronic spectra of [(TPP)Mn^{II}] (purple), [(TPP)Mn^{III}Cl] (green), and [(TPP)Mn^{III}(THF)$_2$]SbF_6 (magenta) in MeTHF at room temperature (RT).

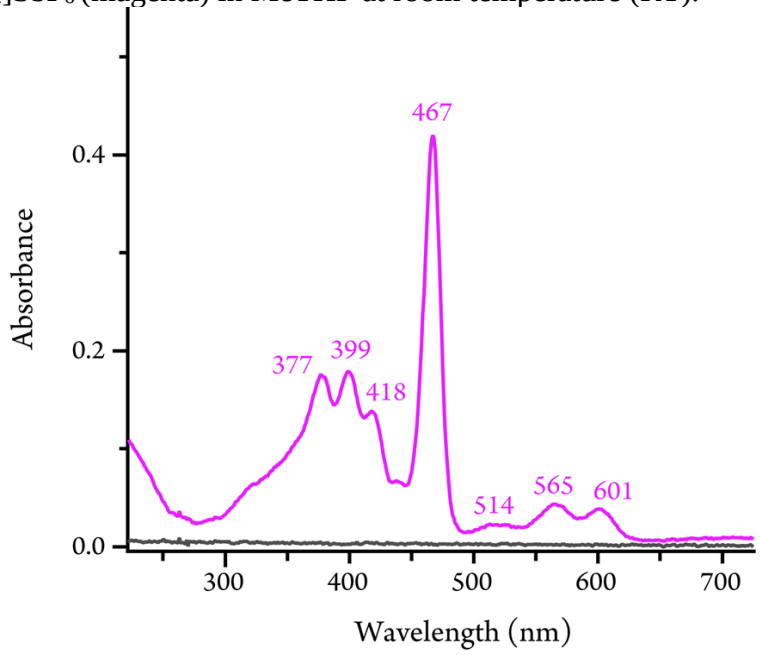

Figure B2. UV-vis spectrum of [(TPP)Mn^{III}(THF)$_2$]SbF_6 in MeTHF at –110 °C.

2. Crystallographic Studies

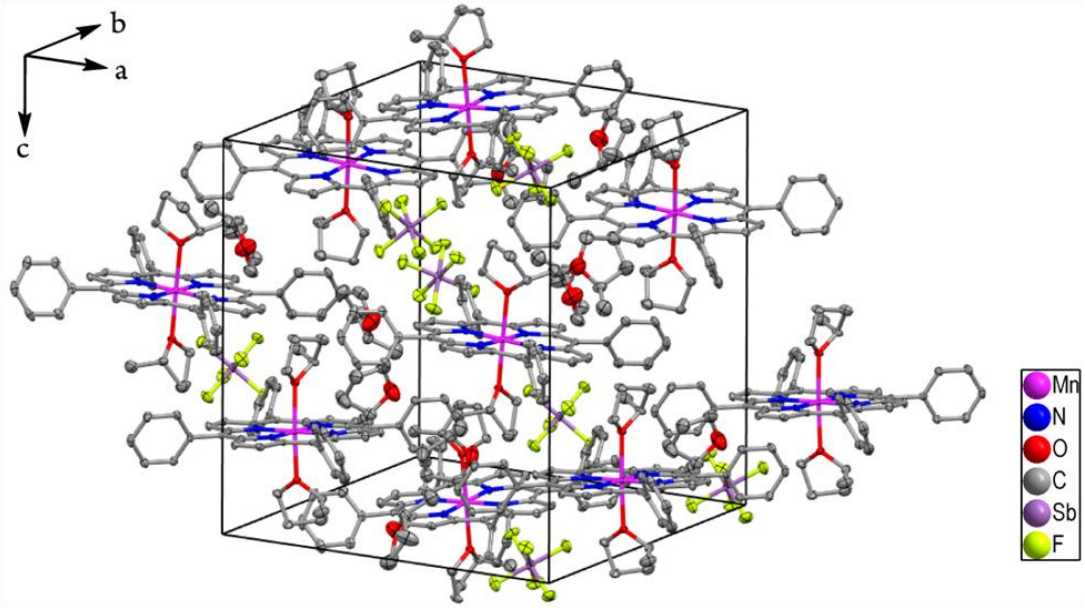

Figure B3. Diagram illustrating the molecular packing of $[(TPP)Mn^{III}(MeTHF)_2]SbF_6 \cdot MeTHF$ at 100(2) K (hydrogen atoms have been omitted for clarity).

Table B1. Crystallographic Data and Data Collection Parameters for $[(TPP)Mn^{III}(MeTHF)_2]SbF_6 \cdot MeTHF$.

Formula	$C_{64}H_{68}F_6MnN_4O_4Sb$
T (K)	100(2)
Formula weight	1247.91
Crystal system	Tetragonal
Space group	P 4_12_12
a, Å	17.4544(3)
b, Å	17.4544(3)
c, Å	18.6564(7)
α , deg	90
β, deg	90
γ, deg	90
V, $Å^3$	5683.8(3)
Z	4
Radiation (λ, Å)	MoKα (0.71073)
dcalcd, g•cm^{-3}	1.458
F(000)	2568
Crystal size (mm^3)	0.17 x 0.13 x 0.08
Theta range for data collection	2.334 to 25.500°
μ, mm^{-1}	0.770
No of unique data	5299
Completeness to theta	99.9%
No. of restraints	0
No. of params. refined	377
GOF on F^2	1.015
$R1^{a\ [I>2\sigma(I)]}$	0.0359
$R1^a$(all data)	0.0494
$wR2^b$ (all data)	0.0859
Largest diff. peak and hole	0.736 and -0.325 e.$Å^{-3}$

$$^aR1 = \frac{\sum||F_o|-|F_c||}{\sum|F_o|};\ ^bwR2 = \sqrt{\frac{\sum\left[w(F_o^2-F_c^2)^2\right]}{\sum\left[w(F_o^2)^2\right]}}$$

Table B2. Selected structural parameters for six coordinated Mn(III) porphyrin complexes having bis-axial oxygen ligation in charge neutral ligands.

Complex	$Mn-O_{ax}$ (Å)[a]	$Mn-N_{por}$ (Å)[a]	Reference
$[(TPP)Mn^{III}(MeTHF)_2]SbF_6$	2.272(3)	2.008(2)	This work
$[(TPP)Mn^{III}(CH_3OH)_2]ClO_4$	2.261(2)	2.006(2)	[1]
$[(TPP)Mn^{III}(N,N\text{-dimethylformamide})_2]ClO_4$	2.217(4)	2.010(5)	[2]
$[(TPP)Mn^{III}(2,6\text{-lutidine } N\text{-oxide})_2]ClO_4$	2.264(4)	1.996(4)	[3]
$[(TPP)Mn^{III}(H_2O)_2]ClO_4$	2.271(2)	2.004(2)	[4]
$[(TPP)Mn^{III}(CH_3OH)_2]SbCl_6$	2.283(5)	2.002(2)	[5]
$[(TPP)Mn^{III}(ONC_6H_4NEt_2)_2]SbF_6$	2.211(4)	2.016 (4)	[6]
$[(DHPP^{b})Mn^{III}(THF)_2]Cl$	2.320(2)	2.004(2)	[7]
$[(TPP)Mn^{III}(THF)_2][(Pc^{c})Co^{III}(L^{d})_2]$	2.307(2)	2.007(2)	[8]

[a] Average value; [b] DHPP corresponds to 5,10,15,20-Tetrakis(3′,5′-dihydroxyphenyl)porphyrinato; [c] Pc corresponds to phthalocyaninato; [d] L corresponds to 1-phenyl-1H-tetrazole-5-thiolate.

3. NMR Spectroscopy

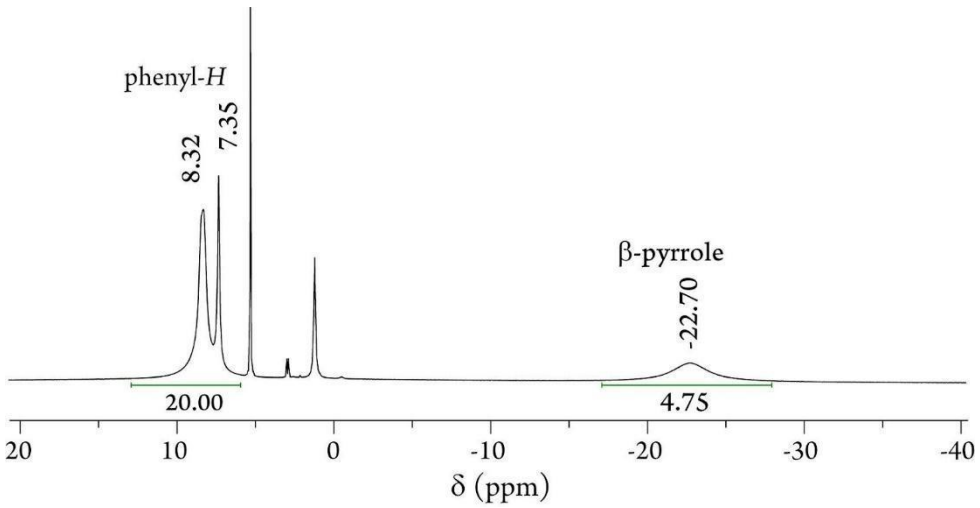

Figure B4. ^{1}H-NMR spectrum of $(TPP)Mn^{III}Cl$ recorded in CD_2Cl_2 at room temperature.

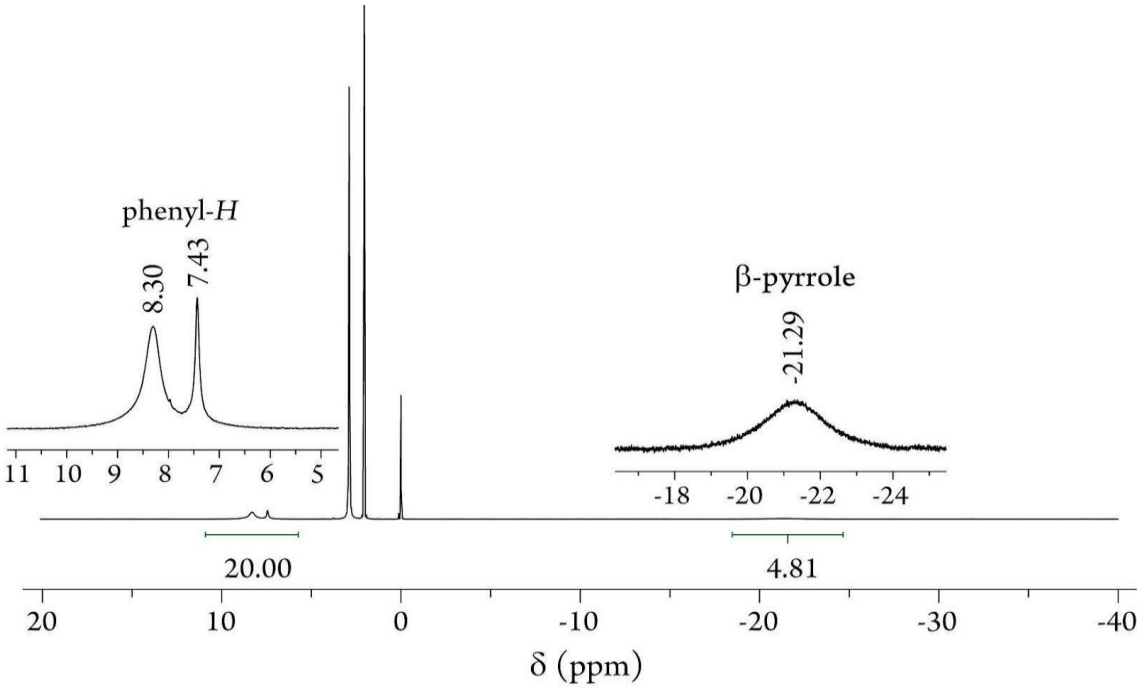

Figure B5. ^{1}H-NMR spectrum of (TPP)Mn^{III}Cl recorded in acetone-d_6 at room temperature.

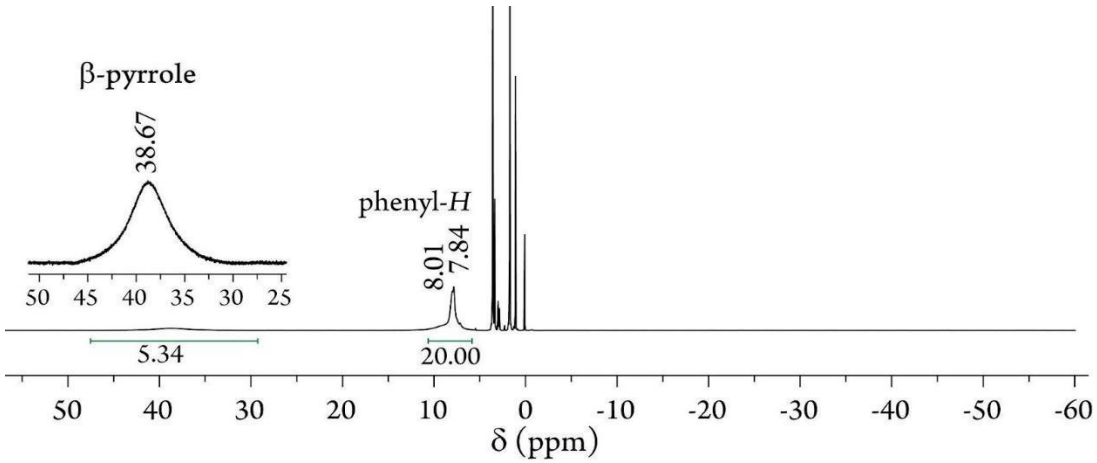

Figure B6. ^{1}H-NMR spectrum of (TPP)Mn^{II} recorded in THF-d_8 at room temperature.

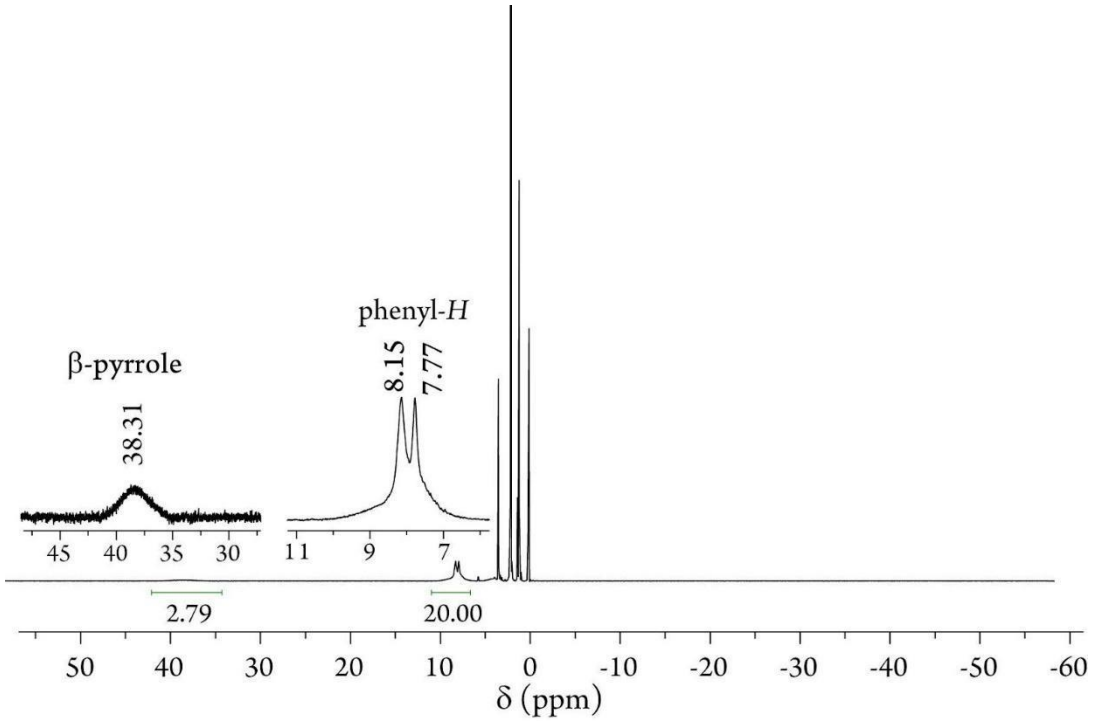

Figure B7. ^{1}H-NMR spectrum of (TPP)Mn^{II} recorded in acetone-d_6 at room temperature.

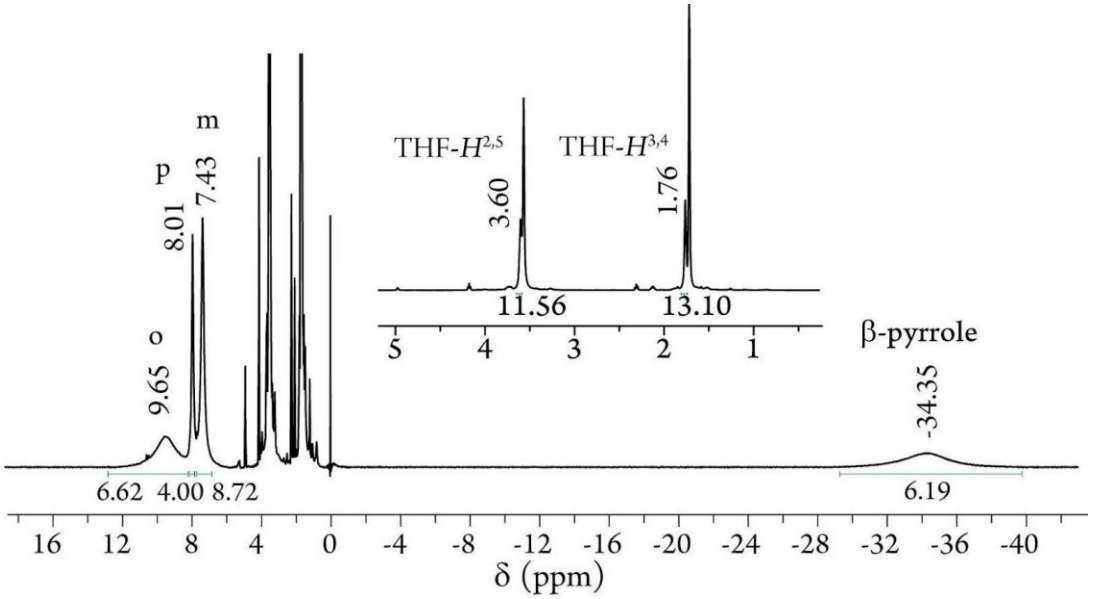

Figure B8. ^{1}H-NMR spectrum of [(TPP)Mn^{III}(THF)$_2$]SbF_6 recorded in THF-d_8 at room temperature.

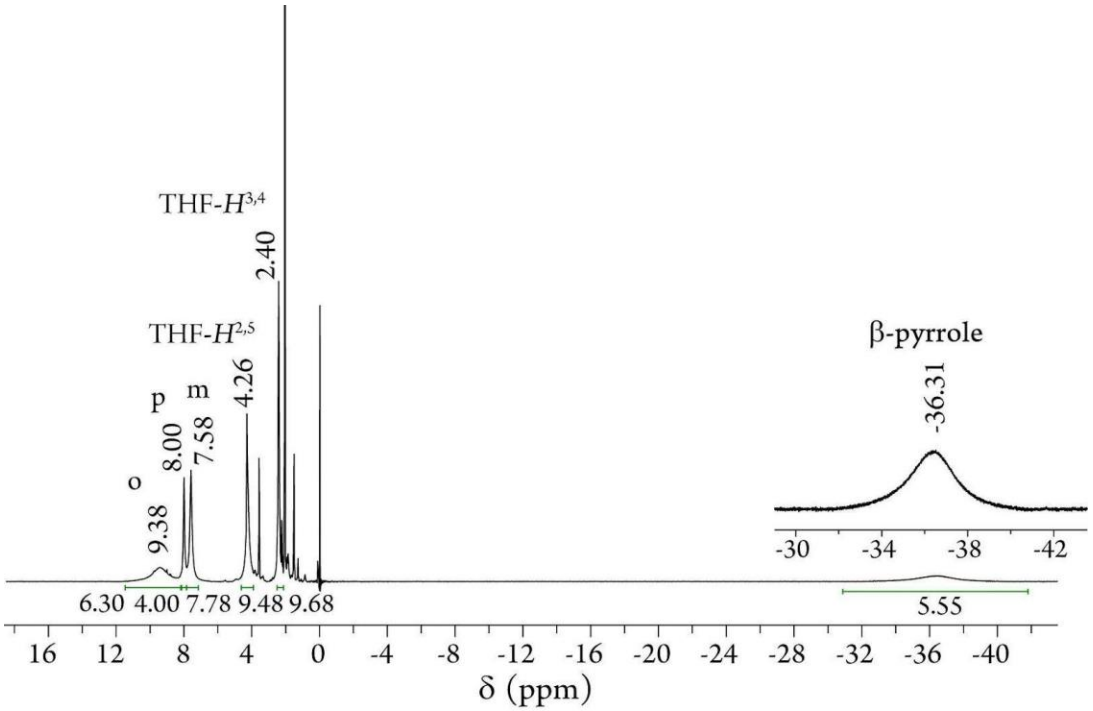

Figure B9. ^{1}H-NMR spectrum of [(TPP)Mn^{III}(THF)$_2$]SbF_6 recorded in acetone-d_6 at room temperature.

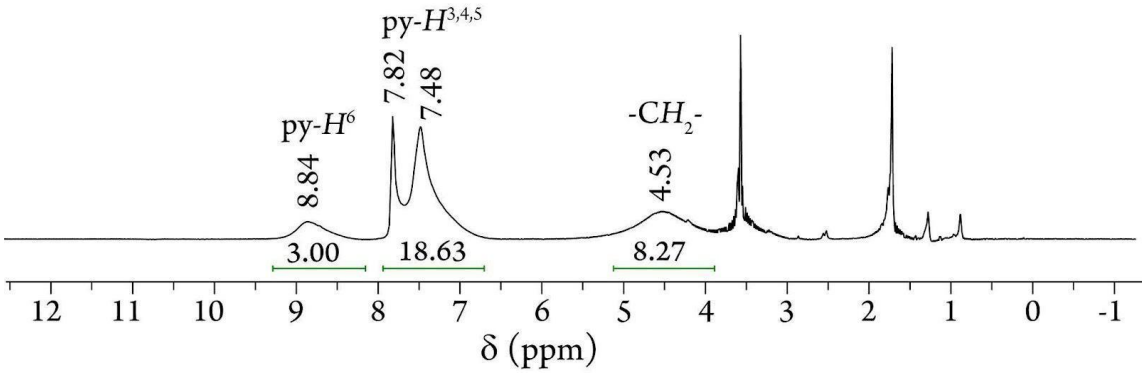

Figure B10. ^{1}H-NMR spectrum of [(tmpa)Cu^{I}(MeCN)][$B(C_6F_5)_4$] recorded in THF-d_8 at room temperature.

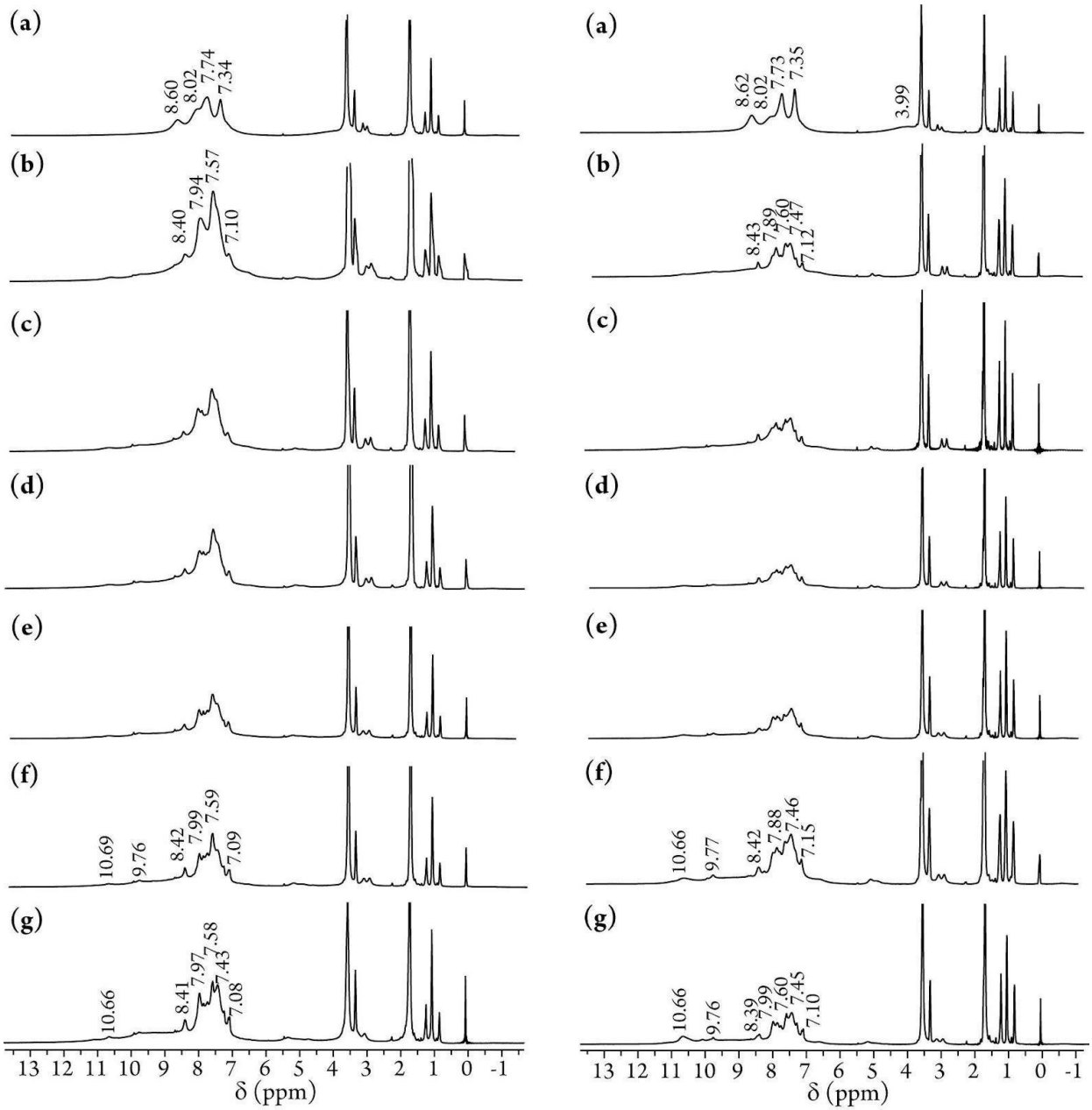

Figure B11. ^{1}H-NMR spectra (selected portions only) (THF-d_8, room temperature) of the oxygenation reaction of a 1:1 mixture, *Left*, and 1:2 mixture, *Right*, of [(TPP)Mn^{II}] and [(tmpa)Cu^{I}(MeCN)][B(C_6F_5)$_4$] at different time intervals: (a) 0 min, (b) 1 min, (c) 15 min, (d) 1 h 30 min, (e) 4 h 30 min, (f) 6 h, and (g) 18 h.

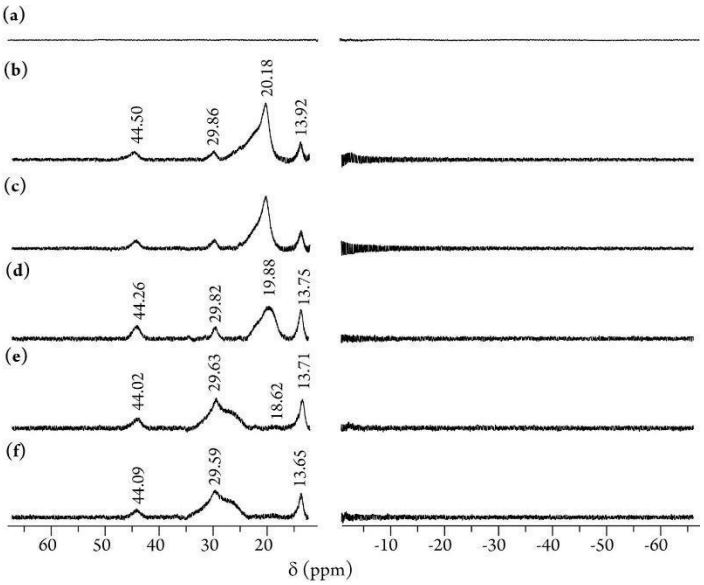

Figure B12. ^{1}H-NMR spectra (selected portions only) (THF-d_8, room temperature) of the oxygenation reaction of [(tmpa)Cu^{I}(MeCN)][B(C_6F_5)$_4$] at (a) 0 min, (b) 1 min, (c) 15 min, (d) 1h 30 min, (e) 4 h 30 min, and (f) 6 h.

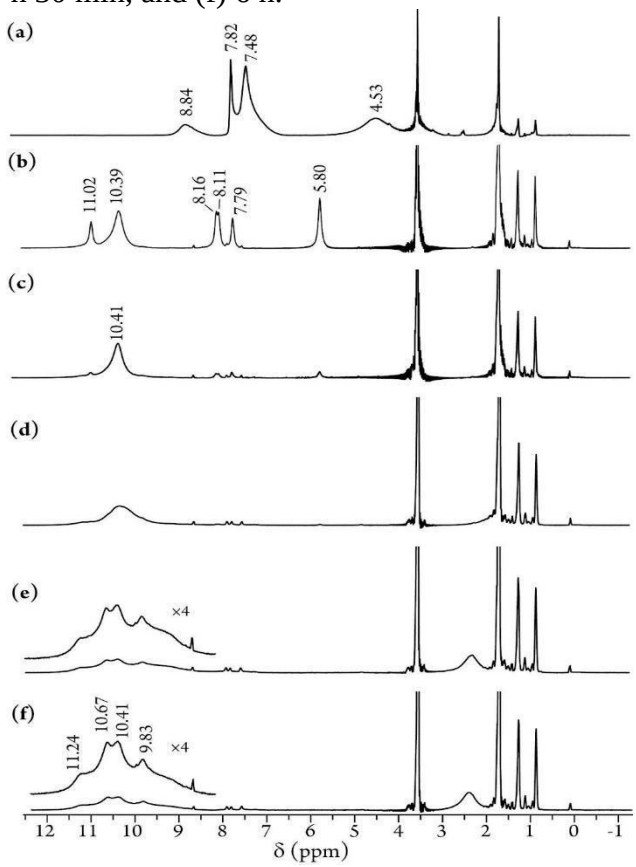

Figure B13. ^{1}H-NMR spectra (selected portions only) (THF-d_8, room temperature) of the oxygenation reaction of [(tmpa)Cu^{I}(MeCN)][B(C_6F_5)$_4$] at (a) 0 min, (b) 1 min, (c) 15 min, (d) 1 h 30 min, (e) 4 h 30 min, and (f) 6 h.

4. Infrared (IR) Spectroscopy

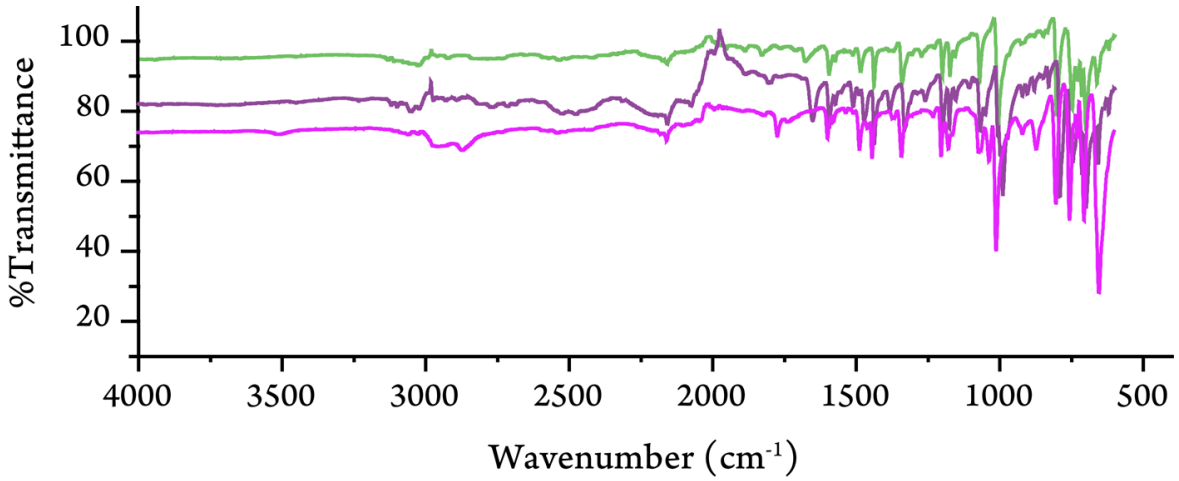

Figure B14. IR spectra of [(TPP)Mn^{II}] (purple), [(TPP)$Mn^{III}Cl$] (green), and [(TPP)$Mn^{III}(THF)_2$]SbF_6 (magenta).

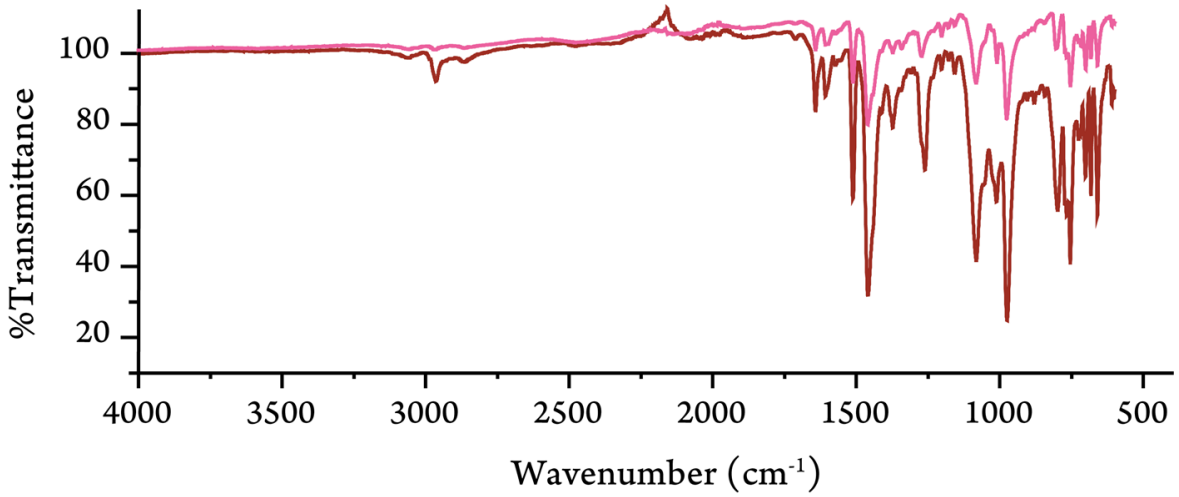

Figure B15. IR spectra of oxygenation products of [(TPP)Mn^{II}] with: 1 eq. of [(tmpa)Cu^{I}(MeCN)][$B(C_6F_5)_4$] (pink) and with 2 eq. of [(tmpa)Cu^{I}(MeCN)][$B(C_6F_5)_4$] (maroon).

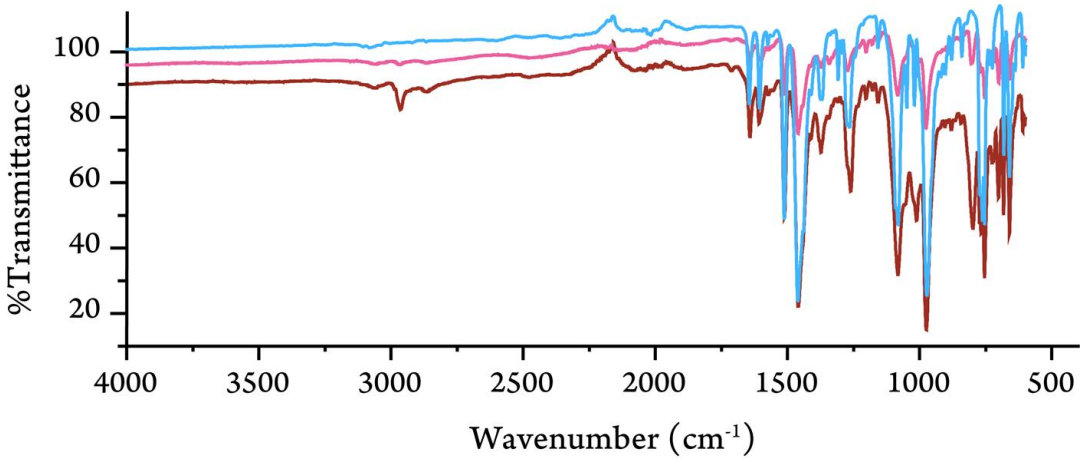

Figure B16. IR spectra of [(tmpa)Cu^{II}Cl][$B(C_6F_5)_4$] (blue) and the oxygenation products of [(TPP)Mn^{II}] with: 1 eq. of [(tmpa)Cu^{I}(MeCN)][$B(C_6F_5)_4$] (pink) and with 2 eq. of [(tmpa)Cu^{I}(MeCN)][$B(C_6F_5)_4$] (maroon).

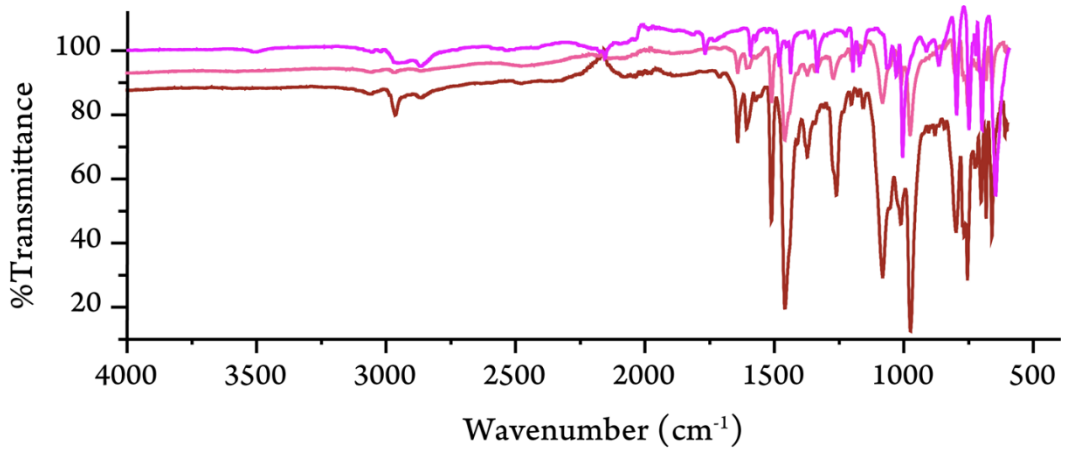

Figure B17. IR spectra of [(TPP)$Mn^{III}$$(THF)_2$]$SbF_6$ (magenta) and the oxygenation products of [(TPP)Mn^{II}] with: 1 eq. of [(tmpa)Cu^{I}(MeCN)][$B(C_6F_5)_4$] (pink), and with 2 eq. of [(tmpa)Cu^{I}(MeCN)][$B(C_6F_5)_4$] (maroon).

Table B3. Metal-sensitive IR bands (cm^{-1}) of TPP manganese complexes.*

TPP	[(TPP)Mn^{II}]	[(TPP)Mn^{III}Cl]	[(TPP)$Mn^{III}$$(THF)_2$]$SbF_6$	1:1 eq. Product	1:2 eq. Product
1596	1594	1595	1598	1598	1598
1491	1473	1486	1487	1487 (shd)	1487 (shd)
1350	1333	1341	1340	1342	1342
1003	990	1006	1010	1010	1011
966	972	966 (shd)	971	(very broad)	(very broad)

* TPP data from Ref. [9]. TPP: Tetraphenylporphyrin. "1:1 eq. Product" and "1:2 eq. Product" refer to the oxygenation products of 1:1 and 1:2 eq. mixtures of [(TPP)Mn^{II}] and [(tmpa)Cu^{I}(MeCN)][$B(C_6F_5)_4$], respectively.

References for Appendix B

1. Hatano, K.; Anzai, K.; Iitaka, Y. The Crystal and molecular structure of bis(methanol)-α,β,γ,δ-tetraphenylporphinatomanganese(III) perchlorate-methanol. A molecular structure relevant to the intermediate-spin six coordinate iron(III) porphyrin. *Bull. Chem. Soc. Jpn* **1983**, *56*, 422-427, 10.1246/bcsj.56.422.
2. Hill, C.L.; Williamson, M.M. Structural and electronic properties of six-coordinate manganese(III) porphyrin cations. Crystal and molecular structure of bis(N,N-dimethylformamide)(tetraphenylporphinato)manganese(III) perchlorate, $[Mn^{III}TPP(DMF)_2]^+ClO_4$. *Inorg. Chem.* **1985**, *24*, 2836-2841, 10.1021/ic00212a027.
3. Hill, C.L.; Williamson, M.W. Electronic and structural properties of a reactive metalloporphyrin with N-oxide axial ligands. Crystal and molecular structure of bis(2,6-lutidine N-oxide)(tetraphenylporphinato)manganese(III) perchlorate. *Inorg. Chem.* **1985**, *24*, 3024-3030, 10.1021/ic00213a031.
4. Williamson, M.N.; Hill, C.L. Molecular stereochemistry of aquamanganese(III) porphyrins. Demonstrable effect of π-arene-porphyrin interaction in the metal coordination environment in the metalloporphyrin. *Inorg. Chem.* **1987**, *26*, 4155-4160, 10.1021/ic00272a005.
5. Scheidt, W.R.; Pearson, W.B.; Gosal, N. Structure of bis(methanol)(meso-tetraphenylporphinato)manganese(III) hexachloroantimonate bis(tetrachloroethane) solvate. *Acta Cryst.* **1988**, *C44*, 927−929, 10.1107/S0108270187012411.
6. Fox, S.J.; Chen, L.; Khan, M.A.; Richter-Addo, G.B. Nitrosoarene complexes of manganese porphyrins. *Inorg. Chem.* **1997**, *36*, 6465-6467, 10.1021/ic970836b.
7. Bhyrappa, P.; Wilson, S.R.; Suslick, K.S. Hydrogen-bonded porphyrinic solids: Supramolecular networks of octahydroxy porphyrins. *J. Am. Chem. Soc.* **1997**, *119*, 8492-8502, 10.1021/ja971093w.
8. Tong, S.-l.; Zhang, J.; Yan, Y.; Hu, S.; Yu, J.; Yu, L. Self-assembled supramolecular architecture with alternating porphyrin and phthalocyanine, bonded by hydrogen bonding and π–π stacking. *Solid State Sci.* **2011**, *13*, 1967-1971, 10.1016/j.solidstatesciences.2011.08.026.
9. Kincaid, J.; Nakamoto, K. Vibrational spectra of transition metal complexes of tetraphenylporphine. *J. Inorg. Nucl. Chem.* **1975**, *37*, 85-89, 10.1016/0022-1902(75)80130-8.